

INFORMATION TO USERS

This manuscript has been reproduced from the microfilm master. UMI films the text directly from the original or copy submitted. Thus, some thesis and dissertation copies are in typewriter face, while others may be from any type of computer printer.

The quality of this reproduction is dependent upon the quality of the copy submitted. Broken or indistinct print, colored or poor quality illustrations and photographs, print bleedthrough, substandard margins, and improper alignment can adversely affect reproduction.

In the unlikely event that the author did not send UMI a complete manuscript and there are missing pages, these will be noted. Also, if unauthorized copyright material had to be removed, a note will indicate the deletion.

Oversize materials (e.g., maps, drawings, charts) are reproduced by sectioning the original, beginning at the upper left-hand corner and continuing from left to right in equal sections with small overlaps. Each original is also photographed in one exposure and is included in reduced form at the back of the book.

Photographs included in the original manuscript have been reproduced xerographically in this copy. Higher quality 6" x 9" black and white photographic prints are available for any photographs or illustrations appearing in this copy for an additional charge. Contact UMI directly to order.

UMI

A Bell & Howell Information Company
300 North Zeeb Road, Ann Arbor MI 48106-1346 USA
313/761-4700 800/521-0600

SIGNIFICANCE OF MULTIPLE SCATTERING IN
REMOTELY SENSED IMAGES OF NATURAL
SURFACES

by

Wen-Hao Li

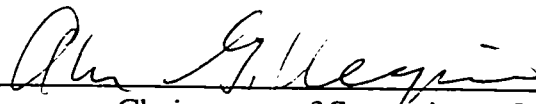
A dissertation submitted in partial fulfillment of the
requirements for the degree of

Doctor of Philosophy

University of Washington

1997

Approved by



Chairperson of Supervisory Committee



Program Authorized

to Offer Degree Department of Geological Sciences

Date November 19, 1997

UMI Number: 9819269


UMI Microform 9819269
Copyright 1998, by UMI Company. All rights reserved.

**This microform edition is protected against unauthorized
copying under Title 17, United States Code.**

UMI
300 North Zeeb Road
Ann Arbor, MI 48103

Doctoral Dissertation

In presenting this dissertation in partial fulfillment of the requirements for the Doctoral degree at the University of Washington, I agree that the Library shall make its copies freely available for inspection. I further agree that extensive copying of this dissertation is allowable only for scholarly purposes, consistent with "fair use" as prescribed in the U.S. Copyright Law. Requests for copying or reproduction of this dissertation may be referred to University Microfilms, 1490 Eisenhower Place, P.O. Box 975, Ann Arbor, MI 48106, to whom the author has granted "the right to reproduce and sell (a) copies of the manuscript in microform and/or (b) printed copies of the manuscript made from microform."

Signature 
Date Nov. 19, 1987

University of Washington

ABSTRACT

Significance of Multiple Scattering
in Remotely Sensed Images of Natural Surfaces

by Wen-Hao Li

Chairperson of the Supervisory Committee: Professor Alan R. Gillespie
Department of Geological Sciences

To separate reflectivity and surface structure information in remotely sensed images, a practical hybrid radiosity model, first developed for use in natural landscape environments, has been adapted from existing algorithms in the computer graphics and engineering fields. This radiosity model can be used to predict quantitatively the total radiance leaving a surface, including single-scattering and multiple-scattering components. The model operates on digital terrain models (DTMs) of the topography of the surfaces. A central problem in the radiosity model is to estimate the geometric function or "form factor", which determines how much light is received from adjacent surface elements. In order to achieve the high precisions required to predict the multiple-scattering signal from natural surfaces, the new radiosity model balances accuracy and speed of computation efficiently. For an image of 100x100 pixels, the radiosities can be estimated with < 2% error in 1.5 hours on a DEC Alpha 3000 with a 276 Mhz processor, run under Unix.

Using the hybrid radiosity model, multiple scattering (MS) has been quantitatively predicted for natural surfaces at pixel and subpixel scales for the first time. These two scales separate multiple-scattering effects into those resolved by Landsat Thematic Mapper (TM) and those that are unresolved at subpixel scale. The model results have been verified by laboratory measurements. Two experiments have been made in

laboratory for two types of surfaces: surface "TA," consisting of parallel triangular prisms and having an accurate DTM, and surface "BC," fabricated by a computer-controlled machine using DTMs of the Bluff Creek watershed in Northern California. Radiosities predicted for the two surfaces using the computational model were compared with CCD camera measurements of radiance from the physical surfaces. The comparisons demonstrate that the practical hybrid radiosity model is reliable, with 98% accuracy.

In this study, I inverted the radiosity model to estimate the surface roughness of geological surfaces from Landsat TM images. I also applied the radiosity model to correct topographic effects in rugged vegetated areas. In both applications, the radiosity model was used to calculate the bidirectional reflectance distribution function (BRDF) for simulated surfaces designed to match the vegetation canopy surface and geological surfaces (such as a gravel bar). Including the multiple-scattering component in the radiosity calculation noticeably improves both the surface roughness inversion and the topographic correction.

TABLE OF CONTENTS

LIST OF FIGURES	v
LIST OF TABLES	xiii
GLOSSARY	xiv
LIST OF ABBREVIATIONS	xviii
INTRODUCTION	1
CHAPTER 1: RADIOSITY MODEL	6
INTRODUCTION	6
PREVIOUS WORK	8
RADIOSITY MODEL	10
Radiosity theory.....	11
Form-factor calculation	13
A HYBRID RADIOSITY MODEL FOR NATURAL SURFACES	15
Modeling the environment	15
Determining the form factor (hybrid form-factor method).....	17
Algorithm selection	24
Iteration in the radiosity equation.....	28
PRESENTING RADIOSITY RESULTS	29
Rendered images.....	29
Analytic results	30
Radiosity related to the radiance measured by Landsat.....	30
CONCLUSION	32
CHAPTER 2: MULTIPLE-SCATTERING PREDCTIONS	34
INTRODUCTION	34
BACKGROUND AND METHODS	36
RESULTS	37
Multiple-scattering effects at the topographic (pixel) scale.	38

Multiple-scattering effects at the subpixel scale.....	44
DISCUSSION.....	49
SUMMARY AND CONCLUSIONS.....	52
CHAPTER 3: VALIDATION OF RADIOSITY MODEL.....	54
INTRODUCTION.....	54
EXPERIMENTAL SETUPS AND LABORATORY MEASUREMENTS.....	56
Making the surfaces.....	57
Illuminating the surfaces.....	58
CCD camera system and radiosity measurement.....	58
Registration and scaling.....	59
ERRORS IN LABORATORY MEASUREMENTS.....	61
Geometric errors of test surfaces.....	61
Illumination error.....	62
Stray light.....	64
Radiosity approximation.....	64
COMPARING THE PREDICTED, MEASURED AND RADIOSITY IMAGES.....	64
image matching.....	65
Quantitative analysis of matching differences.....	74
Radiance mismatch at different illumination elevation angles.....	75
Significance of multiple-scattering.....	77
DISCUSSIONS AND CONCLUSION.....	80
CHAPTER 4: SEMI-EMPIRICAL INVERSION OF TM IMAGES FOR SURFACE	
ROUGHNESS.....	82
INTRODUCTION.....	82
INVERSION MODEL.....	84
OPTIMIZED FINITE-IMPULSE-RESPONSE (FIR) FILTER.....	87
Computer-simulated surfaces.....	88
Reflectance from simulated surfaces.....	91

Laboratory measurement of rock spectra	93
FIR filter	95
RESULTS	97
Estimates of surface roughness.....	98
Correlation of estimates of roughness with “ground truth”	101
Visual comparison of roughness estimates among the four methods.....	103
DISCUSSION	105
CONCLUSIONS	108
CHAPTER 5: TOPOGRAPHIC CORRECTION OF A TM IMAGE USING THE	
CANOPY PHOTOMETRIC FUNCTION	
INTRODUCTION	110
RADIOSITY MODEL FOR CALCULATING THE CANOPY FUNCTION (CF) 112	
CF Topographic correction model.....	112
Canopy surface models.....	116
CFS FOR LANDSAT TM IMAGES	117
Test sites	117
CFs for the two images.....	118
Characteristics of the CF	120
TOPOGRAPHIC CORRECTION OF A LANDSAT TM IMAGE	123
Image preprocessing.....	123
Downwelling sky illumination and surface reflectivities effects to the CF	124
Topographic correction without multiple-scattering	125
Topographic correction with MS.....	127
DISCUSSION	129
Tree shape.....	130
Tree spacing.....	132
Adjustment required for transmissive trees	133
Reflectivity	134

COMPARISON WITH OTHER METHODS	135
Cosine correction.....	135
SCS (sun-canopy-sensor) correction	135
Minnaert correction	136
Comparison of the methods.....	136
Topographic corrections for Image 84	137
Topographic corrections for Image 90	140
CONCLUSIONS	142
SUMMARY	145
MODELING.....	145
APPLICATIONS.....	148
BIBLIOGRAPHY	153
APPENDIX A: REFLECTANCES CALCULATED USING RADIOSITY MODEL FROM THE COMPUTER-SIMULATED SURFACE FOR DIFFERENT ROCK SAMPLES	168

LIST OF FIGURES

<i>Number</i>	<i>Page</i>
Figure 1. Schematic diagram shows the geometric relation of radiosity with components: single scattering, and multiple scattering components, and roughness at Landsat TM pixel and subpixel scales. At the pixel (30-m) scale, roughness is topographic and is described by DTMs. At the subpixel scale, roughness is textural; typical scale lengths vary widely with terrain.....	12
Figure 2. Schematic plot for illustrating the definition of symbols used in the radiosity model.	14
Figure 3. Flow chart shows the major procedures in the radiosity mode.....	15
Figure 4. Form factor vs. distance calculated by the double-contour integral method for the case: $\alpha = 150^\circ$, $\theta_r=75^\circ$, and $\beta=10^\circ$. Maximum value of the form factor is 1 (parallel elements facing each other at close range).....	18
Figure 5. Schematic plot for the half-contour integral algorithm, adapted from Ashdown.....	19
Figure 6. This diagram shows the basic cosine term of the form factor equation 4 as a function of the projection angle (θ_p) for facing angles (a) from 90° to 170° . The positive values indicate that the elements are visible to each other, whereas the negative values indicate the pair of elements cannot “see” each other.....	21
Figure 7. Form-factor values calculated using three different algorithms: double-contour integral (DCI), half-contour integral (HCI), and element-to-element (EE) methods. The DCI is the most accurate. The approximation errors using HCI decrease with the distance and the ones using EE is	

almost constant in the log-axis. The example is calculated using $\alpha = 150^\circ$, $\beta = 30^\circ$, and $\theta_i = 75^\circ$	23
Figure 8. Schematic flow chart illustrating a hierarchy structure for classifying the geometric orientation of a pair of elements into simple categories. For each case, the threshold distance value is evaluated for a specified form- factor precision. All the values in the chart are angles in degrees.....	26
Figure 9. Radiosity decreases with incidence angle, whereas MS increases. These data were calculated at the 30-m (pixel) scale from a DTM for the BC1 area, with $E = 47^\circ$, sun azimuth = 133° , $\rho = 30\%$, $F_A = 10\%$, and solar irradiance = $200 \text{ (Wcm}^{-2}\text{)}$. a. Radiance vs. local incidence angle. b. SS_r and MS_r (relative to R) vs. local incidence angle.....	35
Figure 10. Perspective views of Bluff Creek image subsets show the variation with surface roughness in the distribution of relative MS. a). Subset BC1 (rougher terrain). b). Subset BC2 (smoother broad valley). For both a and b, $E = 47^\circ$ and sun azimuth = 133° , typical for August or May Landsat images.....	39
Figure 11. Perspective views of Bluff Creek subsets show the relative MS distribution variation due to the sun elevation angle. a. Subset BC1, with $E = 21^\circ$, sun azimuth = 155° (December Landsat image), b). Subset BC1 with $E = 62^\circ$, azimuth = 121° (June Landsat image). Images are 3.6 km on a side.....	41
Figure 12. The fraction of the area of BC1 with $> 5\%$ of MS_A and MS_r as function of (a) sun elevation angle E , (b) surface reflectivity ρ , and (c) sky illumination fraction F_A . For a, b, and c, sun azimuth is fixed at 133°	42
Figure 13. Radiosity results as function of local solar incidence angle for the DV cm- scale DTM ($E = 47^\circ$, sun azimuth = 133° , $\rho = 30\%$, and $F_A = 10\%$). (a).	

	Radiosity vs. local incidence angle. (b). SS_R and MS_R vs. local incidence angle.	44
Figure 14.	Variation in $A_{5\%}$ (MS_A) with two standard deviation of the second derivative of topography (D_s) evaluated over the images. The BC1 and BC2 represent the terrain rough surfaces at 30-m resolution. The DV and BC are gravel-bar surfaces at 1-cm resolution. The bigger of D_s indicates the rougher (at the subpixel scale) of the surfaces.....	47
Figure 15.	The photometric function calculated using the radiosity model for the Death Valley (DV) gravel surface and the Bluff Creek (BC) cobble surface. The solid curve represents an ideal flat Lambertian surface. a). The radiance as a function of view angle for a fixed solar incidence angle of 47° . Note that radiance is that from a 1-m square. In remotely sensed data the area viewed increases as the view becomes more oblique such that, for a smooth Lambertian surface, the measured radiance is invariant with view angle. b). The radiance as a function of solar incidence angle for a fixed view angle of 90°	48
Figure 16.	The experimental set-up for the laboratory measurements of CCD images, and relevant geometric parameters. Some associated errors with these parameters are: a. 'open edge', b. 'slope variation,' and c. 'E-angle variation,'	56
Figure 17.	Histograms of predicted radiance (scaled radiosity), predicted single-scatter radiance, and measured radiance (CCD) for the surface. a) TA and b). BC. 'N' is the number of pixels. Radiosity and single-scattering component have been scaled by π	66
Figure 18.	Distributions of mismatch areas between predicted and measured radiance are shown in the Bluff Creek (BC) DEM image (a and b) relative to their scatter plot (c) of predicted radiance (scaled radiosity), predicted single scattering radiance, and CCD measured radiance. a). The distribution of	

	scaled radiosity values that are not matched by the measured radiance. b). The distribution of measured radiance data that were not predicted by the scaled radiosity. c). The scatter plot of the measured radiance data and scaled radiosity and single scattering results vs. the local incidence angle. Note that the mismatch data in both a and b have a similar pattern.....	68
Figure 19.	Scaled single-scattering component (a,d), scaled radiosity (b,e), and measured radiance (CCD) (c, f) images for test surfaces TA (a-c) and BC (c-f).....	70
Figure 20.	The diagrams show how the distribution of the MS component in scene varies with the illumination elevation angle (E) for test surface TA. The “measured MS” is found by subtracting the scaled SS component from the CCD measured radiance, and the “predicted MS” is found by subtracting the SS component from the scaled radiosity. The horizontal axis is the fraction of the radiosity due to multiple scattering in each pixel, and the vertical axis is the area fraction in the scene. Note the y-axis scale is different from histogram to histogram.....	72
Figure 21.	Residual (difference) images for test surface TA (a.) and BC (b.). The residual images are the differences of predicted radiance B/π and measured radiance R normalized by the maximum B_{max}/π . The scale on the right shows the color-coded residuals in the range of 0% to 100%.....	75
Figure 22.	Cumulative histograms of mismatch errors (residuals) for test surface TA (a) and BC (b). The mismatch error in percentage is $(B/\pi-L)/B_{max}/\pi$. E is the illumination elevation angle.	76
Figure 23.	Plots of the area fraction as a function of illumination elevation angle, E. a). Area of the surface TA for which $MS_i/B_i > 20\%$. b). Area of surface BC for which $MS_i/B_i > 15\%$	78

- Figure 24. Examples of computer-simulated surfaces generated from the offset and slope terms of synthetic power-law spectra with random phase angles. The upper circle (indicated by arrows) shows the changes of surfaces as the slope term is changed; the lower circle shows the changes of surfaces as the offset term is changed. For these examples, the spatial scale and field of view are arbitrary: the simulated surface might represent the surface of a sand dune or it might represent a mountain range of equal offset values. The offsets is in unit of cm and the slope is in units of cm^{-1} 90
- Figure 25. VNIR normalized radiance (to flat surface) as a function of slope and offset parameters for simulated rough surfaces, defined by power-law spectra with random phase angles. 91
- Figure 26. Radiance response to offset (roughness at subpixel scale) and reflectivity of simulated surfaces. Power spectrum slope has been fixed at -2.05 cm^{-1} . a) Radiance (L in unit of $\text{Wcm}^{-2}\text{sr}^{-1}$) from rough surfaces without MS. b) Radiance ratio (L_r / L_{sm}) of rough to smooth surface, without MS. c) Radiance (L) from rough surface with MS. d) Radiance ratio (L_r / L_{sm}) of rough to smooth with MS. Color bands show zones of equal radiance or ratio. 93
- Figure 27. Spectra of twelve rock samples collected from Grotto Canyon Wash, Death Valley. 94
- Figure 28. Landsat TM image of Death Valley, California shows the sites of roughness measurements on two alluvial fan systems: Kit Fox Hills and Grotto Canyon. At each site, the micro-topographic profiles have been measured using a close-up photogrammetric technique. "A" shows an unnamed alluvial fan. "B" indicates the playa unit in the upper left of the image. 96
- Figure 29. Surface roughness estimates from Landsat TM data using four methods. The brighter the roughness of the surfaces. Mountainous areas is not in

consideration for subpixel roughness estimation. a). theoretical relationship (semi-empirical method) in which the FIR filter is optimized by modeling and Lab spectra. b). Field-data method in which the FIR filter is optimized by field roughness measurements. c). Image-data method in which the FIR filter is optimized by the image training data with known varied roughness. d). Shade-image method in which the FIR filter is optimized by the training data with known shade fraction. 99

Figure 30. Linear regression of estimated roughness with field measurements for four methods. Note the y axis scales are all different. a) Field-data inversion. b) Semi-empirical inversion. c) Image-data inversion. d) Shade-image method. 102

Figure 31. The canopy-surface model diagram. a). The geometry and parameters of the canopy surface (E sun elevation angle, s terrain slope, $-\tau$ local incidence angle). b). The simulated canopy surface image on a 30° slope (trees are randomly distributed with same height and size). The “box” surrounding the plot is a device to approximate MS from neighboring plots in an infinite forest. The vertical patterns in the box walls are the insides of trees where they overlap the edge of the plot. 115

Figure 32. The canopy function of topographic correction is calculated for Image 90 (the Landsat image acquired on the November 8, 1990, with 37.5° sun elevation angle and 145° azimuth angle), when $\rho = 25\%$. Normalized radiance refers to the radiosity is normalized by the single scattering value at $\tau = 0^\circ$ ($\alpha = 30^\circ$). Color shows zones of radiance. 119

Figure 33. The canopy functions (CFs) of Image 84 for surface reflectivities from $\rho = 0\%$ to 55% in the principle plane, compared with the cosine curve of the local incidence angle. Region 1 is the negative-angle range ($\tau < 0^\circ$).

Region 2 is the middle-angle range ($0^\circ \leq \tau \leq 60^\circ$). Region 3 is the high-angle range ($60^\circ \leq \tau \leq 90^\circ$).....	120
Figure 34. The normalized radiance data calculated from simulated canopy surfaces related to the cosine of the local incidence angle for all sun-surface-camera geometries. It is similar to Figure 35 by projecting all the data on to the principle plane in the range $0 \leq \cos(\tau) \leq 1$. The scatter of the data near $\cos(\tau) = 1$ is caused by the high radiance in the negative angle range. The solid line is the linear curve for a flat Lambertian surface. The terrain slopes are from -50° to 50° . Surface reflectivity is 25%. The data is normalized to the single-scattering radiance value for $\tau = 0^\circ$	121
Figure 35. Comparison of the topographic correction for Image 84 using CFs. a). Color composite of three bands: 3 (green), 4 (blue), and 5 (red). b). The data scatter plots before and after topographic correction for band 4.	126
Figure 36. The comparison of topographic correction of Image 84 with and without MS, using CFs. a). A scatter plot of CF correction without MS, and b). The scatter plot of CF correction with MS. Both plots are resampled by 1/7 for clearer display. c). The comparison of the standard deviations of the two corrected reflectances.	129
Figure 37. The Canopy Functions (CFs) for various type of canopy surfaces. a). CFs for canopy surfaces made of cone-shape trees (conifer) and ellipsoidal trees, compared with cosine curve. b). CFs for canopy surfaces of different canopy closure, from 0% - 90%. c). Comparisons among the canopies containing opaque trees with $\rho = 25\%$, transmissive trees with $r = 25\%$ (“trans.”), trees with a distributed pattern of ρ (crown = 40%, trunk = 5%, and substrate = 25%, “trans. patt.”), and cosine curve. Y axis is scaled radiance normalized by the radiance at $\tau = 0^\circ$	131

Figure 38. Scatter plots of radiance data ($Wcm^{-2}sr^{-1}$) before and after using four different methods of topographic correction on band 4 of Image 84. 138

Figure 39. The standard deviations of topographically corrected reflectance about the regression lines in the scatter plots of radiance vs. $\cos(\tau)$. In both diagrams, the CF's have the smallest standard deviation for all local incidence angles. a). Standard deviations for corrected Image 84 from Figure 38. b). Standard deviations for corrected Image 90 from Figure 40.139

Figure 40. The scatter plots of the topographic correction before and after using four different methods on band 4 of Landsat Image 90. 141

LIST OF TABLES

<i>Number</i>	<i>Page</i>
Table 1. Multiple-scattering at the 30-m scale, Bluff Creek subsets BC1 and BC2	40
Table 2. Multiple-scattering at the cm scale, Death Valley and Bluff Creek scenes.....	45
Table 3. Rock reflectivities for TM bands.....	95
Table 4. Roughness parameters calculated measurements of surface roughness by close-up stereophoto grammetry at 11 sites in Death Valley	98
Table 5. Slopes of the regression line of the TM image data for all combinations of F_{λ} and ρ	125
Table 6. Comparisons of the regressions of image data before and after topographic correction using the CFs.....	127
Table 7. Comparisons of the topographic corrections with and without Multiple- Scattering.....	128
Table 8. Comparisons of four topographic corrections for Image 84.....	137
Table 9. Comparisons of four topographic corrections for Image 90.....	140

GLOSSARY

<i>Radiant Flux (ϕ)</i>	The radiant energy (photons) passing through an area element in unit time: Wcm^{-2} .
<i>Radiant Flux Density (D)</i>	The radiant flux intercepted per unit area of plane surface at a specific spectral wavelength: Wcm^{-3} .
<i>Irradiance (I_{rr})</i>	The radiant flux density for incident upon a plane surface: Wcm^{-2} .
<i>Radiosity (B) or Exitance (M)</i>	The radiant flux density for flux leaving a plane surface: Wcm^{-2} .
<i>Radiance (L)</i>	The radiant flux per unit solid angle leaving an extended source in a given direction per unit projected source area in that direction: $Wcm^{-2}sr$.
<i>Rough & Smooth surfaces</i>	Describe the surface geometric structure, and are scale dependent terms.. Smooth surface is defined here that all the surface finite elements are oriented in same direction, and rough surface is opposite. In this study, they are relative to pixel scale, referring rough and smooth surfaces at pixel and subpixel scales.
<i>Reflectivity (ρ)</i>	Fraction of irradiance reflected from a smooth surface.
<i>Reflectance (r)</i>	Fraction of irradiance reflected from a rough surface. i.e. B/I_{rr}
<i>Sky illumination</i>	The radiant flux density scatters from sky as diffuse light source: Wcm^{-2} , including upwelling (A_{uw}) and downwelling (A_{dw}) scattering components.
<i>Illumination Elevation Angle</i>	See “Sun Elevation Angle (E).”

<i>Sun Elevation Angle (E)</i>	The solar angle E above sea-level horizon, equal to 90° minus the solar zenith angle.
<i>Solar Incidence Angle (i)</i>	Angle from the zenith to the sun; same as the solar zenith angle.
<i>Local Incidence Angle (τ)</i>	The solar incidence angle referred to the local surface normal instead of the global zenith.
<i>View Angle (v)</i>	The angle in the principal plane above the sea-level horizon: 0° is the sun-facing direction.
<i>Shading</i>	Refers to the variations in lighting at all scales that result from changes in incidence angle.
<i>Shadow</i>	Refers to the darkness in lighting at all scales that result from the cutting off of direct illumination.
<i>Texture</i>	Surface roughness unresolved at the measurement scale.
<i>Topography</i>	Surface roughness resolved at the measurement scale.
<i>Radiance Mismatch</i>	The difference between the predicted and the CCD measured radiance.
<i>Geometric Mismatch</i>	The difference between the physical surface and the computer-simulated surface.

<i>Residual image</i>	The radiance difference image, which is the difference between the predicted and the CCD measured radiance normalized by the local predicted radiance.
<i>Single-scattering (SS)</i>	Represents the direct-reflectance component leaving each pixel: $W\text{cm}^{-2}$.
<i>Multiple-scattering (MS)</i>	Represents the light reflected more than once: $W\text{cm}^{-2}$.
<i>Relative MS (MS_R)</i>	MS normalized by the radiosity at each pixel. (dimensionless).
<i>Absolute MS (MS_A)</i>	MS normalized by the maximum radiosity in the image. (dimensionless).
<i>Maximum of MS_R</i>	Maximum value of the relative multiple-scattering component MS_R : $W\text{cm}^{-2}$.
<i>Maximum of MS_A</i>	Maximum value of the absolute multiple-scattering component MS_A : $W\text{cm}^{-2}$.
<i>Areas for which $MS_R/B > 5\%$</i>	The pixels (the fraction of the scene) where the relative multiple scattering is greater than 5% of the radiosity (dimensionless).
<i>Areas for which $MS_A/B > 5\%$</i>	The pixels (the fraction of the scene) where the absolute multiple scattering is greater than 5% of the radiosity (dimensionless).

Offset and Slope

Used in context of Chapter 4. It is the offset and slope terms defining the linear equation of Power-law spectra of a surface roughness.

LIST OF ABBREVIATIONS

L	Radiance
B	Radiosity.
T	Emittance.
SS	Single-scattering component.
MS	Multiple-scattering component.
BRDF	Bidirectional reflectance distribution function.
E_i , E_j	Surface elements i , or j .
A_{dw}	Atmospheric down-welling irradiance.
A_{uw}	Atmospheric up-welling irradiance.
F_A	Fraction of down-welling scattering over irradiance.
dE_i	Derivative of surface element i .
dA_i	Area of element i .
d	Distance between the two surface element, i and j .
$F_{dE_j - dE_i}$	Form factor of element dE_j to dE_i .
θ	Projection angle between the normal of a surface element and line linking the pair of elements together.
α	Facing angle between two surface elements.
β	Projection angle of a surface element on horizontal plane (slope angle of a surface element).

γ	Rotation angle defined as the azimuth angle of a surface element relative to the normal of other surface element
τ	The local solar incidence angle of a surface element.
s	Slope of terrain.
z	Azimuth angle of terrain (terrain slope orientation).

ACKNOWLEDGMENTS

I wish to thank the members of my dissertation committee, Drs Yasuo Kugo, John Booker, Bernard Hallet, John Adams, and Alan Gillespie for advice and contributions towards my research. In particular I would like to thank Dr. Gillespie for continued financial support and helpful advice throughout the course of this research. Many of the ideas suggested by Dr. Gillespie have helped and enabled me to select my research topic, to establish my research confidence, to exploit the scientific key problems, and to finish my research smoothly. His open-mindedness and interest in a large variety of topics have enabled me to pursue my research projects without much difficulty and have exposed me to a variety of other equally interesting subjects. I would also like to thank Dr. Robin Weeks for his invaluable suggestions, advice, and help solving many interesting scientific problems. In addition, I would like to thank Steven Cothorn and Bill Gustafson for programming assistance and for maintaining computer system operations.

I would also like to express my thanks to other members of the geological remote sensing laboratory for the friendship and guidance they have provided during the last five years: Doug Clark, Degui Gu, Don Sabol, Gail Yamada, Ginger Vogler, Kyle Blande, Milton Smith, and Steve Thompson. They help to make the last five years some of the most rewarding and enlightening years of my life. Thanks are extended to the secretary of the Department of Geological Sciences. Bernie Anderson, for her numerous efforts to make life easier for me.

Finally, I would like to thank my family: Liping Zou, my wife for her unconditional spiritual and emotional support throughout my five-year study, and for her help with my two lovely sons, Gary Li and Alan Li. In particular, I would like to thank my parents and parents-in-law for helping us take care of my two young sons for almost four years.

This research has been supported by NASA Contracts 5-31372 (EOS/ASTER) and 958450(SIR-C).

INTRODUCTION

The purpose of my doctoral research was to pioneer a method for removing multiple-scattering effects from images, and for using these effects to help characterize land surfaces. A major goal of terrestrial remote sensing is the mapping of plant communities, geologic units, and attributes of these units such as forest type and maturity, lithology and weathering, degree of soil development, and the changes of these properties in space and time (Schaber et al., 1976; Brown and Scholz, 1985; Franklin et al., 1986; Borengasser et al., 1988; Borengasser and Taranik, 1988; Evans and Smith, 1991; Bonan, 1993). In order to achieve these goals it is necessary to determine the reflectivity (ρ) of the land surface, and also, the land-surface structure (e.g., roughness and/or topography). However, remotely sensed measurements are of radiant fluxes (photons per unit time, Watt) measured through the earth's atmosphere, and commonly scaled into integer digital numbers (DN) in a range of 0-255. Therefore, the data must be calibrated to account for instrument factors if they are to be expressed in units of radiance, and to account for irradiance and atmospheric effects if they are to yield reflectance or reflectivity (Kaufman, 1988; Moran et al., 1990; Kaufman and Holben, 1993; Hallum, 1993; Myneni and Asrar, 1994). The reflectivity spectra of materials in a scene can be measured in a laboratory setting and used for this purpose. A problem which has not been accounted for in this process is that remotely sensed reflectances for many scenes are strongly affected by multiple-scattering effects caused by surface roughness and topography -- features not present in the laboratory (Li et al., 1996). Even the "color" of a surface, largely controlled by its reflectivity spectrum, may differ from the laboratory to the field due to multiple scattering from neighboring surface elements. These effects, which may amount to ~20% of the total measured signal for rugged terrain (e.g. Bluff Creek area, California) and as much as ~50% for rough-textured surfaces (i.e., gravel bar at the subpixel scale), must be corrected if reflectance is to be converted to reflectivity for comparison to

spectral information, or if accurate maps are to be made from remotely sensed images. Such correction is not made now.

The difficulty in extracting scene reflectivities and roughness from images is that surface reflectivity, scene texture (subpixel-scale surface structure) and topography (pixel-scale terrain) influence the surface brightness simultaneously, so that the inversion for any desired parameter is under-determined. The reflectivity controls the brightness directly, whereas the terrain roughness at all scales affects brightness by: (1) reducing the illumination due to shading (foreshortening and shadowing) and (2) increasing the illumination due to multiple reflection. The first overall goal of my research is to improve methods for estimating reflectivity by correcting measured brightness for unresolved shading, and for multiple scattering (MS) at all scales. The second goal is to estimate surface roughness from remotely sensed data, minimizing ambiguity and uncertainty in the inversion.

I have separated my research in three main parts: 1) developing and testing a practical hybrid radiosity model with which to predict multiple scattering for different situations; 2) developing algorithms to estimate reflectivity and surface roughness from images; and 3) applying these models to forests and unvegetated landforms.

The main part of the dissertation is divided into five chapters: the radiosity model; a discussion of multiple scattering at two scales; validation of the radiosity model; estimation of surface roughness; and topographic correction in vegetated areas. The first three chapters are focused on model generation, verification, and primary results; last two are focused on applications of the radiosity model in the separation of surface reflectivity and surface roughness.

Radiosity is a computer-graphics term for describing the total radiance from a diffuse surface, consisting of a directly reflected component and a multiple-scattering

component integrated over the hemisphere of the sky (Cohen and Wallace, 1993). (In most studies only the direct term is considered). In Chapter 1, I present the basic methodology of developing the new hybrid radiosity model used to characterize and compute the radiosity from a complicated natural surface, as represented by digital terrain models, or DTMs. This practical radiosity model is based on an efficient algorithm with which to compute a geometric “form factor.” In terms of accuracy and computation speed, this is the central challenge in coding the radiosity model. The form-factor algorithm combines three existing methods: the double-contour integral (DCI), half-contour integral (HCI), and element-to-element (EE) methods. These three algorithms are listed in decreasing order of precision, and increasing order of computing time. My contribution to radiosity modeling was to develop a sophisticated method with which to select the best of the three algorithms, pixel by pixel, by balancing the desired output precision and required computing times. A threshold distance is predetermined for selecting the algorithm for each form-factor calculation.

First, model results are presented in Chapter 2. The radiosity model is used to make quantitative estimates of the multiple scattering for a range of surfaces, at visible near-infrared (VNIR) and thermal infrared (8-12 mm) wavelengths. These results establish the importance of correction for multiple scattering at the pixel scale of Landsat imagery, which can account for as much as 20% of the total brightness. DTMs of rugged terrain of Bluff Creek, northern California, and a rough gravel bar surface, were used to define test surfaces to demonstrate the multiple-scattering effect at pixel and subpixel scales, respectively. The results show the spatial distribution of multiple scattering (MS) over a surface as a function of surface roughness, surface reflectivity, illumination geometry, and sky illumination.

In order to evaluate the reliability and precision of the new hybrid radiosity model, laboratory radiance measurements of physical surfaces were made and compared to the radiance calculated by the model. In Chapter 3, two types of test surfaces, made from

white board, and plaster (both close to ideal Lambertian surfaces), were analyzed. The radiances were measured using a CCD camera, and the CCD images were registered to digital DTMs of the surfaces. Comparisons of the predicted and the measured results were made by direct matching of results, analysis of mismatches, and analysis of local MS effects normalized to the effects integrated over the image. After accounting for systematic and random errors caused by the artifacts and laboratory equipment, the comparisons show a high degree of consistency that validates the radiosity model.

Once validated, the radiosity model was used to retrieve a surface roughness parameter from a Landsat TM image. Chapter 4 presents a new inversion model (“semi-empirical inversion”) based on the foreground/background analysis (FBA) algorithm (Smith, et al., 1996). Basically, the semi-empirical inversion model uses an optimized finite impulse response (FIR) filter to estimate the roughness of a geological surface using the radiosity model. The inversion is conducted on an image using the FIR filter operating in the spectral dimension. The FIR filter was optimized using radiosity model calculations based on the laboratory reflectivity spectra of natural materials and simulated rough surfaces, rather than on image data or field data, as in other studies. Compared with three other roughness inversion methods, the new semi-empirical method demonstrated better accuracy and stability. In this study, a TM image of Death Valley was chosen as a test site because of the advantages discussed in Chapter 4.

In Chapter 5, I applied the radiosity model to separate the spectral and roughness information in a image in order to improve methods of topographic correction. As an example, the densely forested, rugged Bluff Creek watershed in northern California was chosen. Based on the anisotropic reflectance of the vegetated surface, a special case of the bi-directional reflectance distribution function (BRDF) dependent on the both local incidence and slope angles, as well as subpixel roughness, was calculated using the radiosity model. The modified BRDF is known as the canopy function (CF). The CF varies with many parameters, such as subpixel surface structure (tree shape), surface

reflectivity, canopy density (tree spacing), and illumination geometry. Topographic correction using the CF applied to a simple surface model demonstrates that the CF is a proper, reliable and theoretically based model of surface reflectance. Comparisons with three other methods of topographic correction show that the CF approach is the most reliable, even at low sun elevation angles for which corrections are large. The CF can be recalculated for different types of surfaces, but it takes a long time; hence the CF method is more difficult to use than simple methods of topographic correction, although it is easier to use than full BRDF correction

CHAPTER 1: RADIOSITY MODEL

INTRODUCTION

The increasing demand for high-precision remotely sensed images has created a need to understand and model the basic physical process of electro-magnetic waves interacting with complicated natural surfaces, with a higher level of accuracy than before (Teillet et al., 1982; Lee and Kaufman, 1986; Lepriuer et al., 1988; Proy et al., 1989). This need is driven in large by the requirement to extract intrinsic reflectivities, devoid of the effects of lighting condition and geometries, and devoid of the effects of surface textures and terrain roughness. This information is required for comparison of remotely sensed reflectivities to laboratory spectral measurements, and hence is a basic requirement for robust image classification and for the identification of surface materials.

Models that predict radiance budgets must account for secondary irradiance scattered onto a surface element after one or more reflections from nearby surfaces. The total radiance from the surface element, consisting of the reflected direct sunlight and the reflected secondary irradiance, is called "radiosity," and the models that predict it are called radiosity models.

Radiosity models were originally developed in the engineering and computer graphics fields and have been successfully applied to calculate total radiate energy from simulated surfaces. The greatest use of the radiosity model has been for synthesizing image, especially for architecture, interior design, light engineering, and advertising (Nishita and Nakamae, 1985; Christensen, 1992). Recently, it has been introduced into remote-sensing studies (Borel et al., 1991; Borel and Gerstl, 1992; 1994a; 1994b). Most primary applications in remote sensing have been focused on predicting the reflectance

from vegetation with the simple geometric surface modes (Gerstl and Borel, 1992). However, little attention has been given to natural surfaces .

Existing radiosity models have been mostly used for relatively simple surfaces and were designed to minimize computation time (Baum et al., 1989; Cohen and Greenberg, 1985; Smits et al., 1992; Gortler et al., 1993; Troutman and Max, 1993). Numerous approximation algorithms have been developed to solve radiosity calculations more efficiently, without sacrificing accuracy, but these have limited application for complicated natural surfaces, for example as represented by DTMs. For these natural surfaces, none of the radiosity methods yields both acceptable accuracy and speed. Thus, the need to apply radiosity models to actual images has created a need for computationally efficient implementation on readily available computers.

A central problem in radiosity modeling is to calculate form factors, which are defined as the fraction of light leaving one surface element and reaching another. The full solution for finding form factors is complicated and time-consuming. There are three basic formulas: a closed solution method using double-contour integral for polygon (a finite element) to polygon; a semi-approximation method using half-contour integral for polygon to differential element; and an approximation method, using differential equation, for differential element to differential element. The double-contour integral method (Schröder and Hanrahan, 1993) is the most computationally intensive, but offers the greatest accuracy. The half-contour integral method (Ashdown, 1994) and element-to-element techniques (Siegel and Howell, 1992) offer progressively greater savings and may be used for less-demanding situations.

Most radiosity models were derived from the differential equation by treating the surfaces as differential elements, and therefore contain inevitable approximation errors, especially for adjacent surface elements (Cohen and Greenberg, 1985; Baum et al. 1989; Wallace et al., 1987; Cohen and Wallace, 1993). To minimize the approximation errors

within affordable computation, I have examined existing radiosity algorithms and developed a radiosity model that is accurate, precise, computationally efficient, and suitable for complex surfaces. Accuracy and precision estimates are 1-2% of the maximum radiosity in a scene, or roughly 2-4 DN values if the dynamic range of the sensor is matched to the distribution of radiance measurements. To achieve this performance, the acceleration of model relies on the selection among the three different basic form-factor algorithms as appropriate for a given local geometry. Therefore, a new radiosity model, hybridized from the three existing radiosity methods, was developed through careful analysis of overall radiosity precision as well as computation speed.

PREVIOUS WORK

Several theoretical models have been developed and used in remote sensing to predict the radiance of natural surfaces (Li and Strahler, 1985; Borel et al., 1991; He et al., 1992; Kusk, 1994). The ray-tracing model is a form of radiative-transfer model. It provides a straightforward means to predict the radiance reflected from each point of an image, tracing a visual ray from a sensor into the scene. It has been widely and successfully used for specular surfaces. (Shinya et al., 1987; Wallace, et al., 1987; 1989; Shirley, 1990; Watt, 1990). However, the model for non-specular surfaces is time consuming and impractical (Greenberg, 1989).

To avoid complicated numerical computation, Li and Strahler (1985, 1986, 1992) developed a geometric-optical model by using the “geometric projection fraction” of each object on a flat surface to predict the apparent reflectance from a surface. Primarily, their model was used to predict the bi-directional reflectance distribution function (BRDF) for vegetated surfaces (Li and Strahler, 1985, 1986, 1992; Woodcock et al., 1994). A major limitation of accuracy is due to its strategy of projecting 3-D objects onto a 2-D surface to calculate the geometric area fraction (the “geometric fraction”). Because the geometric-

optical model lacks the ability to handle complicated geometries, with light bouncing among many surface elements, it cannot predict shading and the amount of multiple scattering well (Li et al., 1995).

In contrast to the ray-tracing and geometric-optical models, radiosity models are designed to calculate the total radiance from a diffused surface (Lambertian surface). Without considering the directional variation of surface reflectivity, the computations are much simpler and more practical in terms of coding and speed. The radiosity model has the attractive characteristic of providing a view-independent solution (Wallace, et al., 1987,1989; Shirley, 1990). Thus, it is attractive for remote sensing, because natural surfaces have great amount of diffuse reflected radiation at some scales.

Radiosity has been studied for thirty years, and with increasing frequency during the past decade. Most research has focused on developing efficient methods to calculate the form factor, the parameter at the core of the model. A number of different approaches have been developed, most relying on approximate solution for the form factor to reduce the otherwise prohibitive computation time. These methods include: the hemi-cube algorithm (Cohen, and Greenberg, 1985; Cohen and Wallace, 1993), the cubic tetrahedron algorithms (Ashdown, 1994), Nusselt's analogy (Cohen and Wallace, 1993), the single-plane method (Sillion and Puech, 1989), the Monte Carlo ray-tracing method (Malley, 1988), and the area-sampling method (Wallace et al., 1989). These approximation algorithms are all essentially based on the same basic form factor formulation used in the element-to-element approach. Thus, all contain inevitable errors, especially for radiance from nearby pixels.

Of the approximation algorithms, the hemi-cube algorithm is the most commonly used. In it, a hemi-cube (a half cube) is placed around a differential element, with the hemi-cube faces divided into small grid cells. Each grid defines a direction and a solid angle. A differential form factor, dF , is computed for each cell based on its size. Only

one eighth of the delta form-factors need be computed, due to symmetry (one eighth of the top face and half of one side face). These delta form factor are precomputed and stored in a lookup table (Cohen, and Greenberg, 1985). Two important kinds of error are associated with this approach: aliasing due to projection (Ashdown, 1994), and approximation by the element-to-element algorithm. These errors increase with decreasing the distance between two elements.

Only recently has a full solution for the form factor been achieved. Schröder and Hanrahan (1993) used the double contour-integral method to solve the form-factor equation numerically. Its solution has been coded with both C and Mathematica for direct application. The major drawback of the algorithm is that it is computation-intensive. A scene of 100x100 pixels, for example, requires more than 20 hours to process using a DEC-Alpha station with a 276-Mhz processor. Therefore, the double contour-integral method is impractical for most image applications.

RADIOSITY MODEL

The radiosity model is based on the radiative heat transfer theory, for predicting the radiant interchange between surfaces (Siegel and Howell, 1992; Cohen and Wallace, 1993). The radiance leaving a surface element is determined by the direct illumination and ambient light from neighboring surface elements. Originally, the radiosity model was designed only for Lambertian diffuse reflection; subsequent work has extended the model to glossy and specular (mirror) reflection (Shirley, 1990; Aupperle and Hanrahan, 1993). In this study, I develop an efficient radiosity model for natural Lambertian surfaces.

A Lambertian surface is defined such that its directional reflectance is an isotropic function of the irradiance weighted by the cosine of the local incidence angle and surface reflectivity $L = I_{\tau} \rho \cos(\tau)$. The brightness of the surface is independent of the viewing angle. The Lambertian assumption enables the radiosity model to compute the energy

balance among surfaces efficiently and in a way that is independent of view angle. These simplifications must be abandoned if the surface is non-Lambertian. Even for Lambertian surfaces, the viewer-surface-illumination geometry must be specified in order to compute radiance, but most of the computation of form factors has been completed before selection of viewing position.

Multiple scattering (MS) is a major source of light reflected to the viewer, in addition to the single-scattering component. MS describes the diffuse light bounced between any pair of surface elements.

To describe the spatial distribution of MS effects in an image quantitatively, the image is generally divided into many small cells. Any radiosity function over a complex surface can be estimated by linearly summing the basic functions over a simple array of finite elements. The contribution of each basic function to the radiosity is therefore determined by values computed at a finite number of locations, or cells.

RADIOSITY THEORY

Radiosity (B), or exitance, is the total energy per unit area (Wcm^{-2}) leaving a surface, including the thermal emittance (T), single-scattering (SS) and multiple-scattering (MS) components (Figure 1). It is similar to irradiance, which describes the total energy per unit area arriving on the surface. Its concise formula can be written as

$$B_i = T_i + SS_i + MS_i \quad i = 1, 2, 3, \dots, n \quad (1)$$

The first term (T) represents all thermal energy released from the surface; the second term (SS) is single-scattering radiance, includes all first-order reflectance; and the third term (MS) is the multiple-scattering component, which is the energy bounced one or

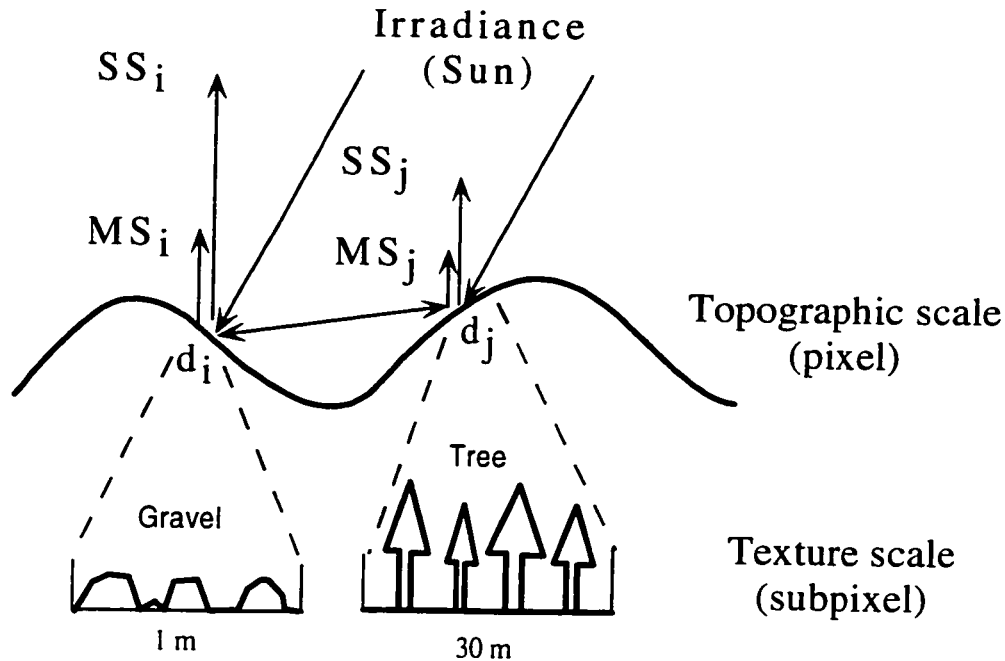


Figure 1. Schematic diagram shows the geometric relation of radiosity with components: single scattering, and multiple scattering components, and roughness at Landsat TM pixel and subpixel scales. At the pixel (30-m) scale, roughness is topographic and is described by DTMs. At the subpixel scale, roughness is textural; typical scale lengths vary widely with terrain.

more times among surface elements. Emittance, the radiation of a surface, is the function of the emissivity and surface temperature, and the first-order reflectance is the light incident on the tilted surfaces. One of the complexities of the radiosity model is the calculation of multiple scattering. The amount of light reflected from adjacent surface elements is determined by the geometric relation of those elements, or how they view each other. The full radiosity model is then written as

$$B_i = T_i + \rho_i * (I_{rr}) * \text{Cos}(\tau_i) + \rho_i * \sum_{j=1}^n B_j * F_{i,j} \quad (2)$$

where ρ_i is surface reflectivity; I_{rr} is Irradiance; τ_i is incidence angle; $F_{i,j}$ is the form-factor. This is a typical form of the radiosity equation as used in computer graphics and

engineering fields. Rearranging the radiosity equation, the n linear equations can be derived, and written in a matrix expression:

$$\begin{bmatrix} 1 - \rho_1 F_{1,1} & \dots & \dots & -\rho_1 F_{1,n} \\ -\rho_2 F_{2,1} & \dots & \dots & -\rho_2 F_{2,n} \\ \dots & & & \dots \\ \dots & & & \dots \\ -\rho_n F_{n,1} & \dots & \dots & 1 - \rho_n F_{n,n} \end{bmatrix} \begin{bmatrix} B_1 \\ B_2 \\ \dots \\ \dots \\ B_n \end{bmatrix} = \begin{bmatrix} T_1 + SS_1 \\ T_2 + SS_2 \\ \dots \\ \dots \\ T_n + SS_n \end{bmatrix} \quad (3)$$

where $SS_i = \rho_i * (I + A_{dw}) * \cos(\tau_i)$ and A_{dw} is downwelling scattering component. There are n unknown radiosities in the n linear equations, associated with the individual pixels in the neighborhood of pixel i . The SS terms as known variables, calculated from the irradiance, surface reflectivities, and local incidence angles (τ_i), and the data kernel (linear-equation coefficient matrix) which represents the geometric position ($F_{i,j}$) for each pixel is determined before-hand. Solving for the data kernel is a key step of the radiosity model and discussed in detail below.

FORM-FACTOR CALCULATION

In describing the simple case of radiance from one point to another, the form factor takes its most basic form, written in equation (4) and illustrated in Figure 2:

$$F_{dE_j - dE_i} = \frac{\cos(\theta_i) * \cos(\theta_j)}{d^2 * \pi} * dA_i \quad (4)$$

where $F_{dE_j - dE_i}$ is the form factor of element dE_j to dE_i ; θ is the projection angle between the normal of a surface element and line linking the pair of elements together; dA_i is the area of element i ; and d is the distance between the two.

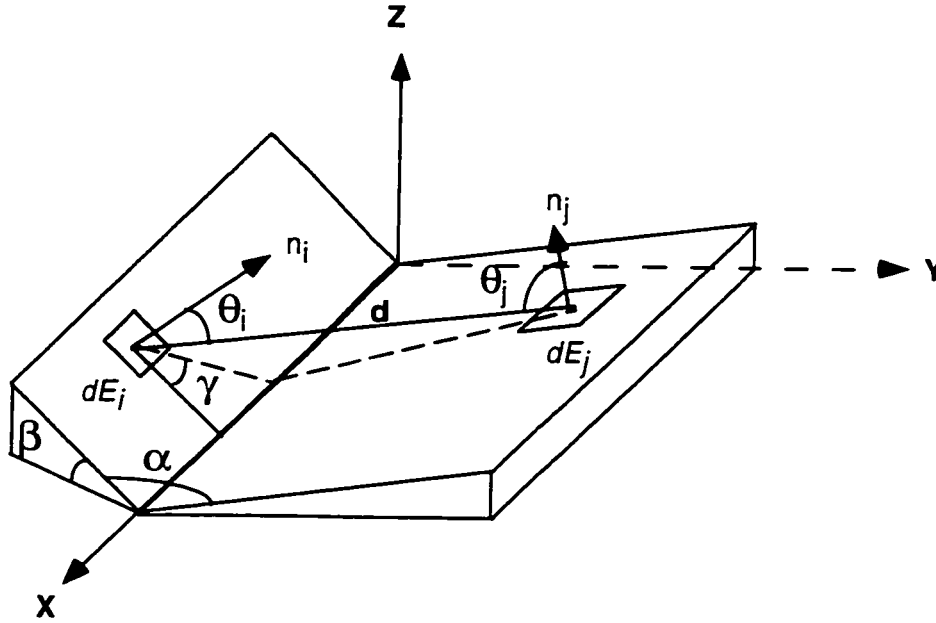


Figure 2. Schematic plot for illustrating the definition of symbols used in the radiosity model.

In considering a form factor for one finite area to another, both θ_i and θ_j angles, and distance in equation (4) will change with each point within the area elements, and therefore, integration is required. Normally, for two arbitrary surface elements in 3-D space, integration must be performed six times along each of the X-, Y-, and Z-axes for both areas. Then equation (4) becomes

$$F_{j-i} = \int_{z_i, y_i, x_i} \int_{z_j, y_j, x_j} \frac{\cos(\theta_i) * \cos(\theta_j)}{\pi * d^2} * dx_i dy_i dz_i dx_j dy_j dz_j \quad (5)$$

Solving equation (5) is complicated and time-consuming (Hamilton and Morgan, 1960). "Full solution has required most of the 230 years since Lambert's pioneering efforts," summarized on page 267 Ashdown (1994). There are two fundamental approaches: numerical and analytic methods. The closed-form solutions are mostly applied for simple geometric shapes of polygons (Siegel and Howell, 1992). Analytic methods are more efficient in terms of computation, but have less accuracy.

A HYBRID RADIOSITY MODEL FOR NATURAL SURFACES

The hybrid radiosity model consists of four main procedures, which are outlined in a flow diagram in Figure 3. They are: 1) modeling the topography with DTMs; 2) determining the form factor (using the hybrid algorithm); 3) solving the radiosity equations iteratively; and 4) displaying the results.

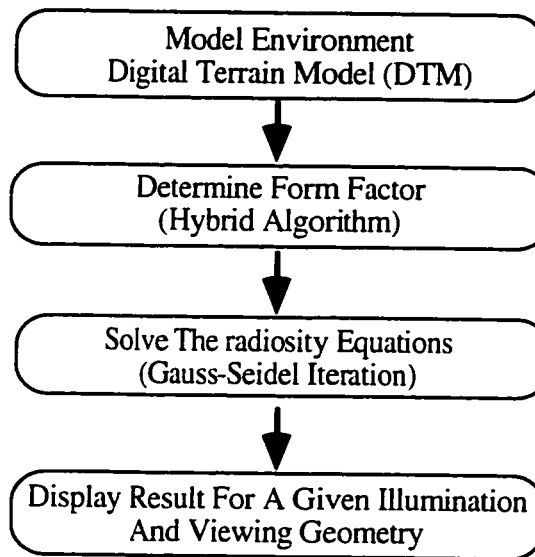


Figure 3. Flow chart shows the major procedures in the radiosity mode.

MODELING THE ENVIRONMENT

Finite surface structure

Digital terrain models (DTMs) are used in the radiosity model to represent the topographic structure of natural surfaces. The DTMs use a predetermined mesh template to map the topography. This template is a predefined subdivision into standard elements, usually a rectangular grid. The chief advantage of the subdivision algorithm is that it generates perfectly regular, well-shaped elements. The mesh template is the only surface structure commonly available for representing natural surfaces. However, this meshing method inevitably generates some inaccurate elements where the template intersects natural boundaries.

Each element can be characterized in two ways. One uses the four corner values directly to represent the surface element, which is not flat but curved. The other way uses the normal vector, the average height, and the area of a best-fit plane controlled by the elevation at the four corners. The normal vector was calculated using a cross-product algorithm, and the average height and area were calculated for the best-fit plane. These two methods were selectively used for calculating form factors with different form-factor methods. Using the double-contour integral method requires the four corner values, and using the element-to-element method requires both the normal vector and the height of the best-fit surface.

The radiosity was calculated for each surface element by assuming the surface was flat. Both methods (double-contour integral and element-to-element) are sensitive to this assumption, and therefore the calculated radiosity is erroneous to some degree. The validity of the approximation, and the accuracy of the calculated radiosity, depend on the spacing of the DTM grid as well as its vertical resolution. In general, the finer the DTM resolution, the better the radiosity results.

Visibility determination

One of the factors determining multiple scattering is the “visibility function” (view blocking) of an element as viewed from adjacent pixels. The mutual illumination between a pair of pixels requires that they face each other, and that the mutual view is unimpeded by intervening topography. Therefore, before calculating the form-factor, the visibility function must be determined for the whole image. This visibility function is a binary field (“true” or “false”), and depends on the normal and height of each surface element. The visibility function controls the number of pixels involved in the form-factor calculation, and hence affects the total computation time.

There are two steps in determining the visibility function. The first step is to check if a given pair of pixels face each other, based on the angle between the surface normal

vectors. If this facing angle is less than 180° , they potentially can see each other; otherwise they cannot. The second step is to determine if the view between pixels is impeded by surface elements between them. After calculation of the binary visibility-function image we may proceed with the form-factor calculation.

For most natural surfaces at remote-sensing scales (10-100 m), typically fewer than half the pixels in the image are visible from a given position, because of the blocking by intervening hills. Usually, the rougher the surface, the fewer the “visible” pixels, and the shorter the calculation time required to calculate the form factor. Consequently, the radiosity model runs faster for rough than the smooth surfaces.

Errors in the visibility function may be caused by the discontinuity between the fitted plane at each pixel. Using the center height of each pixel to determine if the view is blocked results in overestimating or underestimating the height at an edge; hence the blocking factor may also be in error. These errors mostly occur along the edges of blocking terrain features. Their effect in the radiosity image is the geometric distortion of the pattern and errors in the calculated multiple scattering.

DETERMINING THE FORM FACTOR (HYBRID FORM-FACTOR METHOD)

Three approaches to determine the form factor

In this section, three methods of solving for the form factor are explained briefly. In order of decreasing precision, they are the double-contour integral (DCI), half-contour integral (HCI), and element-to-element (EE) methods.

Double-contour integral (DCI) method

One mathematical solution of equation (5) is called the double-contour integral method, which treats the problem as an exchange of energy between two finite areas. Instead of integrating in three directions (X, Y, Z axis) over each surface area, a double-

contour integration is applied to convert equation (5) to two line integrals along the boundary of each polygon, by two applications of Stokes' theorem (Sparrow and Cess, 1978). Through a series of complicated mathematical manipulations (Sparrow, 1963), equation (5) becomes

$$A_j F_{j-i} = \frac{1}{2\pi} \oint_{c_i, c_j} (\oint \ln S dx_j) dx_i + \frac{1}{2\pi} \oint_{c_i, c_j} (\oint \ln S dy_j) dy_i + \frac{1}{2\pi} \oint_{c_i, c_j} (\oint \ln S dz_j) dz_i \quad (6)$$

where c_i and c_j are the boundaries of the two surface elements and S is a complete function (see Schröder and Hanrahan, 1993). Schröder and Hanrahan (1993) were the first to solve this equation and to give the full solution for the form factor for any two polygons of arbitrary shape, coded in *Mathematica* and *C* computer languages. Their full solution is too complicated for presentation here. As a courtesy from Schröder (P. Schröder, pers. Comm. 1995), I have incorporated the *C* code implementing the double-contour integral method in my radiosity computer program.

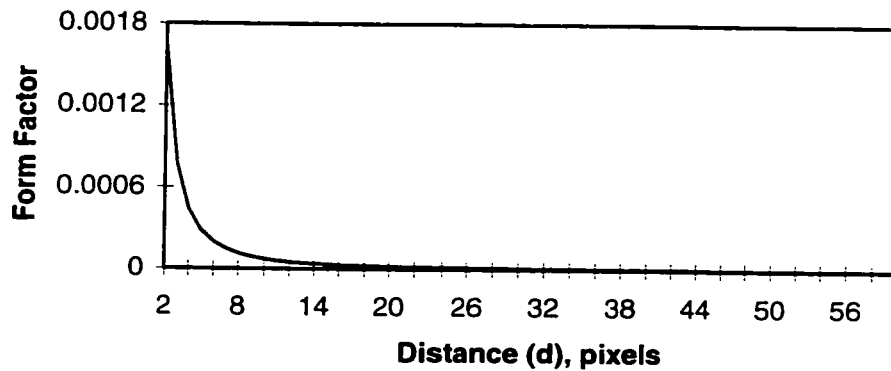


Figure 4. Form factor vs. distance calculated by the double-contour integral method for the case: $\alpha = 150^\circ$, $\theta_i = 75^\circ$, and $\beta = 10^\circ$. Maximum value of the form factor is 1 (parallel elements facing each other at close range).

For a given image, the time required to calculate the whole form factor increases exponentially with the size of the image. For an image (50x50 pixels), calculation of 10^5

complete form factors required 740 seconds CPU time on a DEC-Alpha 3000 computer, with a 276-Mhz processor. The value of the form factor decreases quadratically with the distance between the two elements, indicating the effect of bounce light from an adjacent scene element is rapidly reduced with distance (Figure 4).

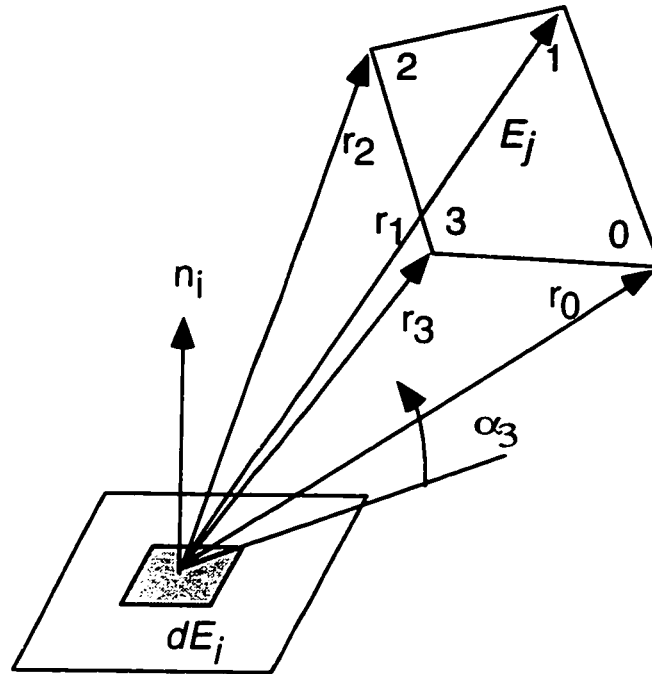


Figure 5. Schematic plot for the half-contour integral algorithm, adapted from Ashdown.

Half-contour integral (HCI) method

The half-contour integral method treats the radiosity exchange as from a differential element to a finite area, therefore reducing equation (5) to three integrals applied only on the finite area. Ashdown (1994) solves the triple integral numerically, yielding

$$F_{dE_i, -E_j} = \frac{1}{2\pi} \sum_{k=0}^{n-1} \varphi_k \cos \psi_k \quad (7)$$

or

$$F_{dE_i, -E_j} = \frac{1}{2\pi} \sum_{k=0}^{n-1} \varphi_k n_i (r_k * r_{(k+1)\%n}) \quad (8)$$

where n is the number of polygon edges; φ_k is the angle (in radians) between vectors r_k and $r_{(k+1)\%n}$ defined from dE_i to each pair of vertices k and $(k+1)\%n$ ($\%$ is the modulo arithmetic operator); ψ_k is the angle (in radians) between the plane of dE_i and the triangle formed by dE_i and the k th edge; and n_i is the normal of dE_i . Figure 5 provides a geometric context for equations 7 and 8. I have written C code for this algorithm.

Computation time was only 12 seconds, for the same set of form factors used in determining run time for the DCI method. Thus, the ACI method is faster by a factor of >60 than the DCI method.

Element-to-element (EE) method

Equation (4) is the basic form of the simplified form-factor method that treats the surface elements as points. Since it has the simplest form, it is the fastest algorithm. It can be used to approximate the form factor only when the distance between the pair of surface elements is sufficiently large to justify treating the elements as points. My radiosity program uses this method whenever this approximation does not result in errors larger than the precision requirement for the radiosity, set by the user.

The EE method took only 2 seconds CPU time for the same set of 10^5 form factors. It is six times faster than HCI and 320 times faster than DCI.

Variables affecting the form factor

The form factor is solely dependent on the five geometric variables relating the surface elements to each other (Figure 2): the two projection angles (θ_i and θ_j), the areas of the surface element dA_i and dA_j , and the distance between them (d). In practice, I use the facing angle (α) (to replace the projection angles θ_j), slope angle β and rotation

angle γ (to represent dA_i) in calculating the form factor, because from a physical point of view, α and θ_i are more convenient than the pair of projection angles (θ_j and θ_i) for describing the geometry of land-surface elements.

In order to understand how each variable affects the form factor, the functions relating the form factor to each variable are discussed in detail below, with respect to the basic form factor equation:

$$F_{dE_j - dE_i} = \frac{\cos(\theta_i) * \cos(\theta_j)}{\pi * d^2} * dA_i \quad (4)$$

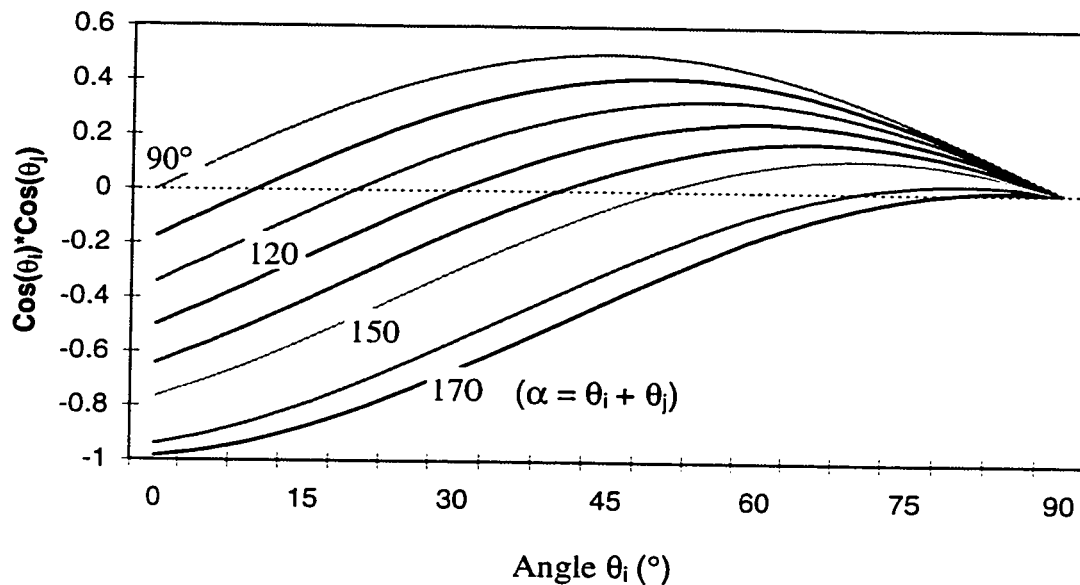


Figure 6. This diagram shows the basic cosine term of the form factor equation 4 as a function of the projection angle (θ_i) for facing angles (a) from 90° to 170° . The positive values indicate that the elements are visible to each other, whereas the negative values indicate the pair of elements cannot “see” each other.

Projection angles θ_i and θ_j

The two projection angles are closely related to the facing angle α and the rotation angle γ of the surface element (Figure 2). By definition, α is the angle between the two surface elements. In principle, α may range from 0° to 180° but, for most natural surfaces, it ranges between 90° (cliff) and 180° (horizontal plane). The rotation angle γ is defined as the azimuth of a surface element relative to the normal of other surface element. When $\gamma_i = 0$, both surface normals lie in the same plane, called the principal plane, and $\alpha = \theta_i + \theta_j$. There is a restricted relationship (dependency) between α and θ_i : if α is fixed, θ_i can vary only in a certain range; if the form factor is positive, the two elements are mutually visible. The relationship of the form factor, α and θ_i is plotted in Figure 6. The dependency of α and θ_i constrains the range of reasonable value of each angle.

Area of surface element E_i (dA_i)

Intuitively, the form factor $F_{dE_j-dE_i}$ ought to increase with dA_i , because the solid angle subtended by element E_i (viewed from E_j) increases with the area. For a given pixel, dA_i can be determined from the surface element slope β and rotation angles γ (Figure 2):

$$dA_i = \{\cos[\arctan(\cos \gamma \tan \beta)] * \cos[\arctan(\sin \gamma \tan \beta)]\}^{-1} \quad (5)$$

where β varies in the range of 0° to 90° , and γ is in the range of 0° to 45° (symmetric to principal plane). Area dA_i will be bigger than a pixel for $\beta > 0^\circ$. When $\gamma = 0^\circ$ both elements are in the principal plane and the target element E_i is fully facing E_j . In this orientation, the multiple scattering between E_i and E_j , and the relative errors attending its estimation (with respect to SS), are all maximized.

Distance (d)

The distance between the two elements is the dominant variable contributing to the form factor, which decreases quadratically with increasing d (Figure 5). The accuracy as well as the value of the form factor depends more on the distance than any other variable. One consequence is that, for most natural terrain surfaces, two patches can be treated as points when d is sufficiently large.

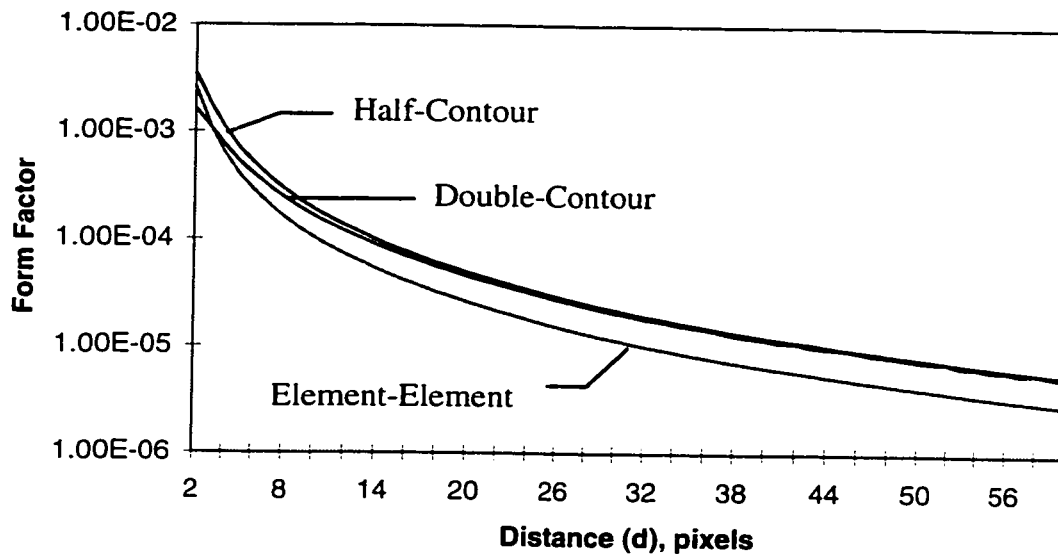


Figure 7. Form-factor values calculated using three different algorithms: double-contour integral (DCI), half-contour integral (HCI), and element-to-element (EE) methods. The DCI is the most accurate. The approximation errors using HCI decrease with the distance and the ones using EE is almost constant in the log-axis. The example is calculated using $\alpha = 150^\circ$, $\beta = 30^\circ$, and $\theta_i = 75^\circ$.

Comparing the three algorithms

Both the HCI and EE methods estimate the form factor by assuming that either one or both of the surface elements are points. That assumption can be justified when d

exceeds a threshold value that varies with the precision desired. Figure 7 shows the form factor as a function of the distance calculated using three algorithms. The approximation errors for the HCI method decrease rapidly with distance. After 15 pixels, there is almost no difference between the values found using the two algorithms. However, the form-factor error from the EE method is constant for the entire range of input parameters. There will be always an error in using EE method, no matter how far the two elements are apart.

This threshold distance does not only vary with the choice of algorithm, but also varies with the geometric variables discussed above. Careful selection of the threshold distance is the key to make the form-factor calculation efficient within the allowable precision. To select the proper algorithm for the form-factor calculation, the threshold distance value must first be calculated. In the next section, the detailed strategy for selecting the threshold is explained.

ALGORITHM SELECTION

The rule of the algorithm selection is to choose the fastest algorithm of the three within the desired accuracy. The threshold distance which gives the chosen errors (desired precision) is then calculated. A set of threshold distances was calculated for all variations of the geometric parameters (α , β , θ , and γ). These precalculated threshold distances are coded in a lookup table for use in selecting the best algorithm for each form-factor calculation.

To determine the accuracy for each form-factor calculation, the first step is to select the approximate radiosity precision for a given image. This precision, in turn, determines the limit of accuracy required for the each form-factor calculation.

$$B_i = \rho_i * I_r * \cos(\tau_i) + \rho_i \sum_{j=1}^n B_j * F_{i,j} \quad (9)$$

The radiosity, B_i (equation 9), is the function of surface reflectivity ρ , irradiance I_{rr} , local incidence angle τ_i , and form factors $F_{i,j}$. Assuming all these variables are constant for a homogenous surface, except the summation of form factors, which must be approximated. Thus, the accuracy of the calculated radiosity depends on the sum of form factor precision.

Figure 7 shows the form factors calculated by the three algorithms as a function of distance. The difference between the approximation algorithms (HCI and EE) and DCI are the errors: positive caused by HCI and negative caused by EE with respect to DCI. When an element receives all bounce light from its neighbors, the error of its form factors in sum is compounded from all the individual of each form factor. When a precision is specified for the predicted radiance, the implied uncertainty for each individual form factor is actually much smaller. This required precision is really dependent on how many form factors must be summed in equation 9. Since the number changes from pixel to pixel, it must be estimated statistically.

In application, the maximum field of view must be determined before calculating the form factor precision. The number of elements (N_d) that are in the field of view and within the distance (d) is given by: $N_d = (2 * d + 1)^2 - 1$. If all pixels are assumed to be visible to each other, the number (N_f) of the form factors is then $N_f = [(2 * d + 1)^{2*2}] / 2$, where the denominator 2 account for the form-factor reciprocity for any pair of elements. For example, if the distance of viewing field is 10 pixels (thus, the image is 21x21 pixels), the total number of elements is 440 pixels, and the total number of form factors is $\leq 97,240$.

For natural terrain surfaces, however, many topographic depressions are enclosed on only two sides, such that only half of the above number of elements must be considered. Again, because the form factor decreases quadratically with distance, for $d >$

60 pixels (1800 m for 30-m resolution), the form-factor value is $< 10^{-8}$. This amount is negligible; therefore, I have chosen 60 pixels as a cutoff boundary for the field of view, and radiance from beyond that distance is neglected.

Determining the threshold distance that accounts for all possible geometries of a pair of elements requires a 5-D lookup table: facing angle α , projection angle q_i , element slope angle b , and rotation angles g . To reduce the number of variables, I have fixed $g = 0$, where the form-factor estimation error is maximum for all range of g . This is the case in which both surface elements are in principal plane. Thus, the reduced lookup table is 4-dimensional.

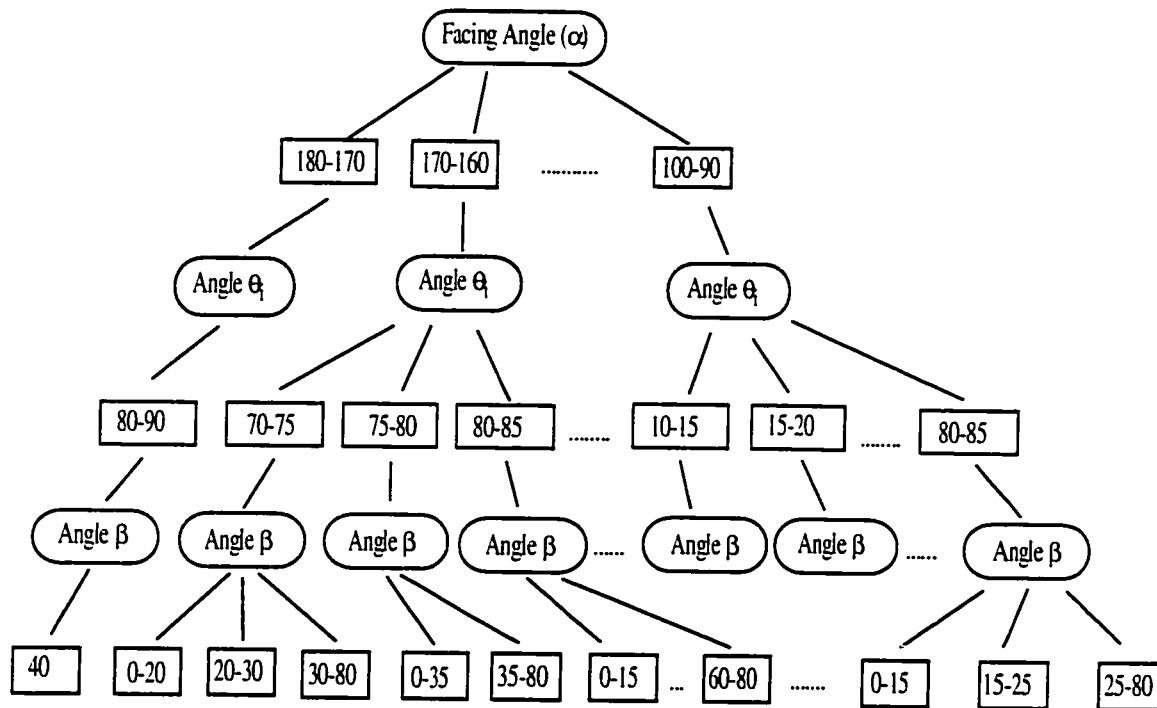


Figure 8. Schematic flow chart illustrating a hierarchy structure for classifying the geometric orientation of a pair of elements into simple categories. For each case, the threshold distance value is evaluated for a specified form-factor precision. All the values in the chart are angles in degrees.

Determining the threshold values depends on evaluating the cumulative errors in the several geometric categories. These categories can be represented as the tree structure shown in Figure 8. Starting from the top node of the tree, the facing angle α was divided from 180° to 100° (the most common situations) in intervals of 10° , and θ_i and β were divided from 45° to 0° in intervals of 5° . All the intervals were chosen with considerations of computational speed and form-factor approximation accuracy. Thus, there are about 400 cases (in which the form factor is positive, Figure 6) of geometry of two elements for evaluating the threshold distance values. Calculating all the form factors in the 60-pixel neighborhood, using both HCI and DCI; taking their difference multiplied by the total number of surface elements within distance d ; and then summing up all the differences in the 60-pixel range (cutoff point), the cumulative errors for the radiosity for each distance value were obtained. Thus, for each different accuracy requirement, the corresponding distance threshold can be calculated. A lookup table was then established for the hybrid radiosity model calculation.

Based on the threshold values in the lookup table, the primary choice of the form-factor algorithms is between the DCI and HCI methods, because there in lies the greatest savings in computation time. For most surface, the threshold distance for this choice is 5-8 pixels.

There is less at stake in choosing between the HCI and EE methods, because the difference of speed is only a factor of six. The difference in radiosity calculated by HCI and EE beyond 15 pixels is generally less than the uncertainty caused by measurement errors. My experience shows that 15 pixels is good threshold distance, beyond which the EE method may be used, provided that the radiosity must be determined within $\pm 2\%$. This rule of thumb greatly simplifies the calculations attending the choice of method.

ITERATION IN THE RADIOSITY EQUATION

Once the form factors for each surface element are calculated, the data kernel in equation (3) is then also known and can be used to solve the linear radiosity equations. Solving the radiosity equation is one of the most familiar challenges in numerical analysis, because the computing time required increases exponentially with $n*m$, where n and m are the row and column of an image, respectively. Many algorithms have been developed for simultaneously solving the $n*m$ linear equations. The most popular ones are direct methods, such as Gaussian elimination and its variants, but these exhibit a computational complexity related to the cube of the number of equations. Thus, even for a relatively small image (e.g., 100x100 pixels), this approach becomes impractical.

The iterative methods are the best of the candidates for approximate solution. In previous studies of radiosity modeling, Gauss-Seidel iteration is commonly used to solve the set of equations (Cohen and Wallace, 1993): therefore, it is used here also. The Gauss-Seidel iteration is given as

$$B_i(k+1) = SS_i + \sum_{j=1}^i \rho_i F_{i,j} B_j(k+1) + \sum_{j=i+1}^n \rho_i F_{i,j} B_j(k) \quad (10)$$

where $k+1$ is the current iteration and k is the previous iteration. At the $k+1$ st step of the iteration, the new $B(k+1)$ is computed using the values $B_k(j = 1, 1-1, \dots, 2, 1)$ computed in current iteration and the values $B_k(j = i+1 \dots n)$ from previous iteration. For each iteration, the Gauss-Seidel iteration requires $O(n^2)$ operations. At the beginning of the iteration ($k=1$), radiosity B is given by the first reflection or single bounce (SS). The first iteration accounts for the incident SS light reflected onto the surface element from its neighbors. The second iteration accounts for second-order reflections, and so forth.

Gauss-Seidel iteration has clear physical meaning and converges quickly, usually within 2-4 iterations. Each iteration actually represents a reflection between a pair of

surface elements. At each iteration, the Gauss-Seidel method uses the most up-to-date values from the current solution, rather than values from the previous iterations. Since the scattered light usually decreases rapidly in natural environment, because of low reflectivity and moderate relief, only a few iterations are required for the convergence. In general, Gauss-Seidel iteration takes only 2-4 times to achieve 1% maximum difference between the n th and $n + 1$ st iteration. However, if the surface is highly reflective, as is the case for snow or for vegetation in the near-infrared, more iterations will be required and the savings will be less.

PRESENTING RADIOSITY RESULTS

Once the radiosity solution has been computed, the radiosity model comes to its final step — rendering results. The radiosity results basically can be presented in two ways: as rendered images and as analytic results.

RENDERED IMAGES

The calculated radiosity field can be rendered as an image in order to display the 2-D spatial distribution. Although the radiosity calculation is independent of the viewing geometry, the rendered image naturally requires its specification. For a given viewing position, the radiosity field is projected on to a plane that is perpendicular to the viewing direction. If a surface is flat and Lambertian, radiosity does not vary with viewing geometry. For a rough surface or for a non-Lambertian surface, however, the radiosity varies with slope and/or the viewing position.

For Landsat images, the viewing angle is close to zero ($< 11^\circ$) and, since terrain slope is typically small also, the emergent angle rarely exceeds 20° . Every target on the ground is projected on to the horizontal plane (ground). If the surface is Lambertian, the radiosity at each pixel projected onto the viewing plane, is the same as the radiosity

calculated from the DTM (assuming that the DTM has same raster structure as the Landsat image). Thus, for a diffuse surface, the rendered image faithfully displays the radiosity results, without any transformation.

If the viewing angle is off-nadir, however, the radiosity projected in the viewing direction varies with viewing angle, due to the roughness of the surface. For a given viewing geometry, the rendered image can be constructed by a function which maps each pixel (P) to a point (X) in the environment. This projected radiosity value (B_p) can be approximated by the radiosity (B_x) weighted by the corresponding form factor of the point (X) to viewing pixel (P).

$$B_p \approx B_x * F_{x,p} \quad (11)$$

Repeating this process for each pixel produces a discrete map (or image) of the radiosity field rendering for a particular viewing geometry.

ANALYTIC RESULTS

Another way to present the radiosity results is to provide necessary key parameters which are derived from the radiosity model in order to evaluate the multiple scattering. Those quantities are all defined in the glossary at the beginning of the dissertation.

RADIOSITY RELATED TO THE RADIANCE MEASURED BY LANDSAT

Radiosity B describes the total flux density (at each wavelength) leaving a surface in all directions within a hemisphere over the surface, in units of Wcm^{-2} . In contrast, Landsat measures the flux density in a detector that subtends only a minute fraction of that hemisphere, such that the measured parameter is radiance L in units of $Wcm^{-2}sr^{-1}$. For a Lambertian surface, because the radiosity is isotropic in all directions, the radiosity and radiance differ only by a constant factor of π , as expressed by

$$B = \int_{\Omega} L \cos \varphi \, d\omega \quad (12)$$

The quantity $\cos \varphi \, d\omega$ is often referred to as the “projected solid angle” and Ω is the hemisphere. Solving the integral over the hemisphere, the result can be derived as

$$\begin{aligned} B &= L \int \cos \varphi \, d\omega = L \int_0^{2\pi} \int_0^{\pi} \cos \varphi \sin \varphi \, d\varphi \, d\Phi \\ &= -L \int_0^{2\pi} \int_0^{\pi} \cos \varphi \, d\varphi \, d\Phi = -2\pi \left. \frac{\cos^2 \varphi}{2} \right|_0^{\pi/2} L = \pi * L \end{aligned} \quad (13)$$

For a non-Lambertian surface, of course, L varies with ψ and ϕ and hence must be brought into the integral. In this case, L and B are not simply proportional.

The radiance actually measured by Landsat includes upwelling sun light scattered from the atmosphere and downwelling sky light reflected by the surface, as well as the direct reflected sunlight (attenuated by passage twice through the atmosphere). Even this description is incomplete, since it does not take into consideration atmospheric scattering of the reflected term. The approximate equation for radiance ignoring those complexities, should be

$$\begin{aligned} L_i &= \frac{1}{\pi} (B + A_{uw}) \\ \text{or} & \\ L_i &= \frac{1}{\pi} (T_i + \rho_i (I_{rr} + A_{dw}) \cos(\tau_i) + \rho_i \sum_{j=1}^n B_j F_{i,j} + A_{uw}) \end{aligned} \quad (14)$$

where A_{dw} and A_{uw} are the down- and up-welling irradiance, respectively; I_{rr} is the solar irradiance on the ground, after passage through the atmosphere; and T_i is the emittance from the surface. Emittance for most terrestrial targets is significant only at wavelengths greater than 3 μm .

In this radiosity model, the focus was on the multiple scattering among the elements of the rough natural surface, and atmospheric effects have been ignored. Therefore, for VNIR wavelengths the radiosity equation can be simplified as

$$B_i = \pi * L_i = SS_i + MS_i = \rho_i * (I + A_{dw}) * \cos(\tau_i) + \rho_i \sum_{j=1}^n B_j * F_{i,j} \quad (15)$$

which is same as equation (9), including the single-scattering (SS) and multiple-scattering (MS) terms. At some point, however, it will be useful to use the full equation 14, especially for visible wavelengths for which atmospheric effects are important.

CONCLUSION

A new hybrid radiosity model was developed based on three existing algorithms: double-contour integral, half-contour integral, and element-to-element methods. Different from other radiosity models, this new model is made specifically for calculating radiosity of natural surfaces. It provides suitable accuracy of radiosity calculation within acceptable computation time.

The major contribution of this model is to solve the form-factor calculation in a more efficient way. In order to satisfy the desired accuracy of radiosity for natural surfaces, one of three algorithms is selected, pixel by pixel, to minimize running time while maintaining specific performance characteristics. The threshold parameter for the selection is a function of the distance variable, which was precalculated for ~400 cases. The EE algorithm is 64 faster than DCI, and HCI is >60 faster than DCI. The major increase in algorithm speed comes using from HCI as much as possible, instead of DCI.

The current model is still limited by the Lambertian surface assumption. The sensitivity of the model to violations of this assumption is not considered in this study,

but it may be an important factor for the application of the radiosity model to many surfaces.

This chapter describes the development of the hybrid radiosity model. In the next chapter, I will apply this model to study the physical interaction of light with real natural surfaces.

CHAPTER 2: MULTIPLE-SCATTERING PREDCTIONS

INTRODUCTION

The multiple-scattering component may comprise a major fraction of the reflected light from rough natural surfaces. Many studies have shown, either directly or indirectly, that uncorrected multiple scattering may cause inaccurate estimates of surface reflectivity and may therefore introduce error into image analyses (Jackson et al., 1990; Lee and Kaufman, 1986). Image calibration, topographic correction and image classification all may be affected adversely. However, because of its complexity, multiple scattering has not been fully understood nor corrected for image processing of terrestrial images. Solar photons, after their first interaction with the surface, may be reflected many times among neighboring elements of the scene. The multiple-scattering component exists at all scales greater than the wavelength of light, and is controlled by the local surface roughness, solar illumination, diffuse sky irradiance, and surface reflectivity.

Any rough surface will experience multiple scattering, but from the remote-sensing standpoint it is helpful to divide multiple scattering effects into those caused by surface roughness at the topographic scale (great than pixel size) and those caused by intrinsic surface roughness at the subpixel scale (Figure 9), because the former can be predicted from readily available digital terrain models (DTMs), but not the latter. These two levels of MS effects exist simultaneously in all remotely sensed images. At the topographic scale, MS refers to the light scattered from adjacent pixel-sized surface elements, whereas at the subpixel scale it refers to the light scattered among surface elements within the pixel.

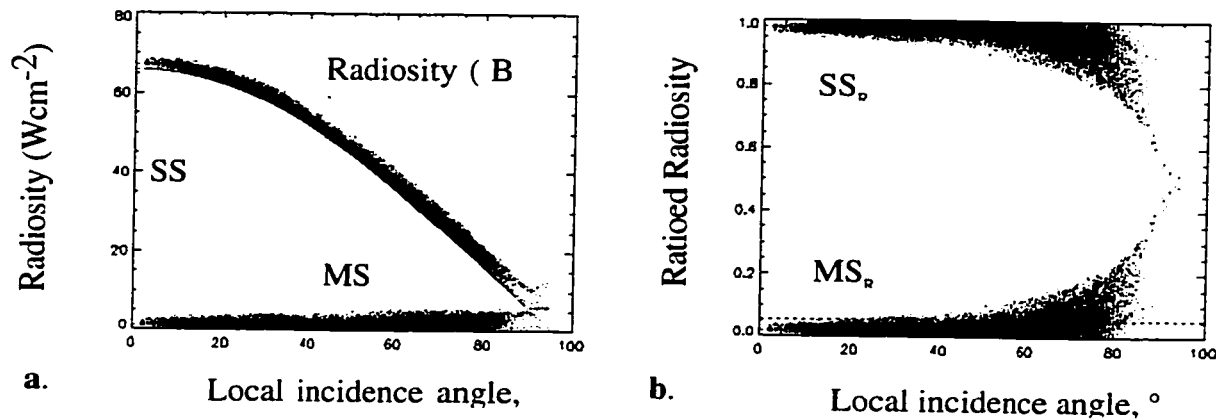


Figure 9. Radiosity decreases with incidence angle, whereas MS increases. These data were calculated at the 30-m (pixel) scale from a DTM for the BC1 area, with $E = 47^\circ$, sun azimuth = 133° , $\rho = 30\%$, $F_A = 10\%$, and solar irradiance = $200 \text{ (Wcm}^{-2}\text{)}$. a. Radiance vs. local incidence angle. b. SS_R and MS_R (relative to R) vs. local incidence angle.

Given an accurate DTM, both the multiple- and single-scattering components of the measured radiance can in theory be estimated quantitatively using radiosity models (Cohen and Greenberg, 1985; Greenberg, 1989; Siegel and Howell, 1992; Cohen and Wallace, 1993). The radiosity-modeling approach has, however, been developed for engineering and computer-graphics applications and not for complex natural scenes for which radiosity calculations have required large amounts of computer time. In remote sensing, radiosity models have been applied to simplified scenes with idealized geometric models such as in, for example, vegetation spectral studies (Borel *et al.*, 1991; Gerstl and Borel, 1992). We have adapted earlier radiosity models to operate on complex scenes for which topographic slopes are calculated from DTMs.

In the modeling of topographic effects, previous studies have mainly used DTMs to calibrate the topographic shadowing and shading effects by using foreshortening of direct illumination (e.g., Teillet *et al.*, 1982; Dozier and Frew, 1990). Few have considered the distribution and magnitude of the higher-order multiple scattering (MS) effects in the

image, and little attention has been given to correcting apparent reflectance for MS effects. Indeed, Proy *et al.* (1989) regarded MS as subordinate to effects of geometry and sky irradiance. Our work, however, shows that this is only true in a general sense, and that for rough surfaces the MS component may locally be second only to direct illumination in importance.

The objective of this chapter is to use the radiosity model to: (1) make quantitative estimates of the amount and spatial distribution of MS for different surfaces; (2) calculate the MS as a function of terrain roughness at the 30-m pixel scale, solar illumination geometry, surface reflectivity, and diffuse sky illumination; (3) calculate MS effects at the subpixel scale and determine the correlation of reflectance, or apparent reflectivity, to surface roughness.

This is a preliminary study on the significance of MS effects for natural surfaces. As such we have ignored some complicating effects such as the changing path length of solar illumination at different solar elevation angles. In future applications, it will be important to consider the whole atmospheric path length.

BACKGROUND AND METHODS

The radiosity model has been developed and discussed in detail in Chapter 1. In my dissertation, all the surface elements are usually assumed to be Lambertian and hence the modeled radiance at the sensor (L , in units of $\text{Wcm}^{-2}\text{sr}^{-1}$) for each pixel is a constant fraction of the radiosity (neglecting atmospheric effects). This fraction is just a constant (π), which can be derived by integrating the radiance (L) over the hemisphere (see Chapter 1 for detail). Thus, the radiance can be written as:

$$L = \frac{B}{\pi} = \frac{(SS + MS)}{\pi} \quad (1)$$

The exitance or radiosity (B) is given by

$$B_i = SS_i + MS_i = I_{rr} * \rho_i * \cos(\tau_i) + \rho_i * \sum_{j=1}^n B_j * F_{E_i, E_j} \quad (2)$$

where I_{rr} is the solar irradiance (Wcm^{-2}), ρ is the reflectivity and τ is the local incidence angle. The MS component of the radiosity or exitance depends on a geometric relationship (the form factor, F_{E_i, E_j}) between neighboring surface elements E_i and E_j .

Two scales of DTM data were used in this study, the first being 30-m resolution USGS elevation data for the Bluff Creek (BC) area, near the town of Orleans in Northern California, and the second being 1-cm topographic data measured for a gravel bar at Bluff Creek and for the dry channel of an intermittent stream in Death Valley (DV), California. The high-resolution (cm scale) DTMs were measured using a 1x1 m pin profiler.

Our goal is to determine approximately how important the contribution of MS can be for natural surfaces depending on viewing geometry. Hence, for simplicity we apply the radiosity model to surfaces assumed to be Lambertian and uniformly reflective, although the model can accommodate heterogeneous surfaces. Laboratory radiance measurements verify that gravel surfaces can be nearly Lambertian but this is less true for vegetation (Vanderbilt and Venecia, 1988; Deering, *et al.*, 1992). However, as in earlier models such as the model of Li and Strahler (1985), we have taken the preliminary approach of assuming Lambertian scattering. Unlike the earlier models, our focus is the estimation of multiple-scattering effects.

RESULTS

For consistency we report results that use the same illumination geometry throughout the study, unless otherwise stated. The viewing angle is 0° (nadir-looking), and the assigned surface reflectivity is 30% (compared to, for example, ~20% for granite

at 0.5-2.5 μm , ~40% for vegetation at 1 μm , and ~80% for snow at 0.5-1.4 μm). The skylight is assigned to be 10% of the solar irradiance, which is fixed at a value appropriate for clear skies at visible wavelengths (200 Wcm^{-2})

To illustrate the importance of MS, we report the results of our modeling using the following parameters: MS, MS_R , MS_A , and $A_{5\%}$ (see glossary).

In evaluating these results it should be noted that the absolute value of multiple scattering in Wcm^{-2} (MS) is somewhat arbitrary since it depends on our chosen value for solar irradiance. MS_R and MS_A provide a measure of the relative importance of MS that is not so dependent on the input parameters we have chosen; MS_R gives the importance of MS compared to total radiosity on a pixel by pixel basis, while MS_A is the importance of MS compared to the maximum possible radiosity in a scene (that for a pixel at zero incidence). Parameter $A_{5\%}$ indicates the area in a scene that might be significantly effected by MS, whether it be MS_R or MS_A .

MULTIPLE-SCATTERING EFFECTS AT THE TOPOGRAPHIC (PIXEL) SCALE.

In this section, we will demonstrate how MS in rugged terrain is affected by the local solar incidence angle (τ), roughness at the topographic scale, the sun elevation angle (E) above the sea-level horizon, reflectivity (ρ) of the surface, and diffuse sky illumination (A_{div}). Two subsets from the Bluff Creek DTM, each 120x120 pixels (3600x3600 m), were selected to represent a rougher and a smoother terrain in this mountainous area. The rougher subset (BC1) contains deep-cutting canyons with a maximum relief of >800 m; the smoother subset (BC2) comprises a broad valley with a maximum relief of <500 m.

Local incidence angle at the pixel scale.

Figure 9 shows scatter plots of radiosity (B), single scattering (SS) and multiple scattering (MS) as a function of local incidence angle (τ), for the rougher subset (BC1). Figure 9a shows the radiant flux density of each component as a function of τ . On this plot the single scattering ($SS = \cos(\tau)$) plots as a line, but the multiple scattering varies with local conditions and causes the exitance or radiosity ($B=MS+SS$) to plot as a scatter of points. MS has generally low values but does increase slightly with τ . Figure 9b shows the relative contributions of SS and MS (ratioed to the local B). About 20% of the pixels in this mountainous area experience a significant component of multiple scattering ($MS_R > 5\%$). Since MS is relatively constant at all values of τ , whereas SS varies as $\cos(\tau)$, the relative contribution, MS_R , tends to increase with τ . Most of those pixels with significant MS_R have $\tau > 40^\circ$. That indicates that MS contributes relatively more in highly shaded and shadowed areas.

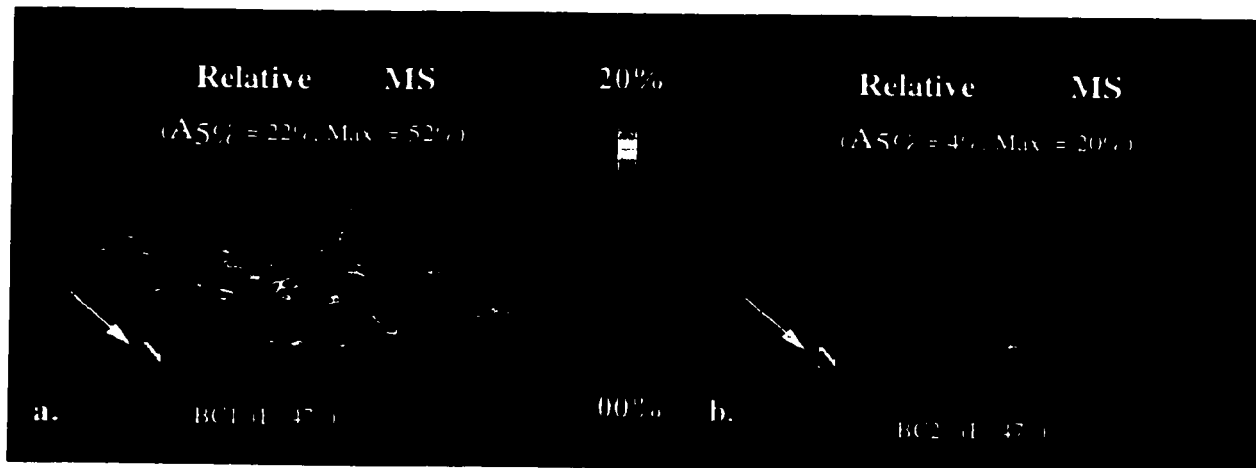


Figure 10. Perspective views of Bluff Creek image subsets show the variation with surface roughness in the distribution of relative MS. a). Subset BC1 (rougher terrain). b). Subset BC2 (smoother broad valley). For both a and b, $E = 47^\circ$ and sun azimuth = 133° , typical for August or May Landsat images.

Topography at the pixel scale.

DTM subsets BC1 and BC2 illustrate the importance of terrain relief on the MS component. Results are shown in Figure 10 for the lighting conditions appropriate for Landsat images acquired in August or May. For the rougher BC1 (Figure 10a) the maximum value of MS_R is twice that for BC2 (Figure 10b). The area of significant MS ($A5\%$ for MS_R) is even more strongly dependent on terrain, being a factor of five or more greater for BC1. Table 1 summarizes the MS effects for BC1 and BC2 under different illumination geometries. In both areas the spatial distributions of MS follow the same patterns, with higher MS values concentrated in localized regions such as cliffs, deep valley floors, and areas facing large reflecting slopes. MS is low in broad valleys and, especially, on ridge tops.

Table 1. Multiple-scattering at the 30-m scale,
Bluff Creek subsets BC1 and BC2

$\rho = 30\%$, sky light = 10%	Bluff Creek Subset BC1			Subset BC2
E	21°	47°	62°	47°
Sun azimuth	155°	133°	121°	133°
$A5\%$ for MS_A	1%	5%	8%	0.5%
$A5\%$ for MS_R	38%	22%	19%	4%
Maximum MS_A	7%	9%	10%	7%
Maximum MS_R	42%	52%	28%	20%

Sun elevation angle at the pixel scale.

For temperate latitudes of $\sim 45^\circ$, the solar elevation angle (E) at noontime ranges from $\sim 22^\circ$ in winter to $\sim 68^\circ$ in summer. Changing the solar illumination geometry affects the shadow and shading, as well as the relative contribution of multiple scattering (MS_R). To illustrate these effects, we have chosen two extremes for DTM subset BC1 (latitude $\sim 42^\circ N$) which relates to available Landsat MSS images: $E=21^\circ$ (19 December) and $E=62^\circ$ (20 June) and a third, intermediate value of 47° . The distributions of multiple scattering

for the two extreme sun elevations are shown in Figures 11a and b. Clearly, both the $A_{5\%}$ and the maximum value for MS_R are much greater when the sun is low on the horizon (Figure 11a) than when it is high in the sky (Figure 11b). The maximum relative contribution, MS_R , is reached for pixels that are in shadow ($SS=0$) and which are illuminated only by multiple scattering and skylight. However, in an absolute sense (in Wcm^{-2}), higher sun elevations cause an increase in both the MS and the single-scattering component (SS), but the multiple scattering forms a smaller fraction of the radiosity, thereby reducing the MS_R term. Therefore, MS_R and $A_{5\%}$ decrease with increasing solar elevation, and MS (in Wcm^{-2}) increases with solar elevation angle, as does the area which experiences a greater than 5% effect for MS_A .

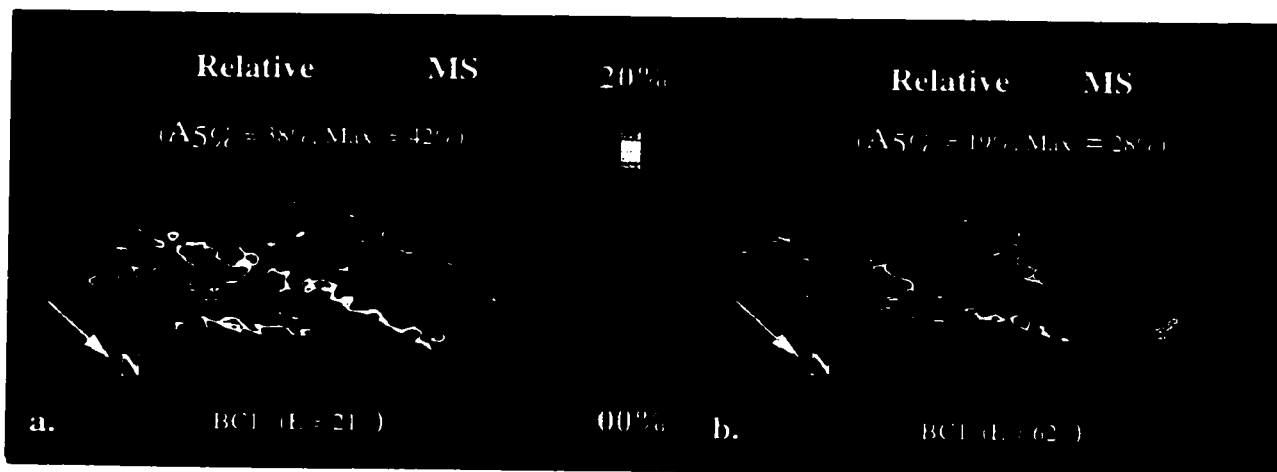


Figure 11. Perspective views of Bluff Creek subsets show the relative MS distribution variation due to the sun elevation angle. a. Subset BC1, with $E = 21^\circ$, sun azimuth = 155° (December Landsat image), b). Subset BC1 with $E = 62^\circ$, azimuth = 121° (June Landsat image). Images are 3.6 km on a side.

In summary, pixels that experience a high degree of shading (because of slope azimuth and angle, or low solar elevation angle) may receive a high proportion (with respect to the total irradiance) of light scattered from surrounding slopes. The relative

contribution of multiple scattering can be very significant for these pixels. This does not necessarily translate into a large absolute measured effect (e.g., in DN) at the satellite sensor.

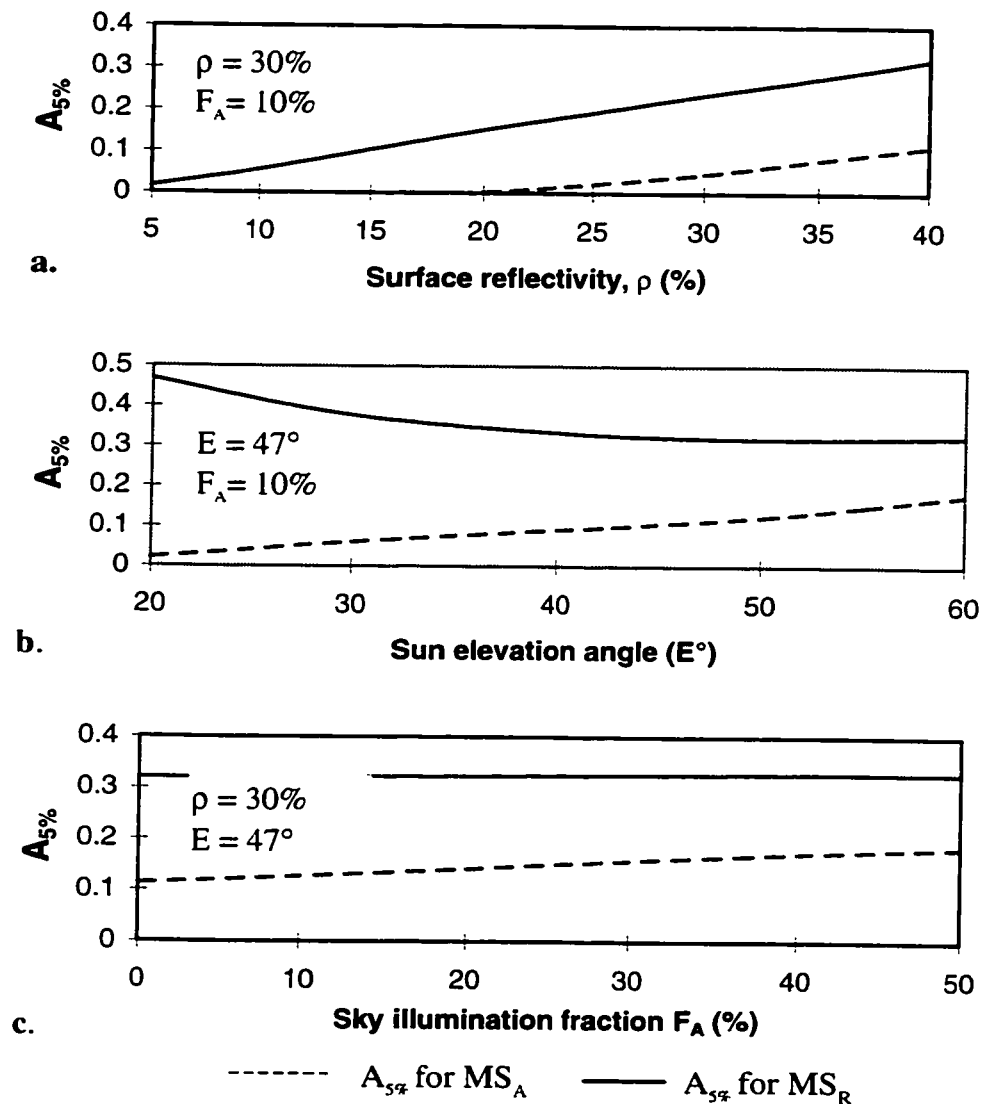


Figure 12. The fraction of the area of BC1 with > 5% of MS_A and MS_R as function of (a) sun elevation angle E , (b) surface reflectivity ρ , and (c) sky illumination fraction F_A . For a, b, and c, sun azimuth is fixed at 133° .

In order to investigate further the physical trend of changes in MS with solar elevation angle, E , we have calculated the radiosity for 10° increments in E ($20^\circ \leq E \leq 60^\circ$) for BC1 (Figure 12a). Figure 12a shows that $A_{5\%}$ of MS_R drops rapidly as the sun rises above the horizon, but changes little for $E > 40^\circ$, whereas $A_{5\%}$ of MS_A increases nearly linearly with E throughout its range. The sensitivity of MS_R to E is thus greater at the lower solar elevation angles than the higher angles, but the absolute value of MS is greater at the higher values of E .

Reflectivity at the pixel scale.

The amount of light scattered from a surface is directly proportional to the reflectivity. In an absolute sense, increased scattering for highly reflective surfaces leads to correspondingly more multiple scattering. The fraction of multiple scattering (MS_R) also increases with reflectivity. This is shown for DTM subset BC1 in Figure 12b, for reflectivities varying from 5% to 40%. The area affected by significant multiple scattering ($A_{5\%}$) increases quasi-linearly with reflectivity—both in a relative sense (MS_R) and in an absolute sense (MS_A). This effect is scale-independent; it influences scenes that are rough at the level of subpixel texture as well at the level of resolved topography.

Skylight at the pixel scale.

We approximate sky illumination as perfectly diffuse and isotropic. Overlooking skylight results in underestimating the irradiance and hence multiple scattering, especially for shady hillslopes. However, the relative proportion of multiply scattered light (MS_R) remains about the same. Levels of sky illumination from 0% to 50% are used to test the influence of skylight on MS (Figure 12c). The $A_{5\%}$ calculated for MS_R is affected little by the amount of sky irradiance (solid curve), but the area of significant absolute multiple scattering ($A_{5\%}$ for MS_A) increases linearly (dashed line). MS_R remains relatively constant because, as skylight is increased, irradiance, SS and MS all increase proportionately.

MULTIPLE-SCATTERING EFFECTS AT THE SUBPIXEL SCALE.

In this section, we first contrast the amount of MS predicted at the subpixel and pixel scales, and then inspect the variation of MS with an rms-height measure of roughness. Then we integrate subpixel effects to the 1-m scale to predict a bi-directional reflectance distribution function (BRDF) for rough surfaces.

Using a pin-profile method, we have measured high-resolution (1-cm) DTMs at Death Valley (DV) and Bluff Creek (BC) that allow us to study the MS effects of the surface roughness at the subpixel scale. The DV site consists of non-sorted, angular rocks and interstitial sand comprising a surface with an rms height of ~ 3.1 cm. The BC gravels are sorted and well rounded, comprising a smoother surface with an rms height of ~ 2.3 cm.

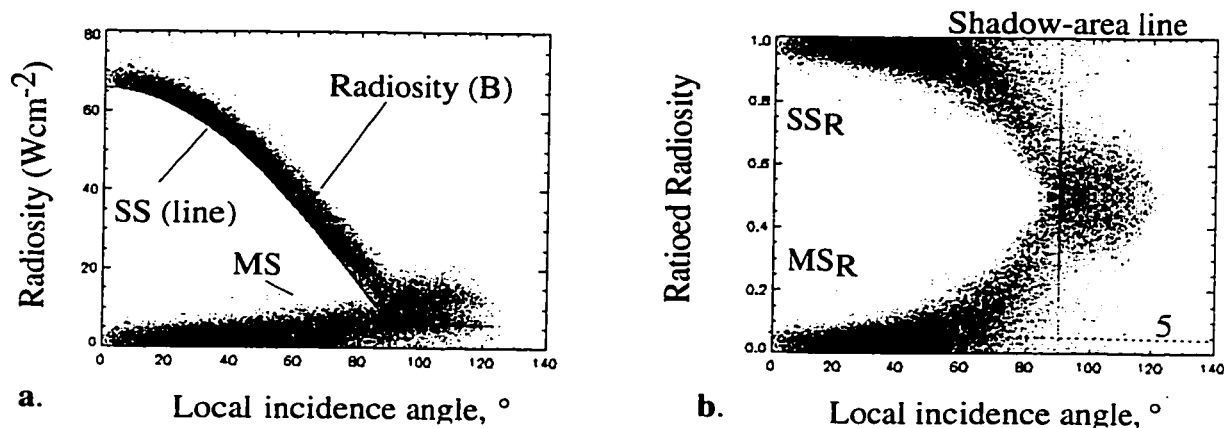


Figure 13. Radiosity results as function of local solar incidence angle for the DV cm-scale DTM ($E = 47^{\circ}$, sun azimuth = 133° , $\rho = 30\%$, and $F_A = 10\%$). (a). Radiosity vs. local incidence angle. (b). SS_R and MS_R vs. local incidence angle.

Subpixel-scale roughness.

The micro-topography measured in the DV and BC areas at the cm scale is relatively rougher than the topography observed at the 30-m scale (BC1 and BC2). This can be documented using the second derivative of the topography, which has a much greater standard deviation at the cm scale (1.5-2.0) than at the 30-m scale (0.2-0.3). The greater local roughness is mainly because clasts have steeper sides than can be maintained for mountain ridges and valleys. Based on the results of the last section, we should predict that these rougher small-scale (cm resolution) landscape features will produce more multiple scattering, although possibly over only a small fraction of the scene. Therefore, $A_{5\%}$ may be difficult to predict from simple statistical summaries of roughness alone.

Table 2. Multiple-scattering at the cm scale,
Death Valley and Bluff Creek scenes

$\rho = 30\%$, sky light = 10%	DV scene	BC scene
E	47°	47°
Sun azimuth	133°	133°
$A_{5\%}$ (MS_A)	30%	26%
$A_{5\%}$ (MS_R)	45%	34%
Maximum MS_A	20%	20%
Maximum MS_R	72%	69%

Table 2 and Figure 13 summarize the MS effects and show the SS_R and MS_R distributions over the local incidence angle for the cm-scale DV pin-profile DTMs. Table 2 shows that although the maximum values of MS_A and MS_R in the DV and BC test areas are similar, the areas affected by MS are much greater for the rougher surface. The $A_{5\%}$ of MS_R in the rougher DV wash is about 45% which is one third greater than that for the smoother BC gravel bar (about 34%). Thus it seems that $A_{5\%}$ is more strongly related to average roughness in a scene than is the maximum MS_A or MS_R . This is because the

maximum value of MS is basically dependent on local geometry, which can be the same for surfaces of different roughness. The $A5\%$ parameter, however, is a statistical measure that depends on the distribution of slopes, and is related to the average roughness of a surface.

Comparison of Figures 13a and 9a shows that (1) both radiosity (B) and the multiple-scattering component (MS) have a greater range of values at subpixel scales, and (2) the MS component rises to much higher values at high local incidence angles. This latter trend is all the more pronounced because steeper slopes are found for boulders and cobbles than can be maintained for hillslopes. Comparison also shows that $A5\%$ for MS_R , likewise, is increased at small scales, from 22% to 45% in this instance. In Figures 13 and 9, $\tau > 90^\circ$ indicates shadowed surface elements facing away from sun, and $\tau = 90^\circ$ includes sun-facing surface elements that are nevertheless shadowed by adjacent topographic feature. In Figure 13b, the vertical array of points at $\tau = 90^\circ$ is due to our arbitrary assignment of that incidence angle to shadowed but sun-facing slopes. The wide range and high values of MS_R for $\tau \geq 90^\circ$ arise because in shadowed areas, the SS radiance is zero and B is dominated by sky irradiation and by MS light from adjacent, sunlit slopes.

The spatial distributions of multiple scattering for the DV and BC test areas are closely related to the spaces between boulders. For both, the peak values of MS_R are concentrated in the spaces between big rocks, and on their north-facing sides. The maximum values of MS_R and MS_A for the two scenes, however, are very close (Table 2), which again indicates that the maximum values are mainly dependent on the local geometry, and are largely independent of average roughness characteristics.

Variation of MS effects over a range of roughnesses

The sensitivity of MS to roughness variation over a greater range of roughnesses may be estimated by comparing Tables 1 and 2, and Figures 13 and 9. All measures

studied show more multiple-scattering effects at the cm scale for gravel surfaces than at the 30-m scale for topography. The presence of depressions and valleys, and the aspect ratio of these features, control the amount of MS in a scene (both area and magnitude). One measure of this aspect of a DTM is the standard deviation (2σ) of the second derivative of the topography ($\Delta\sigma$). In Figure 14 the $A_{5\%}$ (MS_A) appears to increase linearly with $\Delta\sigma$ for a wide range of roughnesses.

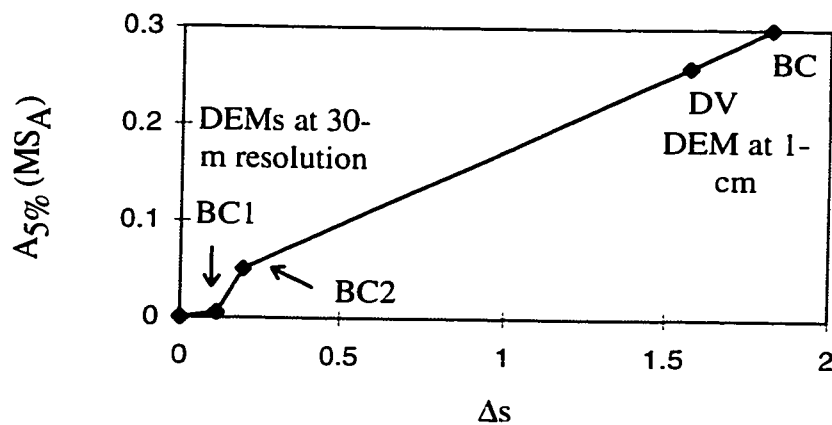


Figure 14. Variation in $A_{5\%} (MS_A)$ with two standard deviation of the second derivative of topography (D_s) evaluated over the images. The BC1 and BC2 represent the terrain rough surfaces at 30-m resolution. The DV and BC are gravel-bar surfaces at 1-cm resolution. The bigger of D_s indicates the rougher (at the subpixel scale) of the surfaces.

Bi-directional reflectance distribution function (BRDF)

In remote sensing, unresolved scene detail is integrated at the pixel scale. Multiple-scattering effects, shadowing, and other radiance features below the scale of measurement are all expressed as a single radiosity or reflectance value. The variation of this value with illumination and viewing geometry (or BRDF) depends mainly on scene reflectivity and roughness. Here we integrate the subpixel radiosities from the pin-profiler sites into single 1-m pixels in order to construct the surface BRDF (Figure 15). Those curves are shown for the DV and BC sites, as well as for an ideal, smooth Lambertian surface. The 1-m pixels are probably quite representative of the BRDF for 30-m pixels since there is

little intermediate-scale topography between the 1-m and 30-m scales. Because the high-resolution DTMs describe surfaces that are flat at scales of 1-30 m, and which contain no clasts larger than cobbles, there are probably few significant roughness differences between 1-m and 30-m pixels.

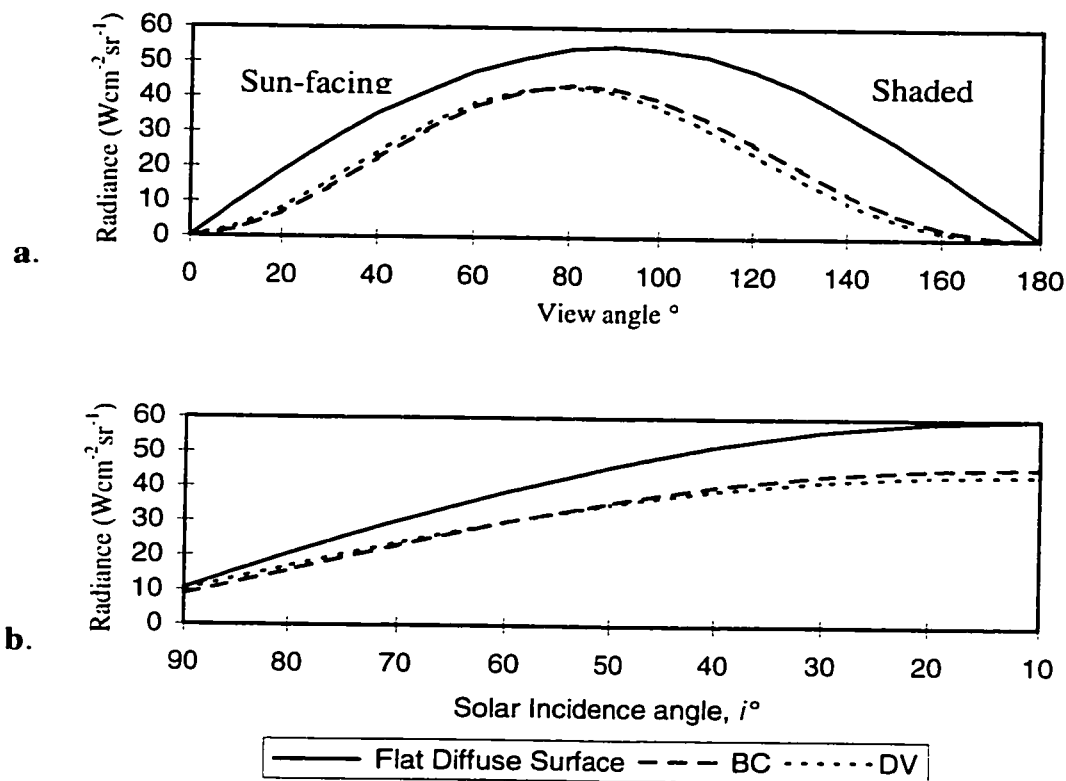


Figure 15. The photometric function calculated using the radiosity model for the Death Valley (DV) gravel surface and the Bluff Creek (BC) cobble surface. The solid curve represents an ideal flat Lambertian surface. a). The radiance as a function of view angle for a fixed solar incidence angle of 47° . Note that radiance is that from a 1-m square. In remotely sensed data the area viewed increases as the view becomes more oblique such that, for a smooth Lambertian surface, the measured radiance is invariant with view angle. b). The radiance as a function of solar incidence angle for a fixed view angle of 90° .

For moderate illumination angles ($E = 47^\circ$), both rough surfaces are darker than the flat surface, mostly due to unresolved shadowing and shading. The relative brightness of

the two rough surfaces, however, changes as the view angle is increased, in this case from $<75^\circ$ to $>75^\circ$ (Figure 15a). This transition point depends on the surface roughness and solar incidence angle and will vary from scene to scene. The sun-facing slopes of the rougher DV surface are the brighter of the two, whereas the shaded slopes of the smoother BC surface are the brighter (by $\sim 5\%$). Therefore, it is clear that the correlation between radiosity and roughness depends on view angle.

For remotely sensed data, the view angle is generally close to 90° or vertical (nadir-looking). In Figure 15b we fix the viewing angle at 90° and calculate the apparent radiances for a range of sun elevation angles ($10^\circ \leq E \leq 90^\circ$). For rough surfaces, the SS term is reduced mainly by the shading of local slopes, whereas the MS term is increased. For BC and DV, single scattering (SS) is reduced to 68% and 64%, respectively, of the value for a smooth surface (sun at zenith), whereas MS is increased by only 9%. Therefore, the overall effect of roughening a surface is to lower the reflectance and to increase MS_R . The smoother natural surface (BC) is the brighter when the sun is high in the sky; the rough surface (DV) is the brighter when it is low on the horizon, by a few percent.

DISCUSSION

In explaining the radiosity model I have assumed that surfaces are composed of smooth Lambertian elements at the 1-cm or 30-m scales of measurement. Clearly, this assumption is violated for some surfaces. For example, light scattered from leaves may have a strong specular component. Incorporating non-Lambertian surfaces in the radiosity model is difficult and computationally expensive, and does not seem to have been done yet. My findings may need modification when this is accomplished. For now, however, even a study based on Lambertian scattering offers useful insights into how remotely sensed images record scene radiance.

The results presented above indicate that multiple-scattering effects comprise, in many cases, an important fraction of the total radiance leaving a pixel, sometimes exceeding the contribution due to sky illumination. The fraction of a scene for which multiple-scattering effects are significant (at the 5% level or higher) may exceed 10-20% in rugged areas, and significant MS effects are almost always present at the subpixel scale. This has implications for many aspects of remote sensing: below, we consider briefly the impact of MS on image calibration, topographic correction and image classification.

Image calibration from DN (digital number) to reflectivity is required before composition may be deduced from remotely sensed spectral data. Unless atmospheric measurements are made during image acquisition, most calibration requires spectral measurements in the field at selected sites. Field spectra are made at smaller scales (e.g., 1-10 cm) than the image measurements, and may be made under different lighting conditions. Therefore, the image data and field reflectance spectra may be differently affected by multiple scattering. For sites for which field reflectance spectra are available it is necessary to know the roughness in order to estimate reflectivities and adjust for the pertinent viewing illumination geometry. The estimate of the reflectance of a surface can then be used with the image data to obtain the appropriate atmospheric correction. In addition, the topographically controlled MS should be accounted for. However, in this respect one could largely avoid the MS effects by choosing sites located on ridge tops or on wide flat plains. This atmospheric calibration would then provide the surface reflectance for the image, but true reflectivity could only be obtained if the roughness was known at all locations in the scene. In the usual case where roughness is highly variable over a scene this would be problematic. Our comparison of two geologic surfaces is encouraging in this respect since the differential effects on MS appeared to be small despite a 60% difference in rms height at the cm scale. However, it is easy to envision situations for which this will not be true. For instance, forest canopies may have much

greater rms heights than gravel surfaces at this and other scales. Correction for these subpixel effects must await further experimentation and characterization of the BRDF for natural surfaces.

Topographic corrections are commonly performed on images in order to remove the effects of different lighting angles on the single-scattering (SS) component of radiosity. This is necessary if images taken at different times are to be compared, or even if image classification is to be attempted, independent of slope and aspect. It would be a straightforward matter to correct for pixel-scale multiple-scattering effects at the same time, using a radiosity model and the DTM. However, to be done correctly it is first necessary to estimate the reflectance. Probably an iterative approach is required. In such an approach, the reflectance is first approximated from the remotely sensed radiances corrected for illumination and viewing geometry with a DTM, and then the approximation is successively refined with the radiosity model.

Complete correction for multiple-scattering effects is necessary if accurate scene classification is to be performed. It is not sufficient merely to classify ratioed reflectances; because MS can distort spectral shape as well as amplitude. Because the amount of this distortion depends on reflectivity, it is an especially severe problem for rough vegetation for which reflectivity may change by a factor of ~20 between 0.6 and 1.2 μm . It should be noted parenthetically that canopy-top MS corrections are necessary but insufficient to reduce remotely sensed vegetation radiances to time-invariant reflectivities, because of the high transparency of leaves in the near-infrared, and volume scattering within the canopy.

I have considered the problem of extracting reflectance from remotely sensed radiances, but equally important is the inversion problem of estimating subpixel roughnesses or textures. In principal, this can be done from visible and near-infrared (VNIR) data, but their strong dependence on reflectivity precludes success in many cases.

Radar images are often used to estimate surface roughness. Radar is insensitive to VNIR albedo, of course, but is sensitive to soil moisture and other dielectric contrasts. Therefore, neither VNIR nor radar alone can be used to extract quantitative surface roughness information unambiguously. I have proposed and am studying a method of joint analysis of VNIR and radar images that can reduce some of the ambiguities and uncertainties inherent in roughness estimation from either data set alone (Weeks *et al.*, 1996; Smith *et al.*, 1996). Further study on the inversion for texture is on-going and will be discussed in later chapters.

SUMMARY AND CONCLUSIONS

In this chapter, I used a new, hybrid radiosity model for studying the spatial distribution of the interaction of electromagnetic radiation with complicated natural surfaces. This model is designed to be of practical use by keeping calculation times within acceptable time limits. I have used the model to determine quantitatively the multiple-scattering component of the exitance (radiosity) from various natural surfaces under various conditions of illumination geometry in order to investigate the importance of this term in remote-sensing imagery.

Multiple scattering occurs on most natural surfaces at all spatial scales and viewing and lighting geometries. I find that the amount of MS in the scene is not only controlled by roughness of the surface, but also by sky illumination, surface reflectivity, sun elevation and viewing direction. Under commonly encountered lighting conditions results demonstrate that multiple scattering is a more significant process than has previously been suggested. The amount of MS can vary with scale, because small-scale features such as boulders can maintain greater slopes than can large-scale landscape elements. At the subpixel scale, the integrated effect of multiple scattering can account for as much as 10% of the measured radiance. In addition to contributing a significant proportion of the radiosity (exitance), the roughness of surfaces has a significant effect on

the net BDRF; surfaces that are Lambertian when smooth become non-Lambertian when rough. At the topographic scale, in Landsat images of mountainous regions for example, the fraction of a scene with significant MS effects ($>5\%$) may exceed 10-20%. It is important to recognize and correct for these effects in quantitative image analysis.

CHAPTER 3: VALIDATION OF RADIOSITY MODEL

INTRODUCTION

In Chapter 1, I developed a hybrid radiosity model to predict the radiosity or exitance (B), including the single-scattering (SS) and the multiple-scattering (MS) components, leaving a surface for any given illumination and viewing geometry. In this model, typical digital terrain models (DTMs) are used to describe the scene structure for computing the radiosity. The predicted radiance can be tested against the radiance recorded, for example, on Landsat images. The radiosity results given in Chapter 2 have visually reasonable distributions or patterns of radiance over a rough terrain at two scales. However, for evaluating applications of the radiosity model in actual remote-sensing projects, quantitative evaluation of the accuracy of the predicted radiosities is necessary.

From inspection of model results, it appears that there are several parameters that control the distribution of radiosity and MS component in a scene. The most important of these are surface roughness, surface reflectivity, and the sun-surface-viewing geometry. Validating the radiosity model thus entails: 1) verification that this list is complete, 2) demonstration that the model sensitivity to each parameter is within predetermined limits, and 3) demonstration that the radiosity predicted for a range of simple natural surfaces is accurate within selected limits.

Model validation serves to connect theoretical model and its applications. It establishes accuracy range for radiosity prediction and indicates potential problem areas in application where terrain light conditions, or any characteristics adversely affect the results.

This hybrid radiosity model was developed under several restrictive assumptions: the surface is a Lambertian scatterer; the reflectivity is known and uniform; the viewing and illumination conditions are accurate; the atmosphere is well characterized; the DTM is accurate; and the scene is band-limited such that no roughness elements are unresolved by the DTM. Violation of any assumption will affect the accuracy of radiosity and MS values. In order to validate the model accuracy, it is necessary to restrict scenes and measurement conditions to those that fit the model assumptions well. For testing the wider range of model predictions, experiments are extended from simple geometrical surfaces to computer-milled surfaces specified by a DTM.

In the study of radiosity, most researchers have concentrated on developing the basic algorithms for solving the form-factor and radiosity equations efficiently, and consequently on the trade-off between rapid computation and accuracy (Cohen and Greenberg, 1985; Baum et al., 1989; Troutman and Max, 1993; Zatz, 1993). Validating these models has been largely subjectively, relying on the visual assessment of the pattern of results (Cohen and Wallace, 1993; Ashdown, 1994). Some applications of radiosity models in remote sensing, however, have compared the model results with actual measurements and these comparisons found that the radiosity model predicts much closer results to actual measurements than those from other models (Greenberg, 1989; Borel et al., 1991). Using laboratory measurements on test surfaces to verify predicted radiosities has not been fully exploited because, in part, the experimental setup is difficult for realistic scene environments and surface materials.

In order to fill the gap of model verification, I have simplified many requirements for calculating the radiosity. I have chosen some extreme materials and test surfaces to diminish the inevitable errors in the laboratory verification. High reflective, diffuse materials (like Matt board and white plaster) were used for building test surface, in order to increase the signal/noise ratio. Simple geometrical surfaces were made with these materials to aid in the comparison of predicted and measured radiosities. The focus is on

how closely these values agree, and why they do not. Through the preliminary validation of the radiosity model, I attempt to built confidence in application of the hybrid radiosity model to natural surfaces at pixel and subpixel scales.

EXPERIMENTAL SETUPS AND LABORATORY MEASUREMENTS

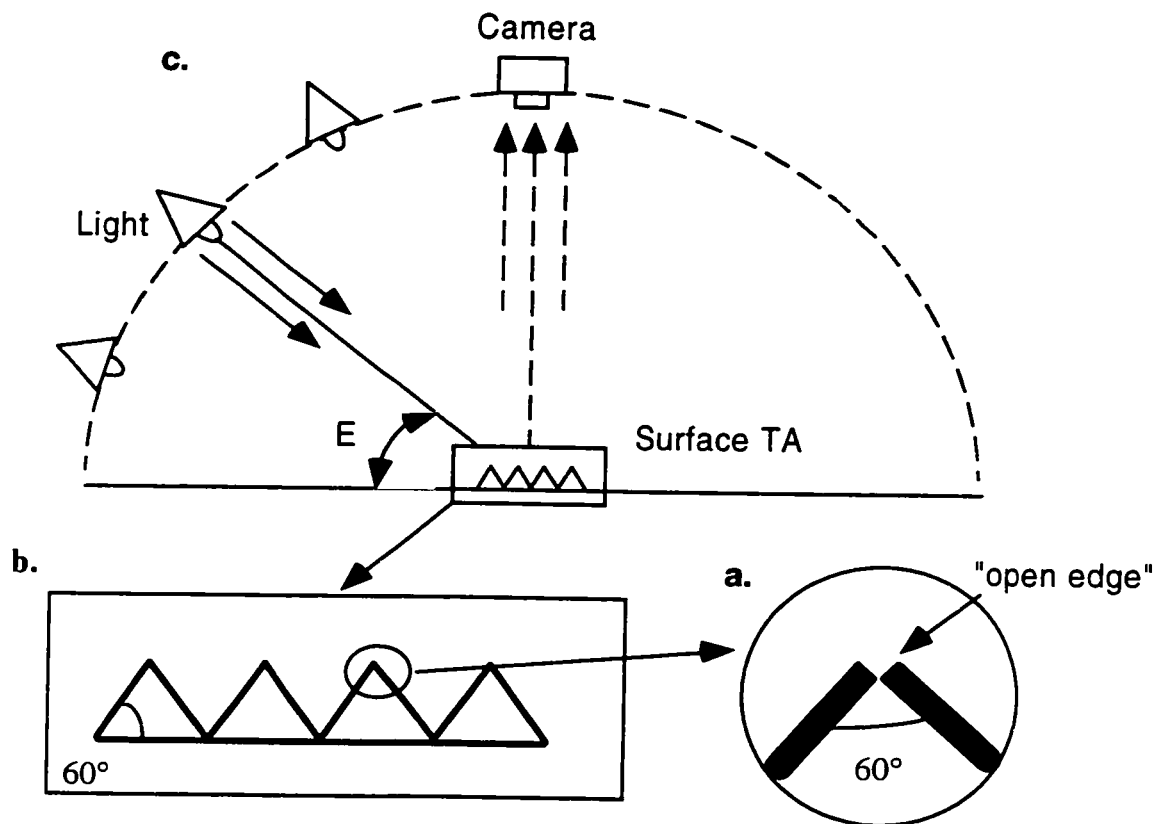


Figure 16. The experimental set-up for the laboratory measurements of CCD images, and relevant geometric parameters. Some associated errors with these parameters are: a. 'open edge', b. 'slope variation,' and c. 'E-angle variation,'

The validation of the radiosity model has been done by matching the predicted model results and measured radiance for two types of surfaces. Radiance measurements

were made in the laboratory using a CCD camera system and controlled illumination. Figure 16 shows the experimental set-up for the radiance measurements. The whole process involves four steps: making the test surfaces, illuminating the surfaces, making the CCD measurements, and registering the CCD images to the digital terrain models.

MAKING THE SURFACES

Two test surfaces were used: a simple geometric surface with accurate DTMs and a more complete and realistic surface of natural terrain. The former was made of equilateral triangular prisms; and the latter was milled from a 7.5' DTM.

The first surface is a one-dimensional triangular function extended in the other direction, called the 'TA' surface. It was designed for maximum geometric control. The surface material is white Matt board, which is nearly Lambertian. The Matt board was scored and bent alternatively $+60^\circ$ and -60° every 5 cm, and the whole was fixed on to a flat board for stability. The whole surface is 20x20 cm and consists of three triangular valleys separated by ridges. Its corresponding DTM is computer-generated using the Excel program. This DTM is accurate except near the edges of the Matt board surface model. Fiducial markers were made using black dots on the edges of the prisms (tops and bottoms) every 5 cm: these helped in the registration of the images and DTMs.

The second surface was fabricated by a computer-controlled milling machine operated by Drs. X. Kuga and S. Chen in the Department of Electrical Engineering at the University of Washington. A subset of the Bluff Creek DTM, called 'BC,' was used to drive the computer. The original milled surface is a mold, from which positive subset plaster surfaces can be made. The BC DTM subset used to make the mold was 400x400 pixels with 30-meter resolution (12x12 km) over a mountainous region. Since the milling head was not designed to accommodate sharp changes of slope, sharp edges present in the

DTM data are smoothed, especially ravine bottoms and ridges. Thus, the physical model and the DTM are not perfectly matched in those particular areas.

All the surfaces are highly reflective to give the maximum contrast of signal to noise. The reflectivity of Matt board was measured to be ~ 95% and white plaster was measured to be ~ 87%, over much of the visible spectrum.

ILLUMINATING THE SURFACES

I used a specially designed Dedo light as the illuminant. This light has a long focusing range which allows the hot spot to be strongly defocused. The field of view can be controlled by a projection attachment: it ranges from 5- to 100-cm diameter at 200-cm distance. Using the Dedo light, the biggest variation in light intensity over a 20x20 cm surface is less than 5%. However, a major drawback of this Dedo light is that the light intensity is decreased, especially for oblique illumination (such as low E). The Dedo light was mounted on a tripod. The illumination direction was controlled manually and measured with clinometer with an accuracy of $\pm 1^\circ$.

CCD CAMERA SYSTEM AND RADIOSITY MEASUREMENT

The radiance was measured by a CCD camera system, which was designed by Dr. Milton Smith at University of Washington. The CCD itself was manufactured by Philco Ford, Inc. It has eight channels in the visible and near infrared centered at 480, 550, 680, 724, 852, 898, 950, and 974 nm respectively, with ~100 nm bandwidths. The total image size is 596x488 pixels. Only band 2 (550 nm) is needed in this study for validating the radiosity model, which is not spectrally sensitive (for reflected radiation). The camera was fixed in the nadir-looking position, looking straight down to the test surfaces, analogous to the Landsat viewing geometry.

Radiances from the test surfaces were measured in a dark room with no source light other than the controlled direct illumination. The test surfaces were laid on a flat surface surrounded by black cloth to eliminate the bounce light from nearby counter tops and walls. Series of CCD images were taken with illumination angles stepped from 80° to 20° elevation angles, at 10° increments. A flat reference surface, composed of the same material as the structured test surface, was also measured under the same illumination conditions and with the same camera integration time for use in image calibration. The images were all saved in short integer format (2 bytes) and processed under IDL operators on a Unix platform (DEC Alpha 3000 with a 276-Mhz processor).

REGISTRATION AND SCALING

In order to compare the CCD and predicted images, it is necessary first to register them. I used the "PICREG" program developed at JPL's Image Processing Laboratory (IPL) by Jean Lorre, and adapted and improved at UW by Steve Cothorn. It uses a geometric rectification algorithm to stretch one of image to another based on a group of selected tie points. These tie points are crucial for the accuracy of the registration. The DTM image was used as the reference to which the CCD image was registered. The accuracy of registration affects the reliability of the comparison of the predicted and measured images.

For the surface TA (the triangular prisms), the tie points were selected by matching the black marks on the CCD image (corresponding to marks on the test surface TA), to the corresponding points on the DTM image. Those tie points on the ridges were matched precisely, but tie points on the valley bottoms were less accurate, because bounce light from valley walls masked the black marks in the CCD image. The maximum registration error was less than 1 pixel, even in the valley bottoms.

Registration for the milled surface BC is less certain than for TA, because of the inaccuracy of the milled surface introduced in the fabrication process. For best

registration, the DTM image was illuminated with the same geometry as the CCD image. Since the milled surface does not have registration markers like the TA surface, its terrain features, such as river valleys, hills, and sharp cliffs, must be chosen as the tie points. However, the fabrication process has smoothed those sharp terrain features in the physical model. Furthermore, because this smoothing is most pronounced on exactly these same landscape features that were used for tie points, choosing good tie points is difficult and maximum registration errors range up to 2 pixels locally.

The CCD measures the photons radiated from each surface element. The flux recorded increases with camera integration (dwell) time. The full dynamic gray-scale range for the CCD is 0-30,000 counts or DN. By changing the dwell time, the image can be scaled to fit in this dynamic range: optimally, the scene fluxes should be scaled to fall in the range 2000-25000. Because the geometry of the experimental setup (light-surface-camera) changes from one measurement to another, and because the dwell times are adjusted correspondingly, image gray levels are scaled differently from image to image. These scaling factors must be normalized to facilitated inter-image comparisons.

To calibrate the images, I put small black and white cardboard reference targets with known reflectivity in the scene before image acquisition. A simple linear equation (light transfer function) relates the image DN to scene reflectivities ($\rho = a + b * DN$). Since two (ρ , DN) pairs are known (for the cardboard targets: black and white), it is possible to calculate the linear coefficients: a and b , and thus the conversion of the all DN to ρ is possible. However, there was some variability DN across the cardboard targets due to the non-uniform illumination and bounce light from the surroundings, which can be especially important for high incident angles (low elevation angle). Thus, the a and b may contain some errors (<5%).

ERRORS IN LABORATORY MEASUREMENTS

Before comparing the predicted and measured radiosity images, it is necessary to discuss some systematic errors from the measured data in order to understand the comparison better. These errors generally refer to the geometry of surface models, illumination geometry and radiosity model approximations.

GEOMETRIC ERRORS OF TEST SURFACES

The geometric errors arise because the test surfaces do not match their corresponding DTM images perfectly, caused both by construction and registration errors. Their magnitudes directly relate to the method of construction of the test surface were made. The DTM of test surface TA was mathematically generated on computer, so it had perfect shape: sharp edges, uniform slope and correct slope lengths. However, the real test surface made from 2-mm-thick Matt white board was less ideal. When the board is bent, the ridges will be expended and opened, rather than forming the sharp edges of the DTM; the valley bottoms will be compressed, and the nearby slopes may be slightly deformed (Figure 16a). These edges are locally curved, creating local multiple-scattering environments that are not represented on the DTM. Therefore, the CCD images show bright stripes along edges not predicted by the radiosity model. The nine edges of the physical model account for about 10% of the total area of the test surface. The second major geometric error is in the slopes of the prism faces: each face may vary from the specified 60° by $\pm 2^\circ$ (Figure 16b). Part of the reason is because the bottoms were supposedly fixed on equally spacing markers on the flat base board, but inevitably the point of contact was somewhat off. Because single scattering is purely a function of the cosine of the local incidence angle, a slope error of 2° will cause a 3.6% error in SS. Therefore, the measured radiance values were probably in error by $< 4\%$ due to disagreement between the physical model surface and its DTM.

The mis-match between the milled surface BC and its DTM is caused only by the fabrication process. The computer controlled milling machine has very accurate geometric positioning, and the overall shape of the terrain is faithfully reproduced. However, the drilling head, with a diameter of 2-3 pixels, smoothes the high-frequency features of the terrain. In addition, due to mechanical failure, the milled surface BC has 2x10 mm mis-match localized in a strip in its center. This defect was filled with plaster manually, but the detailed topography is poorly reproduced.

The geometric errors and their effects on radiance can be inferred from comparison of predicted and measured radiance images, especially if the errors were localized. Overall, their effects compound with errors in illumination and registration.

ILLUMINATION ERROR

The illumination of the physical surfaces results in two kinds of errors: those due to illumination geometry and those due to non-uniform intensity. The former source is manifest both as local registration errors (due to shadowing) and general radiometric errors (Figure 16c). The local mis-registrations are worse at low sun elevation angles, but rarely exceed ± 1 pixels, at least for the illumination geometries used in this study. The global radiometric errors are due to the difference between the assumed and actual incidence angles. This difference does not vary with terrain, but the radiometric effect does, because the irradiance for each element is only proportional to its $\cos(\tau)$. The latter source of error, illumination "hot spots," introduces low-frequency error on the order of $<5\%$ for oblique lighting. The illumination inhomogeneities are less severe for higher elevation angles. This error does not affect the visual appearance of the images, which is dominated by high-frequency features, but it does affect the statistical comparison.

Lighting intensity can vary across the test surface by as much as 50% for regular incandescent sources. For the defocused Dedo-light, this variability is reduced to ~5% , yet it remains the single largest source of radiometric inaccuracy, and the light must be normalized if the model comparison are to be meaningful. In order to do this, the radiance was measured for a white reference board of known reflectivity in place of the test surface, using with same integration time and illumination geometry. This image is a record of illumination variability. The problem is that, because the actual surface is not flat, the light intercepted each surface element is different than the light for the equivalent element of the flat, especially at oblique illumination angles (Figure 16). The error due to lighting heterogeneity varies with the illumination angle and with the local relief of the surface. For most cases, the radiometric error should be less than 2-3% of the average value.

The reference CCD measurements were scaled by normalization accordingly with corresponding test surfaces, and used directly as irradiance inputs in the radiosity model , replacing the assumed constant illumination. Since the overall radiometric errors were quite small (<2-3%), correction was not attempted.

Inaccurate center-pointing of the light source also contributes to radiometric errors. Seated on a tripod, the position of the light was controlled manually with bubble levels in three directions, and the elevation angle and azimuth angles may include inaccuracies of 1-2° %. The centers of illuminated field and the test surface, aligned by eye, introduced error of another ± 1 %. In the worst case, the elevation angle can affect the single-scattered radiance at the level of $\leq 5\%$ of the radiosity. Centering and orientation errors and residual heterogeneity lighting will not be significant for isotropic surfaces, but could be important for anisotropic scenes. Overall, the maximum inaccuracy caused by the illumination errors is less than 4% of the local radiosity value.

STRAY LIGHT

The experiment was not conducted in a perfectly dark room, Some stray light came from the sides of Dedo light housing and from windows, and some of this was reflected from surrounding walls. For high elevation angles and a close light source, stray light was negligible, but it was 5-10% of total irradiance when the direct lighting was oblique or distant and, therefore, of lower intensity. The effect of stray light in the CCD measurements is not clear. Intuitively, it may increase the total irradiance and therefore, the multiple scattering in the scene, but the ratio of the MS and irradiance may be decrease. The flat reference surface was not used for correcting the radiometric effect of the stray light.

RADIOSITY APPROXIMATION

Another type of error is from the radiosity model itself. Radiosity model errors arise from the approximations in calculating the form-factors, early termination of the iterative calculation, and inaccuracies in the input reflectivity value. Although the magnitude of the errors lies within the limits discussed in Chapter 1, the actual errors are unknown because they are due to local unknown geometric or reflectivity uncertainties. These random model errors are difficult to separate from the systematic errors.

Most of the errors discussed above are compounded as total errors, and are present in the image either systematically or randomly. However, low-frequency geometric distortions are manifested as local but non-random errors.

COMPARING THE PREDICTED, MEASURED AND RADIOSITY IMAGES

Comparisons of the predicted and measured radiance are presented in two ways: subjective evaluation of the images (photo-interpretation) and quantitative analysis of differences. The former method involves comparing not only the radiosity (B) images

themselves, but also the histograms and inspections of the predicted SS and MS images. The latter method, however, presents a good quantitative comparison of the spatial distributions of radiance mismatches and the distributions of the local ratio of MS/B. Below, comparisons of each type are reported separately, followed by a discussion of the possible causes of the disagreements between the predicted and measured radiance.

The radiosity results are sensitive to illumination geometric errors, especially for low illumination (or sun) elevation angles, because the effect of geometric errors of the test surfaces are exaggerated there. With high illumination angles, the errors with respect to the local radiosities are smaller than with low illumination angle. In order to minimize this error, the illumination at 70° elevation angle is used as an example for the comparisons of the predicted and measured radiosity.

For comparing radiosity (B) in units of Wcm^{-2} and measured radiance (L) in units of $\text{Wcm}^{-2}\text{sr}^{-1}$, one of them must be scaled to have the same units as the other. As I discussed in Chapter 1, the radiosity is only different from the radiance by a factor of π for diffuse surfaces. For convenience, the use of the term “scaled radiosity (B/π) or predicted radiance” below refers to the radiosity scaled by π , unless stated otherwise explicitly.

IMAGE MATCHING

Histogram match and scattering plot

The first step in validating the radiosity-model results is to match the histograms of the calculated scaled radiosity (B/π) and the measured radiance (L). The histograms of the scaled single-scattering (SS/π), scaled radiosity, and CCD images display the general population distributions of these parameters (Figure 17). The matching of the histograms would indicate the similarity of their radiance distributions.

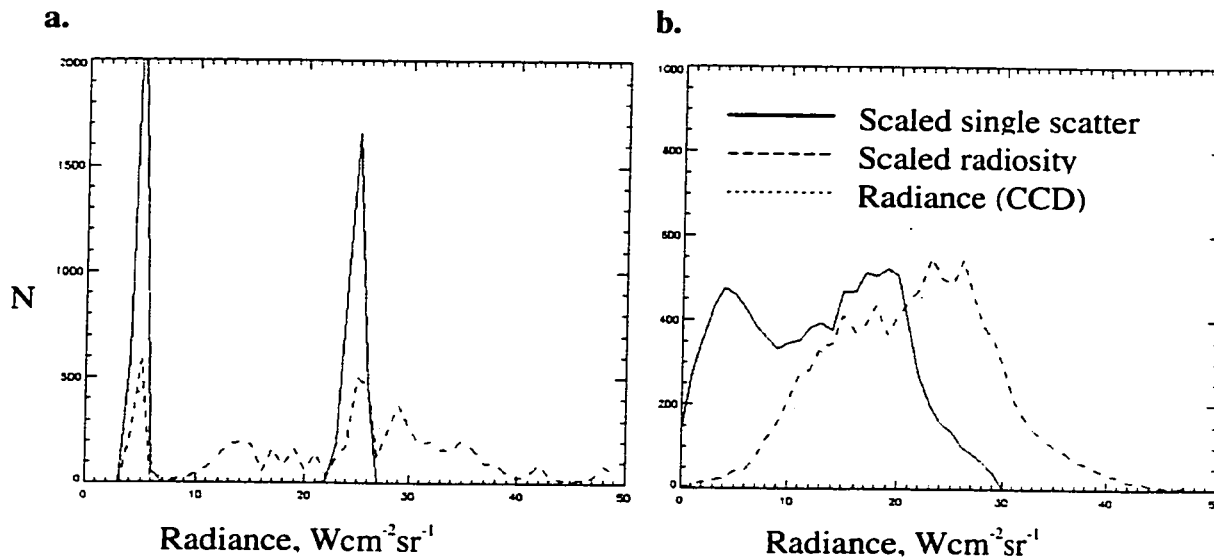


Figure 17. Histograms of predicted radiance (scaled radiosity), predicted single-scatter radiance, and measured radiance (CCD) for the surface. a) TA and b). BC. 'N' is the number of pixels. Radiosity and single-scattering component have been scaled by π .

For a given surface under direct, uniform illumination, single scattering varies only with local incidence angle. The scaled SS histogram reflects the population distribution of the sunlit and the shaded areas in the image. However, if the direct illumination is not constant from pixel to pixel (it varies with $\cos(\tau)$ and non-uniformity of light), the scaled SS will be affected directly. The intensity of the Dedo light, used to illuminate test surfaces TA and BC, varies by 5% across the image and is brighter near the center than near the edges. This variability introduces uncertainties into the measured SS, which should be reflected in the histograms.

The radiosity is the sum of the MS and the SS, so it has a higher value than SS at each pixel. In its histogram, the scaled radiosity distribution is generally spread towards higher values than the scaled SS, but has formed smaller peaks of population than scaled SS due to uneven amount of MS among pixels.

The measured radiance records all the energy leaving the surface, including both the MS and SS terms. Its histogram should be similar to scaled radiosity curve. Details of the histograms for surfaces TA and BC are further discussed below (Figure 17).

Surface TA

The histogram of the scaled SS component (solid line) for surface TA was bimodal (Figure 17a): one peak for sun-facing slopes and the other for shadowed slopes. The peaks were sharp with little spreading: less than $8 \text{ Wcm}^{-2}\text{sr}^{-1}$ out of a maximum of 160. Because of the simplicity of TA, even this dispersion is unexpected and is probably caused by the non-uniformity of the Dedo light source. The histogram for the scaled radiosity for TA (dashed line, Figure 17a) is also bimodal, but each mode is asymmetric, due to the addition of the multiple-scattering component. The residual distinct peaks spreading out towards higher radiance values indicate that some areas received little or no MS illumination. These areas are mostly around the tops of hills. The CCD radiance data for TA (dotted line), stretched to the same scale as discussed earlier, are also plotted in Figure 17a. It is clear that the CCD data more closely match the scaled radiosity than the scaled SS. Although the two histograms are not matched exactly, probably due to artifacts in the physical model, the overall shape and range of gray values correspond well between the CCD radiance and the radiosity histograms.

Surface BC

The surface BC has typical, complicated landscape features and comprises hill slopes up to 40° . The distribution of the scaled SS data, shown in Figure 17b (solid line), has less strongly bi-modal shape than for the TA surface (Figure 17a), because of the wider range of slopes and orientations. The scaled radiosity histogram (dashed line) has been shifted upwards, forming a weakly skewed, normal distribution. The CCD radiance curve (dotted line) is similar to scaled radiosity curve, except the “tail” in CCD data is shorter than in the radiosity distribution, and a small gap is formed in the range of 70-100

units. Both discrepancies are probably caused by inaccuracies in the milled surface BC. The former is related to the smoothed valley floors in the milled surface, leading to anomalously lower radiosities there; the latter is related to both DTM and registration errors, which may produce locally inaccurate SS and MS predictions.

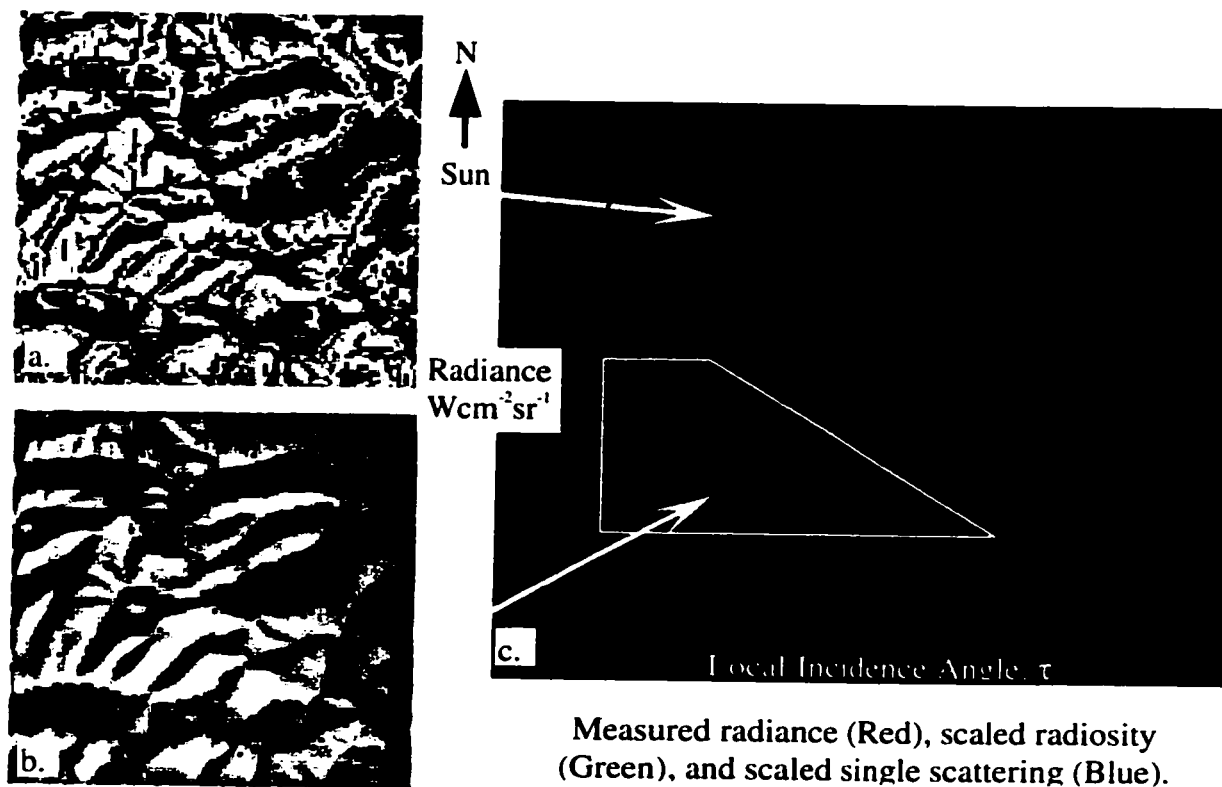


Figure 18. Distributions of mismatch areas between predicted and measured radiance are shown in the Bluff Creek (BC) DEM image (a and b) relative to their scatter plot (c) of predicted radiance (scaled radiosity), predicted single scattering radiance, and CCD measured radiance. a). The distribution of scaled radiosity values that are not matched by the measured radiance. b). The distribution of measured radiance data that were not predicted by the scaled radiosity. c). The scatter plot of the measured radiance data and scaled radiosity and single scattering results vs. the local incidence angle. Note that the mismatch data in both a and b have a similar pattern.

Figure 18c shows the scatter plots of the scaled radiosity, scaled single scattering, and the measured CCD radiance versus local incidence angle (τ) and Figure 18a and b show the corresponding spatial distributions of their radiance mismatches in colors. The scaled SS data, plotted in blue, follows a cosine curve; the scaled radiosity data, in green, are scattered above this curve; the cluster of CCD radiance measurements, in red, overlies the scaled radiosity cluster, except for some radiance mismatched areas at lower incidence angles (green dots only). In mismatch regions, the CCD data tend to be lower than the scaled radiosity values. The corresponding geographic locations are displayed in green in Figure 18a; where they are preferentially along the valleys. The spatial clustering suggests that the radiance mismatch is due to the inaccurate smoothed milled surface, the errors of which were most pronounced in valley due to maximized geometric errors. In contrast, in almost same region of the τ in Figure 18c, CCD values fall below the scaled SS curve (red cross only). Their locations are shown in red in Figure 18b, distributing almost same areas as high radiosities were displayed in Figure 18a. This geographic coincidence of the anomalous data further points to systematic errors (local slope distortion) near the valley floors in BC. As discussed above, smoothing in the milling process has reduced the steep valley slopes there, leading to lower CCD radiances by increasing the local incidence angle. Similarly, the multiple-scattering component is decreased locally, because the roughness of the surface BC is reduced.

Overall, the histograms and scattering plots for both surface TA and BC have shown the predicted and the measured radiances in close agreement. This similarity is evidence of the validity of the radiosity model.

Visual comparison of predicted and measured radiance

Comparison of images instead of 1-D histograms permits more detailed comparison of predicted and measured radiances at each local incidence angle. However, radiosity and MS images both strongly rely on the local geometry. Their spatial variations

therefore closely relate to local location: radiosity is strongly influenced by SS on the sunlit slopes, but dominated by MS on the shaded slopes. Ideally, the CCD image should have same radiance pattern as the radiosity image. Below, the measured CCD image is compared to predicted scaled radiosity images.

Surface TA

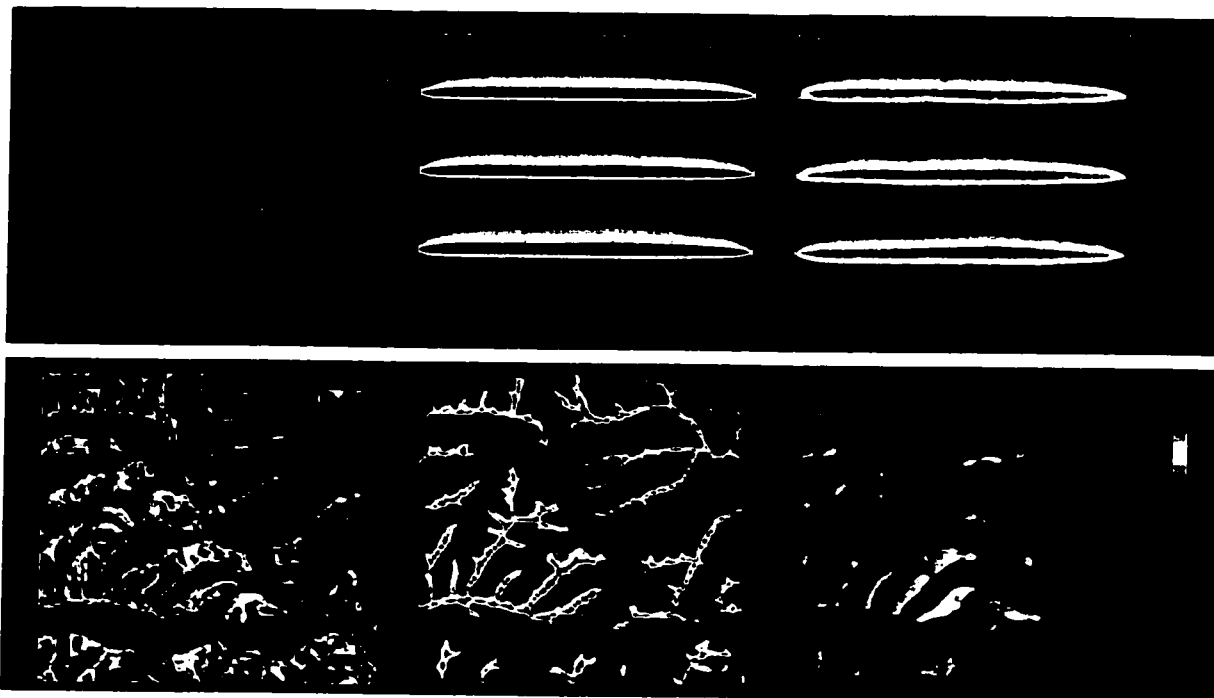


Figure 19. Scaled single-scattering component (a,d), scaled radiosity (b,e), and measured radiance (CCD) (c, f) images for test surfaces TA (a-c) and BC (c-f).

The prismatic surface TA has only two local incidence angles; its scaled SS image consists of only two color stripes (Figure 19a), corresponding to its histogram as the two peaks in Figure 17a. For a given illumination angle, the brightnesses on the two sides of the ridges are constant, except for a little variation due inhomogeneities of the source light. This percentage of bright and dark area in the image would change with the illumination elevation angle. The scaled radiosity image, however, has an additional complexity: three bright elongate enclosures along the three valley floors (Figure 19b).

They are all asymmetric, brighter on the light-facing slopes and darker on shaded slopes, following the cosine law of irradiance. In comparison, the similar pattern in the CCD image (Figure 19c) seem more “noisy” than in the scaled radiosity image. Overall, however, the brightness patterns match well, with only minor discrepancies. First, the boundaries of the enclosures in the CCD images are irregular, which could be due to mis-registration and departures from ideal Lambertian behavior of the physical surface. Second, the three enclosures are shifted a little to the top (shaded side), probably because the illumination angle for the CCD image was higher than specified in the radiosity calculation by a degree or two. Third, boundaries along the ridge tops show radiance mismatching due to inaccuracies in the DTM. These three discrepancies are minor compared with overall agreement of the major patterns.

Surface BC

Surface BC has more complicated landscape features than TA. Its scaled SS image (Figure 19d) displays the basic structure of the mountainous terrain, brighter on the sunlit slopes and darker on shaded slopes of the prismatic ridges. The scaled radiosity and CCD images (Figure 19e and f) both show increasing brightness in valleys relative to the scaled SS images. Most highly shaded areas in the scaled SS image (in valleys), shown in Figure 19d with low values in purple color, have been brightened in the scaled radiosity image by the addition of the MS component. Therefore, both the scaled radiosity and CCD images have less purple area than the scaled SS image. The CCD image resembles more closely the scaled radiosity than the scaled SS image, although the similarity is less than it was for surface TA. This is probably because there are more systematic errors in the DTM of BC than TA. In detail, those errors are revealed as radiance mismatching areas in the valley floors (Figure 18), areas that are brighter in the scaled radiosity image than in the CCD image. In addition, patterns in the scaled radiosity image of BC have sharper boundaries and edges than those in CCD image. This discrepancy maybe

attributed to the milling inaccuracies: the relative lack of high-frequency detail in the CCD image reduces the amount of multiple scattering.

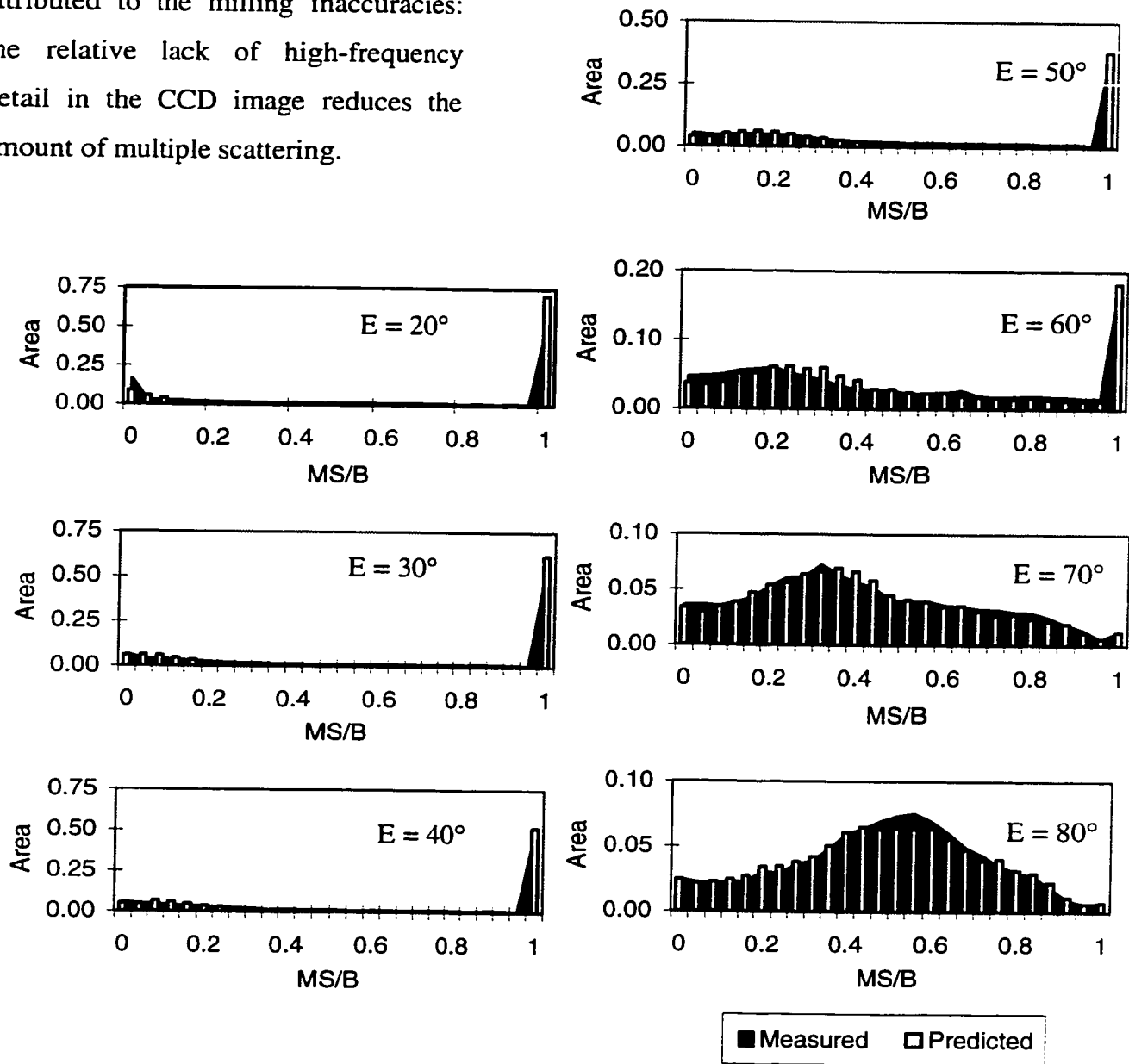


Figure 20. The diagrams show how the distribution of the MS component in scene varies with the illumination elevation angle (E) for test surface TA. The “measured MS” is found by subtracting the scaled SS component from the CCD measured radiance, and the “predicted MS” is found by subtracting the SS component from the scaled radiosity. The horizontal axis is the fraction of the radiosity due to multiple scattering in each pixel, and the vertical axis is the area fraction in the scene. Note the y-axis scale is different from histogram to histogram.

MS histograms: variable illumination

The MS distribution is not only controlled by the surface structure or roughness, but also by the illumination direction (both elevation and azimuth angles). The changes of the illumination direction will change the distribution pattern of direct illumination (SS) and consequently will affect the multiple scattering (MS). In order to verify the prediction consistency for varied illumination directions from this hybrid radiosity model, I compare histograms of the scaled MS component calculated for surface TA for a range of illumination elevation angles. In Figure 20, scaled MS histograms from both the model (“predicted”) and the CCD measurements (“measured”) are plotted together for each illumination elevation angle.

In Figure 21, the “measured” data represent scaled MS calculated by taking difference of the scaled SS and the CCD image, and “predicted” data represent MS calculated from the model. The horizontal axis is the amount of MS light, normalized by the local radiosity at each pixel. The vertical axis is the area fraction of the whole image. In the lower range of illumination elevation angles (less than 60°), the scaled MS histograms are bimodal. The peak for high values corresponds to shaded slopes and shadows, where the SS is very small, so that the radiosity is dominated by MS. The other peak represents MS in sunlit areas, where direct illumination accounts for a high fraction of radiosity. These two peaks migrate towards the center of the X-axis and start to merge as the illumination elevation angle is increased.

MS histograms for both the predicted and measured terms appear similar for $20^\circ \leq E \leq 80^\circ$, indicating that the MS predicted from the model is well verified by the CCD measurements. The change of histograms over the illumination elevation angles for both “predicted” and “measured” MS is almost identical: the bimodal histograms at low illumination elevation angles (20° - 60°) become unimodal at $E > 60^\circ$. There are only minor discrepancies between the predicted and measured histograms (Figure 20). Those

errors are attributed to the DTM geometric mismatch between the physical surface TA and the computer-simulated DEM of surface TA, as discussed above.

QUANTITATIVE ANALYSIS OF MATCHING DIFFERENCES

In this section, I will discuss in detail the discrepancies among the different images, assessed both visually and quantitatively. The difference between the scaled radiosity and CCD images shows the spatial distribution of the areas of disagreement. To aid in the comparisons, I have calculated a residual image of $(B/\pi - L)/(B/\pi)$, the radiance difference (“predicted” and CCD “measured” radiance) normalized by the local predicted radiance (scaled radiosity). If the two input images are the same, the residual image should ideally be flat with zero values, but in reality it has no zero values at all, because of errors in geometric location, illumination geometry, and radiosity estimations. Most of the radiance mismatches due to the geometric errors (between the physical and computer simulated surfaces) can be predicted and evaluated by the pattern of error in the residual images. The residual images for both surfaces TA and BC are discussed below.

Overall, the residual image for surface TA has low contrast and low values (<5%) for the whole image, except for seven narrow high-value strips along the ridges and valley bottoms (Figure 21a). Over most of the hillsides, the radiance mismatch term is less than 2-3%, but the errors are quite different on the two slopes at the ends of the surface model (north and south); 0% on the north and <10% on the south. There was no MS contribution on these slopes, only direct illumination, because of the finite nature of the surface extent. The north-end slope was in shadow with zero value. The high errors on the south-end slope were caused solely by inaccuracies in slope and illumination angles, which mainly affected the SS component. The high values (up to 25%) of radiance mismatch values along the ridges and valley bottoms were obviously related to DTM inaccuracies there. After taking account of the geometric mismatch and registration errors in the range of 3-4%, the residual image (<5%) shows good agreement for the

hillslopes interior to the model, indicating that the predicted radiance is accurate within 1-2%. Most of the high errors are independent of the radiosity model.

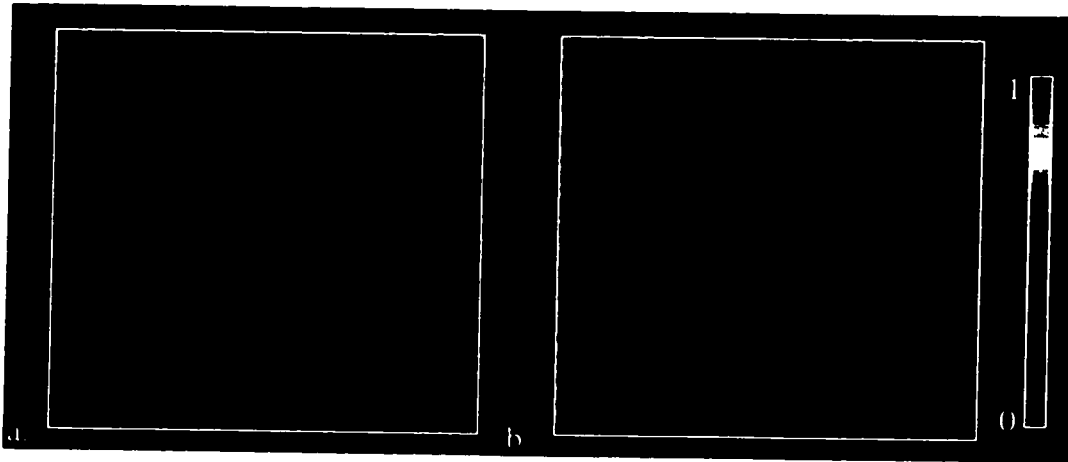


Figure 21. Residual (difference) images for test surface TA (a.) and BC (b.). The residual images are the differences of predicted radiance B/π and measured radiance R normalized by the maximum B_{max}/π . The scale on the right shows the color-coded residuals in the range of 0% to 100%.

The residual image for surface BC shows greater discrepancies. Most high radiance mismatch areas (10-20%) are located in valleys and follow the drainage pattern (Figure 21b). Because the geometric discrepancies between the milled surface and the DTM model are large, the residual image is strongly affected by topographic geometry. In general, the bigger and deeper the valley is, the greater the discrepancy. The complexity of the BC surface has increased the difficulty in separating the radiance mismatches caused by the systemic errors from the radiosity prediction, so it is not clear what the accuracy of the radiosity model is.

RADIANCE MISMATCH AT DIFFERENT ILLUMINATION ELEVATION ANGLES

The radiance mismatches of the scaled radiosity and CCD images are also affected by the illumination geometry. Lower illumination elevation angles (E) usually enhance

these mismatch errors, because SS depends on $\cos(\tau)$. When E decreases, for typical terrain slopes of 10° - 30° the local incidence angle (τ) typically increases and, in turn, increases the sensitivity $\partial B/\partial\tau$ of radiosity ($B = I_r \cos\tau + MS$) to τ , which is proportional to $\partial\cos\tau/\partial\tau = \sin\tau$. Thus, the SS error from the DTM is exaggerated by decreasing the illumination elevation angle.

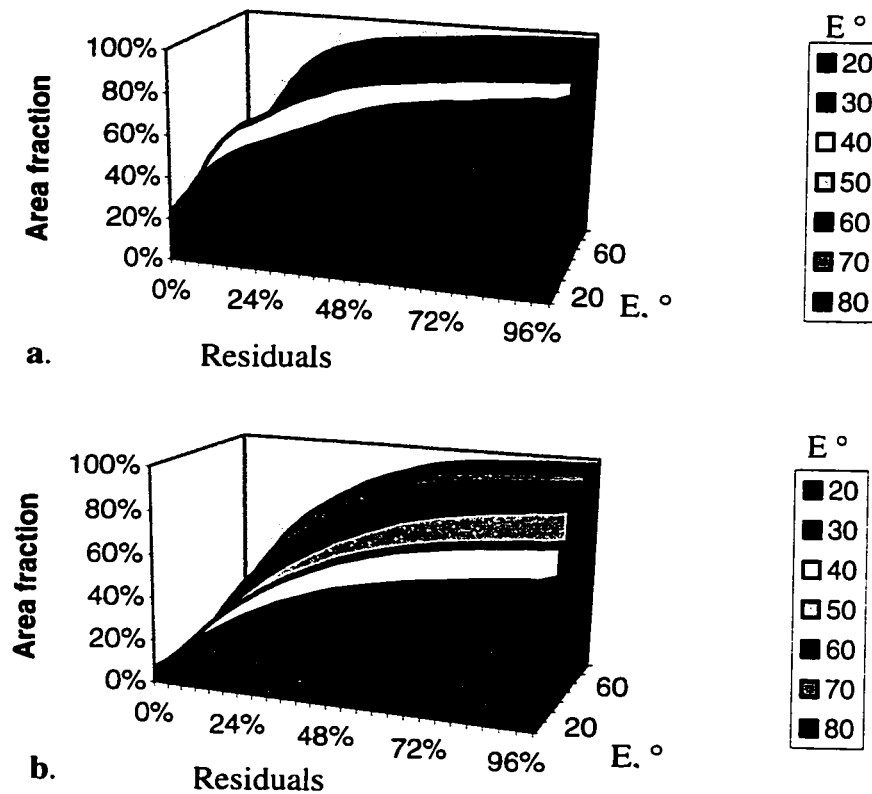


Figure 22. Cumulative histograms of mismatch errors (residuals) for test surface TA (a) and BC (b). The mismatch error in percentage is $(B/\pi - L)/B_{\max}/\pi$. E is the illumination elevation angle.

The cumulative histograms of radiance mismatch also show this trend. Figure 22 shows the cumulative area fractions plotted against the mismatch error (in percentage of radiosity) for surfaces TA and BC. Both histograms rise steeply from low values (areas) as the mismatch fraction is increased, gradually leveling off at high values. The steeper the slope, the smaller the mismatch, and, therefore, the better the match results. In other

words, a high value area fraction at low radiance mismatch values indicates that most of the image is affected by only small mismatches.

Figure 22 shows the cumulative histograms for different illumination angles. The most obvious feature is that the steep slopes of the histograms become even steeper as the illumination elevation angle is increased. The area fraction at low illumination angles is always smaller than at high illumination angles for every radiance mismatch value. This trend is much stronger for surface BC than for TA. For example, for surface BC, the area fraction value (as example, the radiance mismatch is $< 20\%$) increases from 0.2 at $E=20^\circ$ to almost 0.7 at $E=80^\circ$; for surface TA, the same area fraction value increases from 0.45 to 0.85. The other feature is that all the high plateaus in the histograms for surface TA have similar values around 80%, whereas for surface BC the plateau value increases from 40% to 90% as E increases from 20° to 80° . These differences suggest that the CCD measured radiance is much closer to the scaled radiosity for surface TA than for surface BC, and also indicate that the accuracy of the radiosity model is closely related to the complexity of a surface.

SIGNIFICANCE OF MULTIPLE-SCATTERING

The area contaminated by a given amount of MS (e.g., 20%), which is represented by $A_{20\% \text{ MS}}$, is a parameter that describes the percentage of an image containing a significance amount of MS. In Chapter 2, the $A_{5\% \text{ MS}}$ fraction was adopted to show the percentage of a image being affected by the MS for the surface reflectivity of 30%. Here, because a surface reflectivity of $\sim 90\%$ was used, a higher threshold value must be chosen in order to show the changes of the area fraction with illumination elevation angles properly: otherwise the area with 5% MS will cover $>90\%$ of the image.

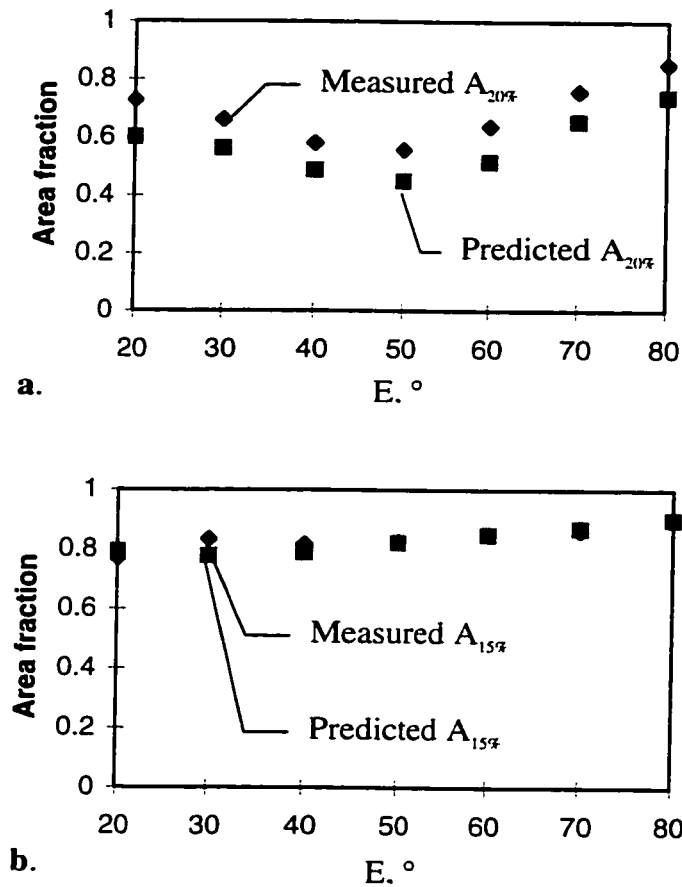


Figure 23. Plots of the area fraction as a function of illumination elevation angle, E . a). Area of the surface TA for which $MS_i/B_i > 20\%$. b). Area of surface BC for which $MS_i/B_i > 15\%$.

Figure 23a shows the area fractions ($A_{20\%}$ MS/B) plotted against illumination elevation angle for both the “predicted” and “measured” MS images of surface TA. The overall shape of the two curves (calculated from the predicted radiance and the CCD radiance, respectively) are matched well, although they are offset. The high peak values ($A_{20\%}$ MS) occur at both low illumination angles ($E = 20^\circ$) and high illumination angles ($E = 80^\circ$), whereas the minimum occurs near $E = 50^\circ$. The value of $A_{20\%}$ has a close relationship with E : when E is low, larger areas of the image are in shadow, and MS is the dominant factor in B; and as E increases, the shadow area decreases, and $A_{20\%}$ is reduced. As E increases further, the increasing area being illuminated leads to more MS in the

scene. When E exceeds a certain value (e.g., $E = 50^\circ$), the effect of increasing MS overcomes the effect from decreasing shadowed area, and therefore, $A_{20\%}$ MS increases.

The two curves in Figure 23a are offset by a constant $\sim 10\%$. This offset, which is consistent through all illumination angles, indicates a systematic radiance error between B/π and L . As noted above, surface TA has extensive edge effects. In all, the seven edges (three on top and four at the bottom) count for about $\sim 10\%$ of the total surface area -- the same as the offset between the curves. By removing the 10% offset here attributed to the inaccurate DTM, the two curves match closely, indicating that the radiosity model has predicted the MS component correctly outside of the identified problem areas. This evidence further indicates that radiosity model has only $<1-2\%$ error after accounting for the systematic geometric errors.

$A_{15\%}$ MS has been selected as the threshold values for surface BC in Figure 23b, because of its surface complexity and smoother than surface TA. The curves are more linear than for TA, but still show the area fraction increases (from 0.8 to 0.9) as E is increased from 20° to 80° . In comparison with surface TA, surface BC has a smoother topography (lower aspect ratio). From $E = 20^\circ$ to 80° , the CCD measured radiance curve has almost identical linear shape to the predicted, except for some differences between $E = 20^\circ$ and 50° . As discussed above, at low elevation angles, the radiance mismatch from inaccurate DEM is exaggerated. Even though the DTM for surface BC has numerous problems, the radiance mismatch for the worst case affects less than 5% of the image, again showing the accuracy of the radiosity model.

The radiance mismatches between the two curves due to the DTM inaccuracies also vary with the threshold values of area fraction (e.g., $A_{5\%}$ to $A_{20\%}$). The trend of dependency is complicated, but surely relates to the degree and geometric location of the inaccuracies of DTM. In general, the higher threshold the value, the more radiance

differences occur between the predicted and the measured, because of the higher variation of high frequency of DEM between physical surface and the digital surface.

DISCUSSIONS AND CONCLUSION

The radiosity model was validated by laboratory measurements for two different surfaces. The results predicted by the model were compared to CCD radiance measurements for different illumination geometries, using 1-D histograms, scatter plots and 2-D images, for a simple geometric surface (TA) and a real landscape surface (BC). Comparison was made by direct matching of results, by analysis of mismatches, and by comparison of local MS effects at a scene element to integrated effects over an image. All the comparisons showed that the majority of modeling results are well matched by the measured CCD images.

The verification of the radiosity model confirms the conclusion that using SS to approximate the radiosity is not accurate, and that MS is a major component in the reflectance from rough surface. Conventional image calibration without considering the MS in a image is not accurate, especially for highly reflective surfaces, such as snow or NIR vegetation. Inaccurate reflectances resulting from this oversight may introduce errors in remote-sensing applications.

Inaccurate DTMs are the major source of uncertainty in the verification of the radiosity model. They cause consistent systematic errors for all the comparisons, affecting both the SS and MS components. As the illumination elevation angle decreases, the effect of the inaccurate DTM is magnified. The worst situation is when the illumination angle is close to the local slope, resulting in large local incidence angles.

In general, the maximum MS and radiosity are both strongly sensitive to the local changes in the DTMs. The inaccurate steeper slopes of DTM may cause overestimation of MS and radiosity values, but the inaccurate smoother slopes may cause

underestimation of MS and radiosity values. However, the area with a given amount of MS is less sensitive to the high-frequency variation of the DTM than to the overall terrain shape, or low-frequency component of the DTM. It describes the total coverage of MS in the scene.

The scattering properties of the surface may also affect the radiosity. Because the materials used in this study to construct surfaces were nearly Lambertian, the effects of violating the Lambertian assumption is not clear. This is an important issue from the practical point of view, and should be examined in the future studies.

Making allowance for the systematic errors in the experiment, the comparison of the radiosity model and CCD image showed great similarity. The overall modeling results were well matched by the measured CCD images, indicating the new hybrid radiosity model is correct and accurate and its prediction is reliable and applicable. From quantitative evaluation of the mismatches in two situations -- difference images and $A_{20\%}$ MS -- the accuracy of the predictions from the radiosity model proved to be less than 1-2%.

CHAPTER 4: SEMI-EMPIRICAL INVERSION OF TM IMAGES FOR SURFACE ROUGHNESS

INTRODUCTION

Visible and near-infrared (VNIR) radiance recorded in Landsat TM images primarily contains information on two attributes of natural surfaces: surface roughness and composition of surface materials. Separation of surface roughness information from the image data is of importance in many fields. Surface roughness contains an integrated record of past climate conditions, since it is influenced by erosion, aeolian deposition, desert pavement formation, and other geological processes. Surface roughness is a key parameter to reconstruct past climate to the understanding of impact of contemporary global changes on the Earth's surface, leading perhaps to the reconstruction of climatic history (Evans et al., 1992; Sellers et al., 1995). In geology, surface roughness relates to the age and history of a surface, and can be used to infer tectonic history and sedimentary environment (Farr, 1992). Because it controls unresolved shading patterns and shadows, roughness is also important to the interpretation of most remotely sensed images. Driven by those reasons, a great amount of work has been directed to the problem of determining surface roughness from Landsat imagery (Schaber et al., 1976; Evans et al., 1992; Farr, 1992; Austin et al., 1994; Weeks et al., 1996).

Most of roughness inversion models have been developed for airborne or spaceborne synthetic aperture radar (SAR) data (Zebker and Goldstein, 1986; Evans et al., 1988; Evans et al., 1992; Shoshany, 1993; Weeks et al., 1996; Smith et al., 1996). These inversion models basically fall into two categories: theoretical models such as the small-perturbation model (e.g., Zebker et al., 1987; van Zyl et al., 1991) and empirical models based on experimentally determined relationships (e.g., Oh et al., 1992; Dubois et

al., 1995; Shoshany, 1993). In general, both the approaches are successful under restricted conditions and often work well in the geographic and physical circumstances in which they were developed and tested. However, roughness inversion models with more general applicability have yet to be demonstrated. One of the major difficulties is attributed to the complexity of natural surface to which the radar signal is sensitive. Any changes of the geometry of the surface structure will affect the inversion results greatly.

The radiosity of a surface varies with the roughness, as presented in Chapter 2, because of shading, shadowing, and multiple scattering in the scene. Thus, in principal, VNIR data could be used to characterize and quantify surface roughness. However, using VNIR images to study surface roughness has not yet widely been attempted because of difficulties in separating the reflectivity and shadowing (roughness) information. One effort to extract roughness information from VNIR images (Weeks et al., 1996) exploits the theoretical relationship of reflectance to surface roughness in TM images. Weeks et al. (1996), however, stopped short of inverting the surface roughness from an image directly. Instead, they used empirical approaches from field and image data to optimize the inversion filter. Empirical methods inevitably contain errors from both field and image training data and therefore, produce unstable results of the inversion. A semi-empirical inversion of VNIR data, which relies only on laboratory spectral measurements and the theoretical relationship of radiance and roughness, could limit these errors and produce relatively stable estimation of surface roughness. The radiosity model enables the computing of the theoretical relationship, which could be used to separate the albedo and shadowing information. At the subpixel scale, multiple scattering has been proved to be important component of the radiosity values (see Chapter 2). For quantifying the radiance response to roughness, it is necessary to consider the MS component.

The primary goal in this chapter is to estimate the surface roughness from the spectra of a Landsat TM image, as an application of the radiosity model. Using the theoretical relationship of surface reflectance and roughness calculated by the radiosity

model, a semi-empirical inversion of surface roughness was generated based on a strategy termed as “foreground/background analysis” or FBA (Smith et al., 1994; 1996), which basically is an application of the principal component analysis algorithm. The FBA essentially separates the image data into two groups: foreground and background, to quantify explicitly the effect of background factors (such as vegetation, rock types, water, and more) on the interpretation and inversion for a foreground entity such as roughness (Smith et al., 1994; 1996; Weeks et al., 1996). This inversion model is expected to reduce the unstable factors caused by differences in sampling scales and locations. The new inversion results are compared with other inversion methods driven by field and image data.

A major focus in developing the semi-empirical inversion is on techniques for determining finite impulse response filters (FIRs) for different data sets. A FIR filter is a principal component optimized by a set of training data to indicate the foreground. Differing from empirical approaches, which rely on field data or image data to define the foreground vector in the multiple dimension space -- the multiple spectral bands in TM images -- the semi-empirical inversion uses the laboratory spectral measurements and the theoretical relationship of radiance to roughness to determine a stable FIR, which will produce consistent estimates of surface roughness for each image. Thus, the roughness inversion of FBA equipped with this semi-empirical filter could provide stable, reliable estimates of surface roughness from Landsat TM images.

INVERSION MODEL

In fact, FBA represents an extension of spectral mixture analysis (Adams et al., 1986; 1989; Smith et al., 1990a, b; Gillespie et al., 1990; Gillespie, 1992; Sabol et al., 1992) that allows any number of spectra to be included in the unmixing process by separating them into two categories: foreground and background spectra. The foreground refers to spectra which give a substantial contribution from a desired physical variable

such as surface roughness, and the background includes the spectra which has minimal contribution from that same variable and a contribution from undesired variables (such as roughness at large scales or vegetation).

The FBA inversion can be changed by optimizing different FIR filters. There are three ways to optimize the FIR filter: using image data, field data, or theoretical relationships. In the field-data method, actual field data (in this case, roughness Y_n) are used to optimize the selection of the FIR filter weights w_b by solving the general equation of the FIR filter, using singular value decomposition:

$$Y_n = \sum_{b=1}^m (w_b \sigma_b) + K + \varepsilon \quad (1)$$

where roughness Y_n (n : sample number) is the output of the filter, σ_b refers the TM image data for six bands ($b = 1, 2, \dots, 6$), m is the number of the bands, K is a constant which is required because the radiance of shadow in the TM image may not be zero in DN, and ε is an error or fit term. The error in solving for w_b in equation (1), although not shown explicitly, is in units of the driving measure Y_n (e.g., for roughness this would be in units of rms height, slope, or offset). By comparing the standard deviation of this error to the range of a given parameter within an image, the detectability of the foreground with respect to the background can be estimated.

For finding the w_b vector, both Y_n and σ_b must be known for all TM bands. In the field-data method, the Y_n are calculated from field measurements at the meter scale with a technique of close-up stereophotography (Weeks et al., 1996) -- indicating roughness of a geological surface, whereas the σ_b are sampled from the TM image at the 30-meter scale (and include topographic roughness information such as canyons, ravines, washes). The actual roughness extracted from a TM image may be different from what can be measured

in the field at a different scale. This scaling error will propagate into the w_b calculation and will introduce inevitable errors in this inversion method.

In the image-data method, the FIR filters are calculated in a slightly different way. First, the image is treated as a composite of areas of foreground (roughness) and background (other variables). Image-derived spectra, σ_b , comprising the foreground and background sets, are used to find the solution vector, w , such that the projection of all background vectors along w_b is as close as possible to zero, and the projection of all foreground TM image data vector onto w_b is as close as possible to unity. The w_b vector defines an optimum projection in the hyperspace defined by the multiple spectral bands (six TM bands in this study), separating the foreground from the background. A set of equations is generated for a collection of background and foreground spectra as follows:

Foreground

$$I = \sum_{b1=1}^m w_{b1} \sigma_{b1} + K + \varepsilon \quad (2)$$

Background

$$O = \sum_{b2=1}^m w_{b2} \sigma_{b2} + K + \varepsilon \quad (3)$$

Again, singular-value decomposition is used to determine a single w_b vector and constant K that optimizes both foreground and background equations simultaneously. Solutions can be sought that minimize the effects of surface orientation, intermediate-scale topography, or other spectral variations, by choosing spectra from the image that assign such variability to the background.

Precise and accurate selection of foreground and background for optimizing the w_b vector is critical for the image-data method. Some field knowledge of the foreground and background components is required for selecting training data sets. Rough surfaces, for

example, can be selected from large-boulder alluvial fan surfaces, and the different types of surface materials as background can be selected from lake deposits, sand dunes, or volcanic deposits. It would be ideal to select the background surfaces that are of same roughness, but have different reflectivities. Usually, the selection of appropriate test sites is affected by human knowledge of the field, so that the inversion for roughness using this method could be unstable.

The third method, called the theoretical relationship method (or semi-empirical inversion method), is similar to field-data method and uses the same singular value decomposition of equation 1. Instead of using field data to optimize the FIR filter, the semi-empirical method applies a theoretical relationship for deriving the filter. In this approach, σ_b (reflectance for six bands) is calculated based on semi-empirical data rather than the field roughness measurements. The details of defining the theoretical relationship and the ways to compute σ_b are discussed in the next section.

The theoretical-relationship method will reduce the inevitable sampling errors in field-data and image-data methods, because the rock spectra are measured on flat prepared surfaces in the laboratory, and the theoretical relationship of surface reflectance to roughness is calculated for computer-simulated surfaces. However, uncertainty will be introduced by the simulation of the surfaces, because the simulated surfaces are generated mathematically with a limited number of parameters, which may not be enough to describe natural surfaces.

OPTIMIZED FINITE-IMPULSE-RESPONSE (FIR) FILTER

To calculate the w_b vector by the theoretical relationship method, first it is necessary to define quantitatively the theoretical relationship of the surface reflectance to surface roughness. The radiosity model is used to construct the relationship for a series of computer-simulated rough surfaces.

COMPUTER-SIMULATED SURFACES

It is important to select an appropriate method to generate simulated surfaces that are similar to natural surfaces in terms of their reflectance changes with surface roughness. There are several models commonly used to describe the roughness of a surface mathematically from their DTMs, such as rms height, and the surface spectral power-law method (described by two parameters: the slope and offset of lines fitting Fourier spectra of a DTM). One-parameter methods (such as rms height) are of simple form, but are not sufficient for describing and constructing complicated two-dimensional surfaces (Weeks et al., 1996). Two or more parameters (as in the power-law method) can give more accurate descriptions of real surface structure, but require additional complicated mathematical treatment. Weeks et al. (1996) have suggested adding a third parameter: the phase angle in Fourier transform. Mathematically, this has prove difficult to implement.

Previous work on natural surfaces has indicated that, in many cases, one-dimensional power spectra obey a power law (Sayles and Thomas, 1978; Brown and Scholz, 1985; Austin et al., 1994). Some application studies have supported this finding (Farr et al., 1986; Evans et al., 1992; Farr, 1992). The power-law spectral presentation of surface roughness is a more complete description than rms height, since it contains the scaling and complete statistical information, if phase is included (Weeks et al., 1996; Goff, 1995). In reconstructing the simulated surface, the power-law method produces more natural appearing surfaces than the rms-height method. Therefore, in this study, I chose the power-law method, inverting the slope and offset of power-law spectra using the FFT (fast Fourier transform) with randomized phases to create DTMs of simulated natural surfaces.

The general approach (Austin et al., 1994) of parameterizing the power-law spectrum is to fit a function ($F(k)$) to the mean power spectral density calculated from the FFT of the DTM:

$$F(k) = Ck^{-m}, \quad (4)$$

where k is wavenumber ($2\pi/\lambda$: λ is the wavelength), and C is the amplitude of each wave. The equation is linear in log-log space:

$$\log(F(k)) = \log(C) - m\log(k), \quad (5)$$

and the two parameters, $\log(C)$ and m , are the offset and slope of the power spectrum, respectively. Field surveys of surface roughness by Weeks et al. (1996) indicate that many natural surfaces are defined by the slope (m) in the range of $-2 < m < -3 \text{ cm}^3$ and the offset ($\log(C)$) in the range of $-2 < \log(C) < -4 \text{ cm}$. As would be expected, the rms height of the surface, being related to the area under the spectrum, is positively correlated with $\log(C)$, the offset term.

Given the pairs of slope and offset from field measurements, computer-simulated surfaces were generated using the inverse FFT, assuming random phase angle. This assumption is a major source of error in the simulated surfaces generated this way (detailed discussion in Weeks et al., 1996) and this problem does not appear to have been satisfactorily solved. Even though the power spectral method has this unsatisfying problem, the simulated surfaces produced this way appear to be better than those produced by the rms method (Pak et al. 1995; Weeks et al. 1996). The FORTRAN code from Pak et al. (1995) was used to generate the computer-simulated surfaces for different slope and offset terms. The radiosity model was then applied directly to these surfaces for computing the radiance response to surface roughness. Examples of simulated surfaces are shown in Figure 24. There are two main circular paths in the figure showing how the surfaces are changed by varying the slope term (upper circle) and the offset term (lower circle). The upper circle displays the surface changes for slopes of -1.45 , -2.05 and $-2.95 \text{ (cm}^3\text{)}$ with a fixed offset term of -1.73 (cm) . As the slope is increased, the spacing of surface features increase, but their amplitudes do not. In the lower circle, the

amplitude of the surface structure decreases dramatically as the offset is reduced from -1.73 to -2.53 to -3.73 (cm), while the slope is held constant at -1.45 (cm^3). It is clear that the offset term is the dominant one controlling the roughness of surfaces.

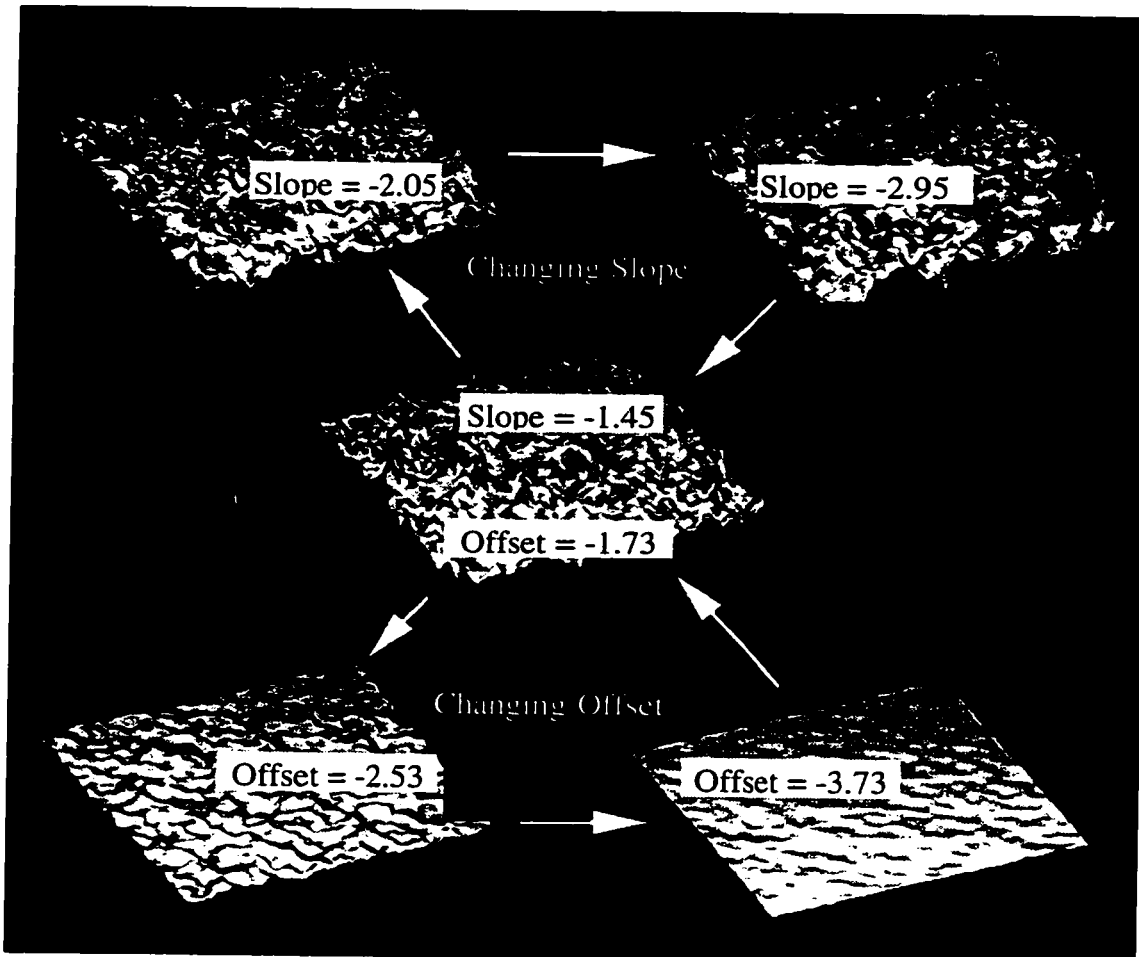


Figure 24. Examples of computer-simulated surfaces generated from the offset and slope terms of synthetic power-law spectra with random phase angles. The upper circle (indicated by arrows) shows the changes of surfaces as the slope term is changed; the lower circle shows the changes of surfaces as the offset term is changed. For these examples, the spatial scale and field of view are arbitrary: the simulated surface might represent the surface of a sand dune or it might represent a mountain range of equal offset values. The offsets is in unit of cm and the slope is in units of cm^{-3} .

REFLECTANCE FROM SIMULATED SURFACES

The radiosity model was used to calculate the reflectance from the simulated rough surfaces. Each simulated surface has been subdivided into 100x100 elements. The reflectance was integrated over all the radiosities calculated for the individual elements. As presented in an earlier chapter, the radiosity values are computed using following equation;

$$B_i = \rho_i * I_{rrd} * \cos(i_i) + \rho_i * A_{dm} + \rho_i \sum_{j=1}^n B_j * F_{i,j} \quad (6)$$

By assuming the surface has uniform reflectivity, and by ignoring the downwelling atmosphere radiation, the equation is simplified as:

$$B_i = \rho_i (I_{rrd} * \cos(i_i) + \sum_{j=1}^n B_j * F_{i,j}) \quad (7)$$

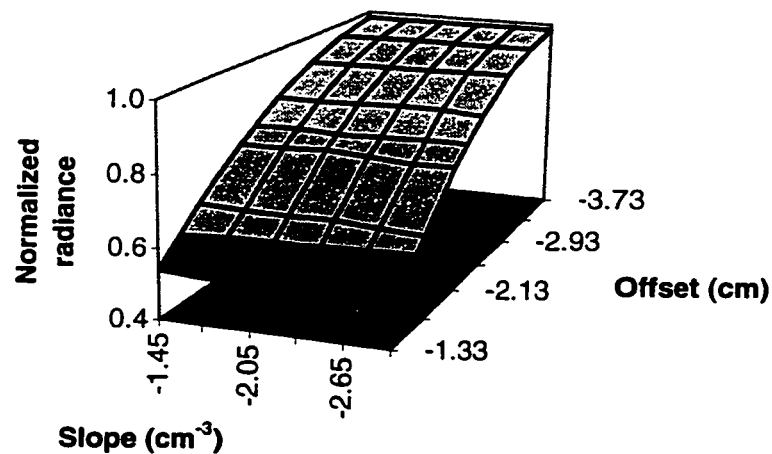


Figure 25. VNIR normalized radiance (to flat surface) as a function of slope and offset parameters for simulated rough surfaces, defined by power-law spectra with random phase angles.

Given the irradiance term ($I_{rrd} = 200 \text{ Wcm}^{-2}$), the radiosity value varies only with surface reflectivity ρ_i and surface roughness, a function of $\cos(i)$ and F_{ij} . Under the Lambertian assumption, the reflectance from each rough surface element is directly proportional to the radiosity (B) with a factor of π (see Chapter 1).

Before applying the radiosity calculation to rough surfaces, it is important to know how sensitive the reflectance is to each coefficient (offset and slope) of the power-law spectra. For this purpose, I have first fixed the surface reflectivity and then computed the reflectance for each rough surface by varying either the slope or offset term. Thus, the reflectance as a function of slope and offset was obtained, as shown in Figure 25. Clearly, the VNIR reflectance has a strong dependency on the offset, but almost no dependency on the slope term in the range of $-1.45 \leq \text{slope} \leq -2.95 \text{ cm}^3$. This offset dependency illustrates that the reflectance varies mainly with the amplitude (power) of the surface structure, instead of with the surface wavelengths at different scales. Thus, in this study, only the one parameter of roughness, the offset term, is used for relating surface reflectance and reflectivity for rough surfaces. By fixing the slope of the power spectrum at -2.05 cm^3 , which is a common value for natural surfaces (Weeks et al., 1996), I have calculated the reflectance as function of reflectivity for representative offset values. Figure 26 shows the variation of the calculated reflectance (or radiance) to the surface reflectivity and roughness. Figures 26a and c give the calculated reflectance (or radiance) with and without MS, whereas Figures 26b and d show the ratios of radiance normalized by the value of a flat surface of the same reflectivity. Comparison between Figure 26b and d shows the difference of reflectance due to the MS in the scene. Without MS, the radiance ratio does not vary with the surface reflectivity, whereas with MS, the radiance ratio increases with the surface reflectivity. This effect confirms that MS is proportional to the surface reflectivity, as discussed in Chapter 2. For a given irradiance ($I_{rr} = 200 \text{ Wcm}^{-2}$), and including the MS in the scene, Figure 26c represents the theoretical

relationship of surface reflectance to surface roughness, and provides the basis for building the FIR filter for semi-empirical inversion.

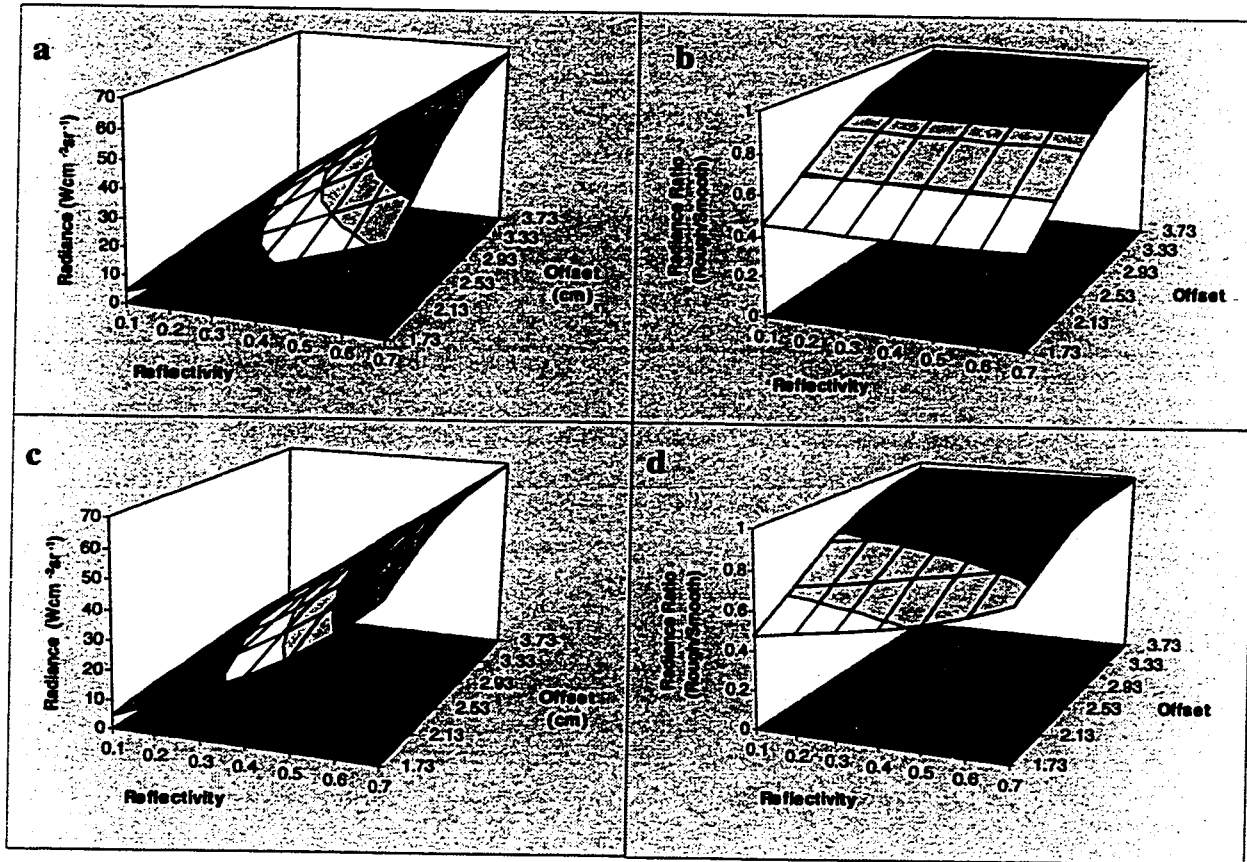


Figure 26. Radiance response to offset (roughness at subpixel scale) and reflectivity of simulated surfaces. Power spectrum slope has been fixed at -2.05 cm. a) Radiance (L in unit of $Wcm^{-2}sr^{-1}$) from rough surfaces without MS. b) Radiance ratio (L_r / L_{sm}) of rough to smooth surface, without MS. c) Radiance (L) from rough surface with MS. d) Radiance ratio (L_r / L_{sm}) of rough to smooth with MS. Color bands show zones of equal radiance or ratio.

LABORATORY MEASUREMENT OF ROCK SPECTRA

Twelve rock samples were collected from Grotto Canyon (GC) Wash in the Death Valley field area. They bracket a range of lithologies (mostly, limestone and dolomite),

but are only lightly weathered. The rock spectra were measured using a laboratory spectrometer (Perkin Elmer Lambda 19DM UV/VIS/NIR). They are shown in Figure 27 and listed in Table 3.

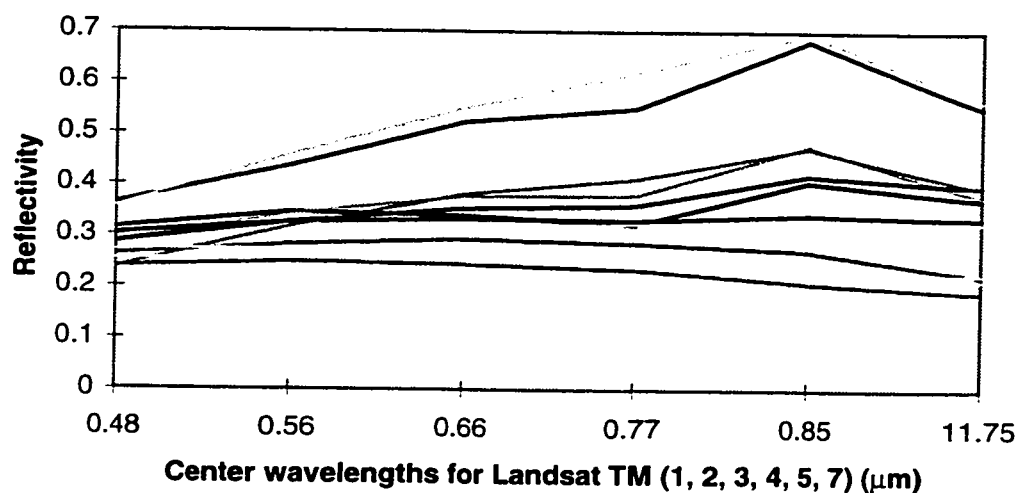


Figure 27. Spectra of twelve rock samples collected from Grotto Canyon Wash, Death Valley.

All the spectra were measured on a flat surface (2 cm diameter) in order to eliminate roughness effects on the spectra, which are inevitable in the image-based and field-based methods. The w_b vector, which was constructed based on the laboratory spectra of these rock samples, would contain no component of the roughness foreground in the assemblage of background vectors; therefore the estimates of roughness using the semi-empirical inversion contained less variations caused by background factors than other methods. If the collected rock samples do not cover all the rock types in the field, the w_b vector will not recover the foreground (roughness) properly, resulting in an imperfect estimate of roughness.

Table 3. Rock reflectivities for TM bands

Sample	TM 1	TM 2	TM 3	TM 4	TM 5	TM 7
# 1	0.31	0.34	0.33	0.32	0.40	0.37
# 2	0.23	0.24	0.24	0.23	0.20	0.19
# 3	0.28	0.31	0.32	0.32	0.34	0.32
# 4	0.28	0.34	0.37	0.37	0.47	0.37
# 5	0.36	0.43	0.52	0.54	0.68	0.55
# 6	0.28	0.32	0.35	0.35	0.41	0.39
# 7	0.26	0.28	0.29	0.28	0.27	0.22
# 8	0.30	0.32	0.33	0.33	0.34	0.33
# 9	0.23	0.31	0.38	0.41	0.47	0.39
# 10	0.35	0.45	0.55	0.61	0.69	0.56
# 11	0.27	0.27	0.27	0.25	0.23	0.21
# 12	0.25	0.25	0.25	0.25	0.23	0.22

FIR FILTER

When both a spectral library and theoretical relationship between radiance and roughness are obtained, the reflectance responses to surface roughness as represented by the offset term are calculated from each type of rock sample, as shown in Figure 26c. A fourth-order two-dimensional polynomial was used (with consideration of accuracy and computation) to fit the reflectance data for each simulated scene. Thus, the function of radiance σ_b to surface reflectivity ρ and roughness Y_n was defined for computing the w_b vector in equation 1: $Y_n = \sum_{b=1}^m (w_b \sigma_b) + K + \epsilon$. Each surface roughness corresponds to different reflectances in the six TM six bands. Six different roughnesses in the range of -1.73 to -3.73 (cm^2), which represent most common surfaces in Death Valley alluvial fans (Weeks et al., 1996), were used. The results are listed in Appendix 1.

Six roughnesses and twelve rock samples give a total of 72 linear functions (equation 1) for finding w_b for the six TM bands. This is an over-determined problem, easily solved. The solution is:

$$w_b = [0.29084, -0.31833, 0.01017, 0.08707, -0.14929, 0.20232].$$

This is the semi-empirical FIR filter for estimating of surface roughness with the FBA inversion algorithm.

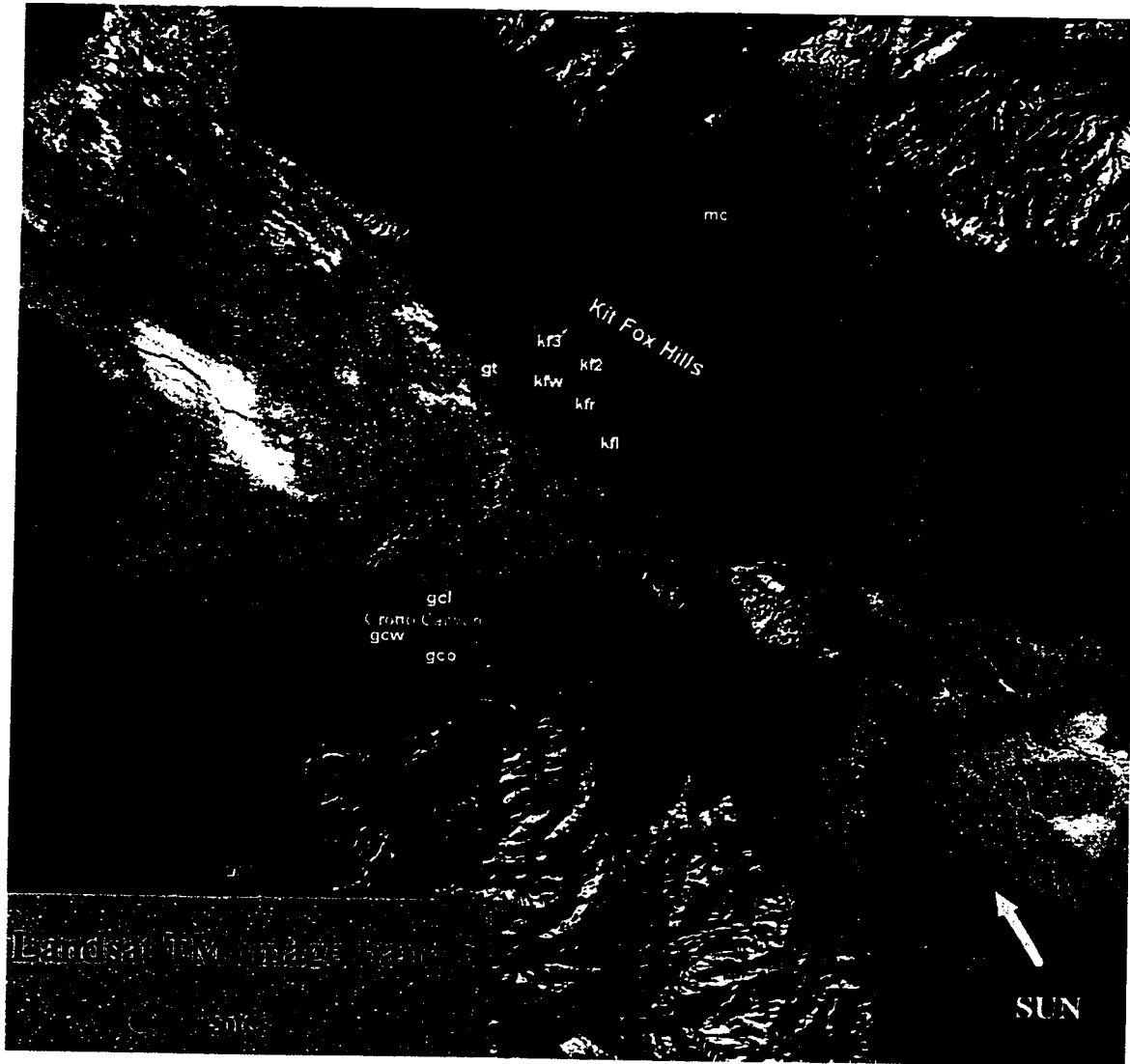


Figure 28. Landsat TM image of Death Valley, California shows the sites of roughness measurements on two alluvial fan systems: Kit Fox Hills and Grotto Canyon. At each site, the micro-topographic profiles have been measured using a close-up photogrammetric technique. “A” shows an unnamed alluvial fan. “B” indicates the playa unit in the upper left of the image.

RESULTS

Death Valley TM image acquired on December 09, 1982, was chosen to test the semi-empirical inversion method for surface roughness (Figure 28). Death Valley is a good site for the study of surface roughness because it is vast, largely vegetation-free and has alluvial fans of various ages and lithologies as well as lake deposits and sand dunes. The low vegetation cover in the valley provides an opportunity to measure the surface roughness of these geological units from aircraft and satellite images. Many studies have characterized the surface roughness using remotely sensed radar images (Wall et al., 1991; Farr, 1992; Evans et al., 1992). However, little attention has been given to using the remotely sensed VNIR data (e.g., Weeks et al., 1996). Recently, detailed field surface-roughness measurements were collected using close-up (2-m) stereophotogrammetry, for many locations on the alluvial fans in the Death Valley. These field data provide “ground truth” for testing remote estimates of surface roughness (Weeks et al., 1996). Location for the ground-truth sample sites are given in Figure 28, and their roughness measurements are listed in Table 4.

The TM image was calibrated using a simple empirical-line calibration method (Roberts, 1991). Two anchor points selected from shadow and gravel bar sites define the conversion line in a DN vs. reflectance plot. The coefficients of the conversion line for each band were then calculated. This calibration has not considered the differential atmospheric effects due to elevation differences within the scene (its effects may be less than 10%: A. R. Gillespie, informal discussion, 1997). There is 1000 to 1500 m elevation difference, which may cause < 4% variations of atmospheric scattering effects.

In this result section, I will present surface roughnesses estimated from these sites using the three different methods: the semi-empirical inversion, field-data inversion, and image-data inversion. A “shade” image, calculated using the fraction of darkness with assumption zero-radiance in shadow, is also presented and compared with these three

methods. All the inversion results were verified using the ground-truth surface-roughness data (Table 4).

Table 4. Roughness parameters calculated measurements of surface roughness by close-up stereophoto grammetry at 11 sites in Death Valley

Site	Offset (cm)	Slope (cm ³)
kfr	-1.88	-2.37
gt	-1.86	-2.45
kf3	-1.77	-2.50
gcl	-1.71	-2.62
kfw	-1.69	-2.41
kf1	-1.64	-2.71
kf2	-1.59	-2.57
mc	-1.58	-2.52
gco	-1.54	-2.29
gcw	-1.47	-2.44

ESTIMATES OF SURFACE ROUGHNESS

The semi-empirical inversion, in which the w_b vector was calculated from the theoretical relationship shown in Figure 26c, together with the rock spectra shown in Figure 28, applied equation 1 directly to the calibrated TM image data (σ_b) to estimate the roughness offset term. Essentially, the TM image data are projected onto the foreground/background line direction defined by the w_b vector in the hyperspectral radiance space of the six TM bands. The inversion result created a single image of the spatial distribution of roughness (Figure 29a).

For the field-data method, the w_b vector was optimized using the roughness data (offsets) measured in the field (Table 4), and reflectances (σ_b) sampled from the TM image for the same sites. Estimates of roughness using w_b vector are displayed in Figure 29b. Notice that this method contains estimated error from the sampling scale difference problem. The roughness measured in the field (at scale <10 m) is somewhat different

from the roughness shown in the image at 30-m resolution. This is an unavoidable source of errors.

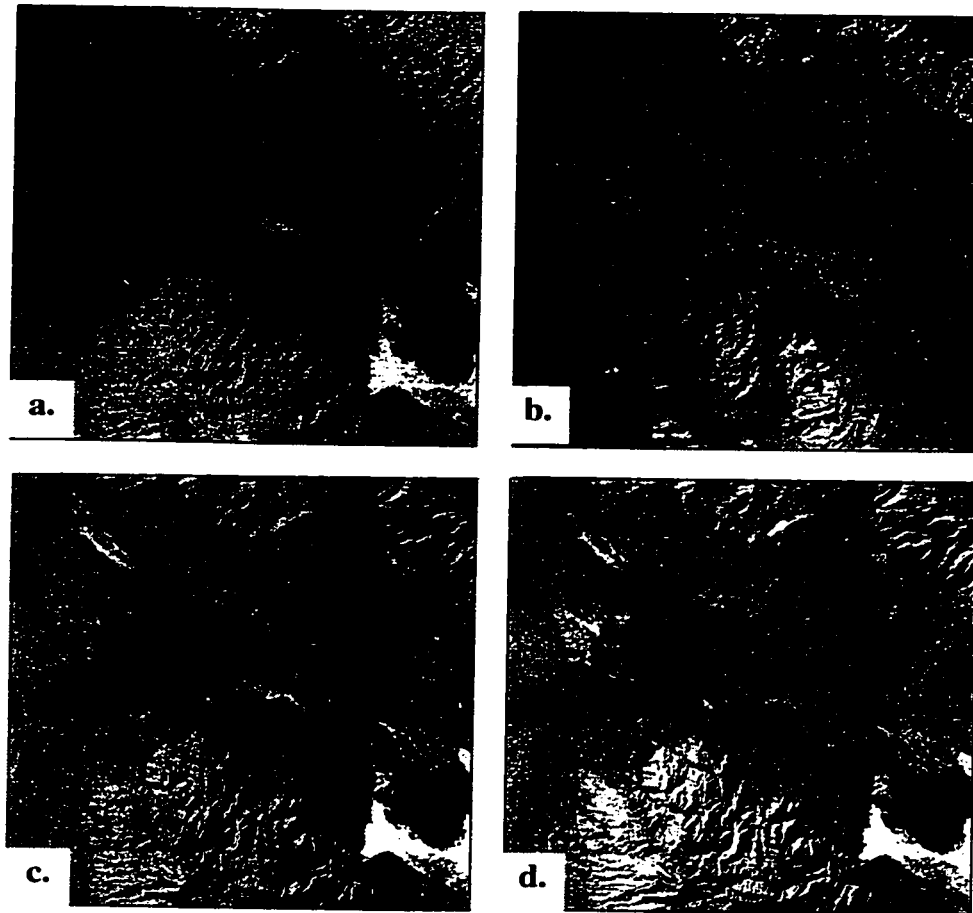


Figure 29. Surface roughness estimates from Landsat TM data using four methods. The brighter the roughness of the surfaces. Mountainous areas is not in consideration for subpixel roughness estimation. a). theoretical relationship (semi-empirical method) in which the FIR filter is optimized by modeling and Lab spectra. b). Field-data method in which the FIR filter is optimized by field roughness measurements. c). Image-data method in which the FIR filter is optimized by the image training data with known varied roughness. d). Shade-image method in which the FIR filter is optimized by the training data with known shade fraction.

The image-data method uses equations 2 and 3 to optimize the w_b vector. The training sites of both foreground (rougher surfaces) and background (smoother surfaces of various lithologies) were selected by inspecting the TM image. Field experience is important in selecting the training sites. Generally, the more diverse the background materials, the better the estimation of the foreground roughness. I have selected five training sites: a “rough” site on the Grotto Canyon alluvial fans; a “smooth” site on the playa surface; two intermediate sites on the Kit Fox fan and the “A” fan (Figure 28); and second “smooth” site on sand dunes. The estimated roughness image is shown in Figure 29c.

The “shade” image not only relates to the roughness (unresolved subpixel roughness), but also contains spectral information. In general, the shade fraction of a surface is proportional to its roughness (offset term), because of shadowing. However, poorly reflective surfaces can mimic areas of high shade in images, even though the surface maybe smooth. Surfaces with the same roughness but different reflectivities, will have different radiance or reflectances and will look different in the shade image. Thus, the shade image can only be used to predict a minimum value for surface roughness. The shade image is a minimum estimates of roughness for comparing the other three roughness images and is shown in Figure 29d.

Each roughness image has been scaled individually for maximum contrast to show the variation of the roughness values. For all four images, the brighter areas refer to rougher surfaces, and the darker areas to smoother areas. Mountainous areas, all subject to shading at the topographic (resolved) scale and therefore, give invalid estimates of roughness. Thus, the focus here is on roughness estimation for the valley floor areas, including alluvial fans, lake and aeolian deposits. The different estimates of roughness from these methods are discussed in next section.

CORRELATION OF ESTIMATES OF ROUGHNESS WITH “GROUND TRUTH”

I correlated the estimated roughnesses to “ground-truth” field measurements in order to verify the estimated results for the four inversion methods. Roughnesses were estimated from the images for locations where the ground-truth data were collected, but over much larger areas due to the 30-m sampling scale. Regression of the estimated roughnesses to the field measurements indicated their correlation for these particular sample sites.

As expected, the roughness image estimated from field data gives the best correlation coefficient ($R^2 = 0.94$) (Figure 30a), because its w_b vector was optimized using the same ground-truth data that were used to correlate with the estimates. The small fraction of the scatter above the fitted line is probably caused by the roughness variation from different sampling scales. However, the extendibility of the estimated roughness outside the training areas is not clear and requires more field data to evaluate.

The semi-empirical method estimates the roughness from the calibrated TM image. The regression coefficient is $R^2 = 0.72$ over the same field measurements as the data used in field-data method (Figure 30b). Even though its regression coefficient is smaller, this is misleading, and the roughnesses are actually better estimated, because they were obtained independently from the field measurements, and have no heritage from these field data. The $R^2 = 0.72$ thus indicates the true correlation of estimated and field-measured roughness.

Estimates of roughness using the same method were also made from the uncalibrated TM image. The regression to the field data is worse, $R^2 = 0.60$, because the w_b vector was based on the laboratory spectra, while the uncalibrated image has different spectra due to the contamination of atmospheric scattering effects. Thus, the calibrated image is required for the semi-empirical method. The quality of calibration may affect the precision of estimation of the surface roughness.

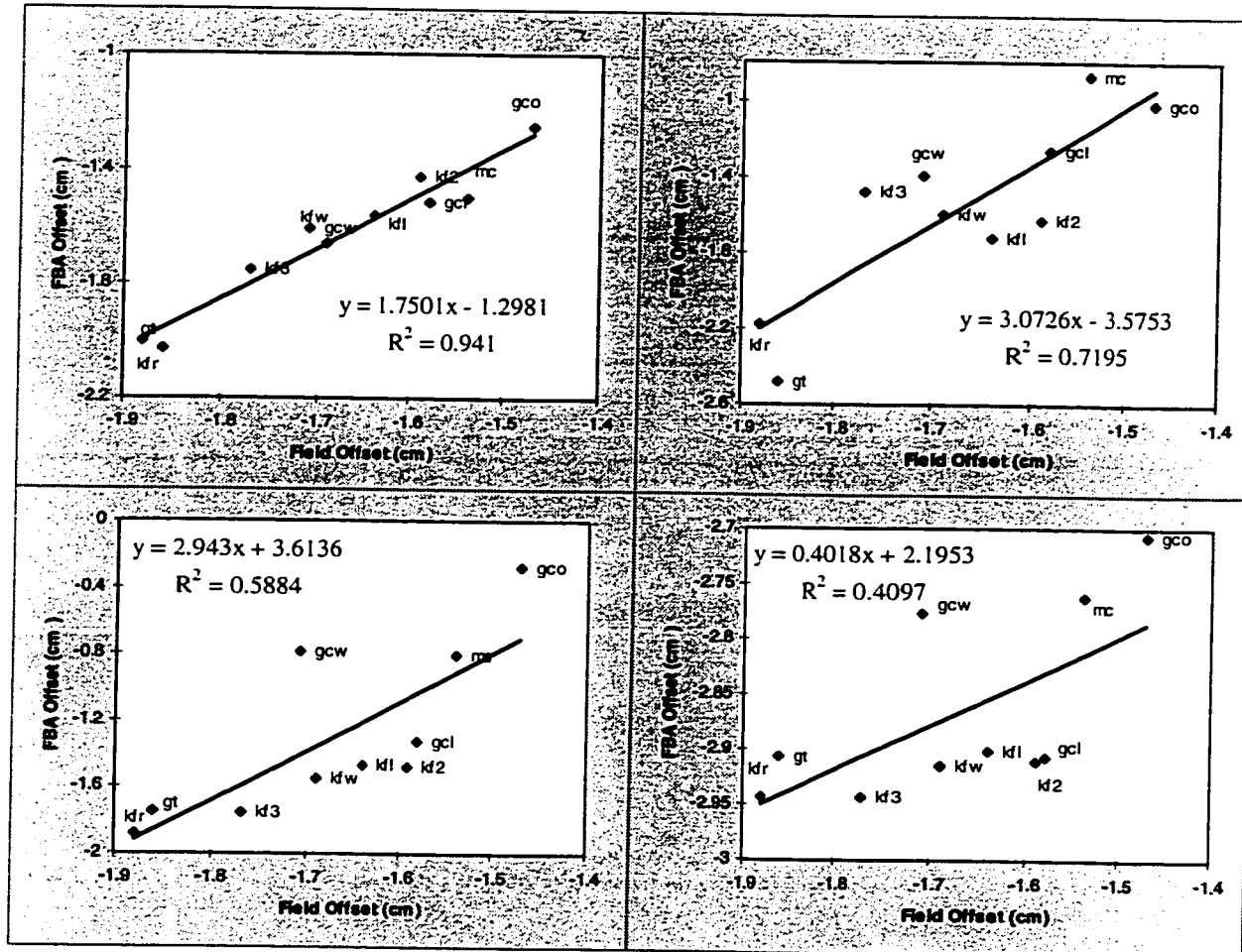


Figure 30. Linear regression of estimated roughness with field measurements for four methods. Note the y axis scales are all different. a) Field-data inversion. b) Semi-empirical inversion. c) Image-data inversion. d) Shade-image method.

The regression coefficients for the image-data method (Figure 30c) is less than for the semi-empirical method, $R^2 = 0.59$. The shade-image method has the minimum coefficient value among the four, $R^2 = 0.41$ (Figure 31d). As discussed above, both estimated roughness images contain the effect of spectral variability due to different rock types. From the two regression plots (Figure 30c and d), there are two separable data groups: one group below the regression line consisting of gcl, gco, gcw; and the other above the line consisting of rest of the data. By looking at the location of these field sites

(in Figure 28), it is clear that these two groups belong to two geological units: the Grotto Canyon alluvial fan and the Kit Fox alluvial fans. The two fan systems have different rock types (limestone and dolomite), causing spectral variations. In the two estimated-roughness images, the spectral variations are not well separated from actual roughness information. If the regression was applied to one group at a time, the coefficients are 0.15 higher. The accuracy of the image-data method may be improved if the foreground and background are better selected to optimize the FIR filter, but detailed knowledge of the scene is required to achieve that goal. In contrast, the shade-image method has no potential for excluding the spectral variation from the estimated roughness.

From the R^2 regression coefficients above, the evaluation of each method is quite limited, because a good match of predicted and field measurements implies that the particular inversion method is sufficient for the test sites, but does not imply that the method is extendible to other areas. For example, the field-data method has a high R^2 value, but it is unclear if that value is valid for other areas. However, if w_b is optimized from other methods which do not use these field data, then the correlation of estimated roughness to the field data is an independent test that is a useful estimate of performance. In the semi-empirical inversion, the w_b vector is optimized based on laboratory spectra and simulated surfaces, so that the correlation of estimated roughnesses to the field data indicates not only its accuracy, but also its extendibility. The R^2 coefficient value in the >0.7 range is probably of general significance for the semi-empirical inversion.

VISUAL COMPARISON OF ROUGHNESS ESTIMATES AMONG THE FOUR METHODS

Visual comparison is based on generalized knowledge of the large geologic units in the Death Valley TM image. Two units are selected for the comparison among the four roughness images (Figure 29): a large alluvial fan from a canyon in the upper right-hand corner of the image, labeled as A; and the playa in the left upper area, labeled as B. Physically, unit A has similar roughness to the Kit Fox alluvial fans on its left, but has a

different mixture of lithologies. The gravels of fan A can be clearly traced upslope, to the top of the image, shown as the darker unit in shade image. Unit B, the playa surface, is very smooth and may be subdivided on the basis of composition, mainly silt, halite, and other evaporate minerals. The wide range of spectral variation in unit B is clearly shown in the TM images (Figure 28).

If the roughness inversion methods work well, the estimated results should describe only the foreground information (roughness). Thus, unit A should have same apparent roughness as the Kit Fox fan, and unit B should be represented as smooth, by a dark color.

The shade image is not only a function of shade and shadow in the image, but is also affected by the spectral variation of the surface materials. Dark units could be rough and shadowed, or could be poorly reflective. The Figure 29d shows the estimated roughness from the shade-image method. Unit A in Figure 29d is represented with a dark color and has clear boundaries, darker than the Kit Fox alluvial fans; unit B is represented by many sub-units with different colors. Clearly, the two units in Figure 29d have inaccurately estimated roughnesses, because of the varied reflectivities of the surface materials.

Both the image-data method (Figure 29c) and field-data method (Figure 29b) separate the roughness and albedo information, but the separation relies entirely on the selection of sites used to select the w_b vector. If the training data do not represent all the materials in the scene, the albedo information (background) may “leak” into the roughness estimation (foreground). In these two methods, unit A is more similar to the Kit Fox alluvial fans than in the shade image (Figure 30d), even though a weak difference is still evident. Unit B still contains much spectral variation, as shown by sub-units in different colors. However, these sub-units have less color contrast than in the shade image.

The semi-empirical inversion method (Figure 29a) improves the estimation of roughness for units of A and B. With this approach, it is difficult to distinguish unit A from the Kit Fox alluvial fans (pointed by arrows). In the foreground image, both have same brightness (roughness), defining as a continuous unit at the front piedmont west of the Kit Fox Hills, and showing no difference in surface composition, even though the fan gravels have different provenances. Unit B is represented by a uniform dark color, indicating a smooth surface. The sub-units of unit B, which are seen in shade image, are not recognized in the semi-empirical roughness image. The playa incorrectly appears rough (light) in the other three roughness images, but is correctly represented as smooth (dark) in the semi-empirical inversion image.

The comparison among the roughness images made by the four methods has demonstrated that the semi-empirical inversion of roughness gives the most accurate representation and the best extendibility outside the training areas.

DISCUSSION

Inversions based on Foreground Background Analysis depend on how the finite impulse response (FIR) filter is optimized. In other words, they depend on the training data used for calculating the FIR filter, or w_b vector. The image- and field-data inversion methods rely on field measurements, together with some ground knowledge, so that their results are strongly affected by many factors, as discussed above. However, in the semi-empirical method, the w_b vector was optimized based on purely the theoretical relationship and rock spectra measured in the laboratory. The theoretical relationship was calculated by applying the radiosity model to a series of computer-simulated rough surfaces. Thus, the semi-empirical FIR filter was less sensitive to inaccurate field measurements and human knowledge. Modeling error associated with the semi-empirical inversion is related to the sensitivity of the reflectance to surface structure and to the variation of surface reflectivities. The amount of change of reflectance responses to the

surface structure without the random phase angle assumption is important to the theoretical-based inversion method. Changing the surface type from gravel bar to vegetation canopy may affect the theoretical relationship of reflectance to the surface roughness in different ways.

In semi-empirical inversion method, the “power-law spectra” method was used for generating computer-simulated surfaces. Both slope and offset of the power-law spectrum were used for characterizing the degree of the roughness, assuming random phase angles. However, Weeks et al. (1996) have demonstrated that complicated natural surfaces cannot be fully described by the power-law method with this assumption. Significant differences between the natural and simulated surfaces, defined by the same slope and offset, are introduced by the random-phase assumption. These affect the theoretical relationship of the reflectance to roughness and, therefore, affect the semi-empirical inversion for the surface roughness. In this study, however, this complexity was overlooked. Its effect is not clear and requires further study to understand.

The variability of rock and soil spectra also affects the semi-empirical inversion method. In this study, all twelve rock samples were collected from one site, Grotto Canyon wash, and this severely under-represents the lithologies present in the Death Valley region. This bias in sampling unavoidably affects the inversion results, but the sensitivity of its effectiveness is very complicated and has not been explored.

Uncertainty of reflectance response to the changes of surface types from vegetation, to sand, or soil may be high for the semi-empirical inversion method. This may limit the reliability with which the reflectance may be calculated for simulated surfaces, and, thus how well the power-law method describes various surfaces. However, vegetation is sparse (5-10%) in the Death Valley study area, which minimizes complexity from that quarter. Obviously, for densely vegetated forest areas, this source of uncertainty must be addressed in detail if the semi-empirical inversion is to be applied.

In general, inversions for roughness parameters only coarsely resolve surface roughnesses. The resolution of the roughness estimation for all inversion methods appears to be limited to major geological units. This results from the inherent indeterminacy of inversion problems. There are two reasons for the limited roughness resolution: 1. the remote-sensing data resolution (30-m), and 2. a certain amount of spectral information in foreground limits the accuracy with which the FIR filter is chosen, resulting in loss of separation of background and foreground.

The difficulty of model validation is a common problem in remote sensing, especially for the surface roughness, because the ground truth for roughness is difficult to measure using current techniques. Some techniques used in the field include close-up stereophotography and direct measurement of topography at the cm scale with pin profilers. However, all field measurements of roughness are at much finer resolution than Landsat images, so many intermediate-scale features are not accounted for. Field measurement is also labor-intensive, so that sufficient data to bridge these scales are hard to acquire. Thus, it is necessary to validate the inversion models using available ground-truth data, while remembering that this effort will necessarily be incomplete.

As discussed above, some ambiguities remain in the semi-empirical inversion method because of background/foreground blurring due to spectral variation mimicking the roughness, and due to limitations of the method itself. Several techniques can be used to reduce these ambiguities. "Extended-spectral" remote sensing can provide roughness estimates from different viewpoints, based on different physical light/surface interactions: thermal infrared for roughness and emissivity, microwave radar for roughness and dielectric constant. Furthermore, improvement may result if images taken at different illumination angles are used. Thus, the uncertainty of inversion of NIR images could be reduced by inversion of several kinds images of the same scene. The joint analysis has been suggested by Weeks et al. (1996).

CONCLUSIONS

1. In this study, a new, semi-empirical roughness inversion method was developed based on the FBA model to estimate surface roughnesses from Landsat TM images. The basic element of the FBA inversion is the definition of a finite impulse response (FIR) filter using training data. The FIR filter for the semi-empirical inversion is optimized by using the theoretical relationship of reflectance to surface roughness and a surface-material spectral library.
2. The theoretical relationship was calculated using a radiosity model to derive the response of reflectance to the surface roughness. Mathematically, a series of computer-simulated surfaces were defined from two input parameters (slope and offset) describing the power-law spectra of surface roughness, assuming random phase angles. The reflectance response predominately depends on the offset term. Therefore, the correlation to roughness may be defined by the offset term alone. The spectral library was constructed from samples collected in Death Valley, all from Grotto Canyon.
3. The semi-empirical inversion model has been applied to a Landsat TM image of Death Valley. The roughness results have been verified by field roughness measurements and geological knowledge of this area. Regression of the estimated data to field measurement gives correlation coefficients of $R^2 > 0.7$.
4. Comparisons were made with three other inversion methods: the field-data method, the image-data method, and the shade-image method. For the field data sites alone, the field-data method is the best with $R^2 = 0.94$, but for other areas, the semi-empirical inversion method has the highest overall accuracy. There are two important advantages of the semi-empirical inversion. One is the extendibility of the model, which means the inversion is good not only for training sites, but also for other areas. The other advantage is that inversion results are stable (or repeatable). Once the FIR filter is obtained, the estimate of roughness for the same TM image is uniquely determined, subject only to measurement errors in the image to be inverted.

5. The estimation accuracy in the semi-empirical inversion model is due to two major factors: the sensitivity of reflectance to the accuracy of the simulated natural surfaces; and the sensitivity of FIR filter to the variation of the surface types. These two factors are the most important for the semi-empirical inversion method, and have not been explored in detail in this study. Future work on the semi-empirical inversion model is required to do so.

CHAPTER 5: TOPOGRAPHIC CORRECTION OF A TM IMAGE USING THE CANOPY PHOTOMETRIC FUNCTION

INTRODUCTION

The classification and monitoring of mountainous forest is important to the management and protection of forest resources. Detection of change in forests is of even more significance for studies of land use, forest management, climate monitoring, and other environmental issues (Anderson, 1977; Ingram et al., 1981; Singh, 1989; Collins and Woodcock, 1996). Remotely sensed images are potentially common powerful tools in studies of change. However, the use of remotely sensed data in rugged terrain can be hindered by variations in illumination and reflection geometry caused by different slope angles and orientations (Civco, 1989). Images acquired by high-resolution sensors such as the Landsat Thematic Mapper (TM) and the SPOT are particularly affected by these problems (Leprieur et al., 1988), with the result that topographic shading and shadowing mimics unresolved or subpixel shadowing from and in the trees themselves (Mustard and Pieters, 1987; Itten and Meyer, 1993; Schaaf and Strahler, 1993; Schaaf et al., 1994). Yet, it is this subpixel darkening due to the forest canopy that is a major key in forest mapping.

Various topographic correction models have been developed and used to remove slope effects from images (Civco, 1989). Most conventional topographic corrections have used simplified photometric functions to characterize the bi-directional reflectance distribution function (BRDF) of natural surfaces: examples include the simple cosine function, or Lambert "law" (Hall-Konyves, 1987; Jones et al., 1988; Kawata et al., 1988; Meyer et al., 1993), the Minnaert law (Smith et al., 1980), and their modifications (Teillet et al., 1982). For many natural surfaces, especially including vegetation canopies, these models correct for topographic effects poorly, causing under- and/or over-correction,

basically because they are over-simplified and/or not physically based (Kriebel, 1978; Lee and Kaufman, 1986; Johnson, 1994). A model based on characteristics of unresolved subpixel scene structure, called SCS correction (sun-canopy-sensor) by Gu and Gillespie (1997), is tuned for forested slopes. This is because the SCS model accounts for the distinctive geometric feature of trees: the independence of tree orientation and topographic slope. The SCS model is a step closer to characterizing the BRDF than other methods for forest at least, but its accuracy is limited by variability in the shape and spacing of the trees.

The attempt to define adequate BRDFs for vegetation canopies has led to the development of forward models of radiation scattering (Li and Strahler, 1985; Liang and Strahler, 1993). Li and Strahler (1985) developed a "Geometric-Optic" canopy model based on the mutual shadowing among trees. This model has been used to study the BRDF of canopies and the effects of terrain slope (Li and Strahler, 1986; Schaaf and Strahler, 1993). However, multiple scattering has not been accounted for in the model, even though it has been shown to be important in rough terrain (Shoshany, 1989; Li et al., 1996) and, therefore, in forest canopies. Thus, the radiosity model, which accounts for multiple scattering, is necessary for calculating accurate BRDFs.

As a function of sun-surface-sensor geometry, the BRDF describes the directional reflectance properties of a surface. Much research with forward models (Suits, 1972; Norman, 1984; Smith et al, 1984; Reyna and Badhwar, 1985) and in-situ field measurements (Bauer et al., 1986; Deering, 1989; Jackson et al., 1990; Jon-Ranson et al., 1994) has shown that BRDFs for realistic rough surfaces may be anisotropic, or not ideally diffuse (Lambertian). Shaaf et al. (1994) has recently demonstrated that, for forests, BRDFs vary not only with canopy type, but also with the terrain slope and aspect. The geotropism of trees, which has been pointed out and used in topographic correction by Gu and Gillespie (1997), determines the dependency of surface structure and its BRDF on the terrain slope. In order to characterize the surface photometric function properly,

the BRDF should be calculated for given sun-surface-sensor geometries and the terrain slope and aspect.

In this study, in order to correct the topographic effect on vegetated terrain in TM images, the BRDF is calculated for each image using the radiosity model. A canopy function (CF) as a special case of a BRDF is calculated with fixed viewing angle (nadir looking) and varying terrain slope. This case is feasible only for images like Landsat images, which have been acquired with a narrow range of viewing angles and sun directions, so that the CF is effectively a function only of terrain slope, s (or local incidence angle τ), and slope orientation (azimuth angle), z . To simulate the forest canopy, I designed a “virtual” tree of simple shape consisting of the cone-shaped crown of a conifer. The CF is then built for a surface consisting of these trees having specified sizes and spacing, and viewed under a given illumination geometry, all for various topographic slopes and aspects. Terrain correction using these CFs has been tested on Landsat TM image subsets in Bluff Creek region, and the results have been compared with those of three previous models: cosine correction, Minnaert correction, and sun-canopy-sensor correction.

RADIOSITY MODEL FOR CALCULATING THE CANOPY FUNCTION (CF)

CF TOPOGRAPHIC CORRECTION MODEL

The CF topographic correction model can be derived from the radiosity model (equation 15 of Chapter 1) with some simple modifications. By definition, the surface reflectance r_i is the ratio of radiosity (B) and irradiance (I_{rr}): $r_i = B / I_{rr}$. The reflectance is normalized radiance over a rough surface near the ground surface, which is affected by local slope and azimuth angles. From the equation 15 of Chapter 1, the surface reflectivity can be solved by

$$\rho_i = \frac{r_i}{\cos(\tau_i) + F_A + \sum_{j=1}^n r_j * F_{i,j}} \quad (1)$$

where $F_A = A_{dw}/I_{rr}$ in percentage.

The equation 1 is actually a cosine correction function adjusted for sky light and multiple scattering, all for an intrinsically Lambertian surface. Since reflectance of the forest canopy is characterized by the BRDF, equation 1 becomes the CF correction model if $\cos(\tau_i)$ is replaced by $CF(\tau_i, z)$, the generalized function. The corrected reflectivity thus is

$$\rho_i = \frac{r_i}{CF(\tau_i, z) + F_A + \sum_{j=1}^n r_j * F_{i,j}} \quad (2)$$

Note that the MS term in equation 2 is still based on the Lambertian assumption. With the substitution of $CF(\tau_i, z)$, the calculation of the MS term is no longer accurate but merely an approximation. However, this approximation may be sufficient enough for describing the diffuse component in rugged terrain surfaces, because there exists some degree of randomness of terrain slopes and some Lambertian component of the scattering from a vegetation canopy. This claim is supported in a later section (results section) on topographic correction with MS considered.

Using equation 2 requires accurate image calibration to convert the measured radiance (DN) to canopy-surface reflectance (ρ). An incorrectly calibrated image will introduce errors into the topographic correction, especially for poorly illuminated or shadowed areas, due to a high signal/noise ratio there.

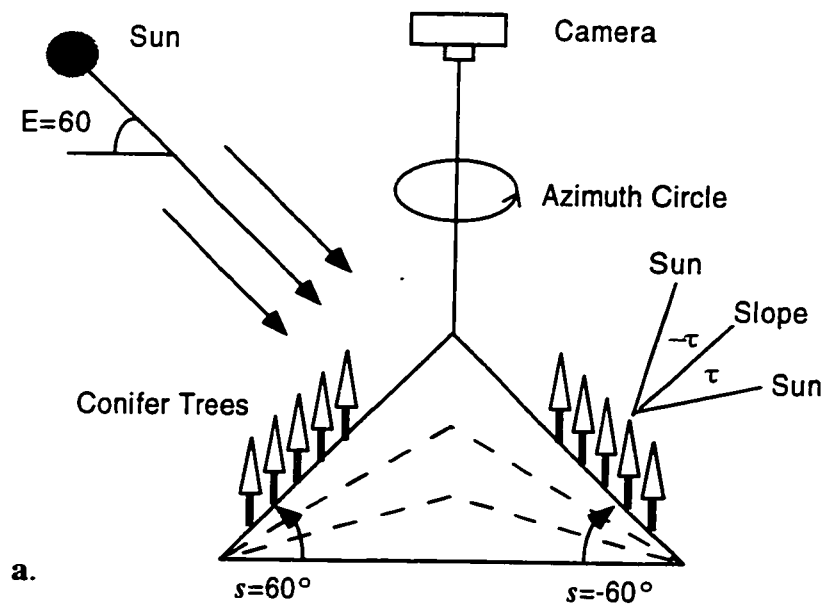
For application to uncalibrated data, the CF correction model (equation 2) has been further modified by the substitution of calibration coefficients and uncalibrated measurement (DN) for the reflectance. The r term can be replaced by the DN using empirical line calibration method (Roberts et al. 1990; 1993; Farrand et al., 1994). Its simple form is; $DN = g * r + o$, where g and o are the coefficients of the empirical line. Thus, the modified CF correction becomes

$$\rho_i = (DN_i - o) / g \left/ CF(\tau_i, z_i) + F_A + \sum_{j=1}^n (DN_j - o) / g * F_{ij} \right. \quad (3)$$

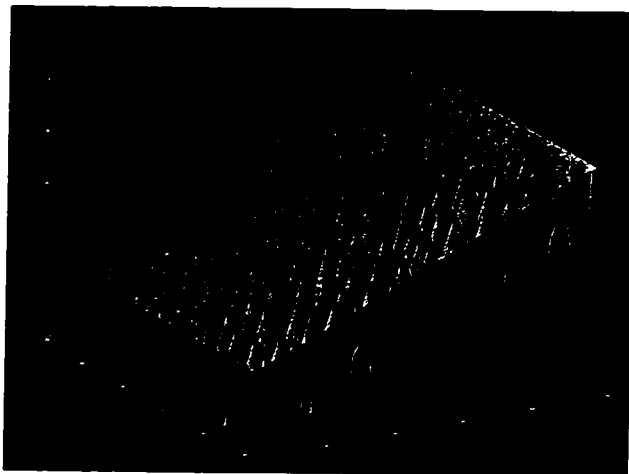
Because the calculation time of the MS term at the pixel scale increases quadratically with the size of the image array, it is the major time-consuming task in running the model. The effect of the MS term for high sun angles, at least, are relatively small (less than 20% area with > 5% MS_R , from Chapter 2) and, in the interest of economy, the simplified CF topographic correction model ignores them. Thus, the modified correction becomes

$$g\rho_i = \tilde{DN} / CF(\tau_i, z_i) + F_A \quad (4)$$

where $\tilde{DN} = DN - o$, and the offset term o includes sky irradiance and instrumental effects. In this equation, a preliminary calibration is required to remove the offset term with an approximation method. In this study, I have simply selected the DNs from lakes or resolved streams, and/or minimum values in the Landsat image, to approximate the offset term. The slope coefficient is not calibrated in this preliminary calibration. The F_A is another term which has to be estimated. The correction will be affected by the estimation of F_A . Detailed discussion on the estimation is in a later section. The images corrected using equation 4 will be in terms of gp .



a.



b.

Figure 31. The canopy-surface model diagram. a). The geometry and parameters of the canopy surface (E sun elevation angle, s terrain slope, $-\tau$ local incidence angle). b). The simulated canopy surface image on a 30° slope (trees are randomly distributed with same height and size). The “box” surrounding the plot is a device to approximate MS from neighboring plots in an infinite forest. The vertical patterns in the box walls are the insides of trees where they overlap the edge of the plot.

CANOPY SURFACE MODELS

A simple canopy surface model was specified by a high-resolution DTM constructed from simple geometric shapes representing individual trees. Conifer forests in the Pacific Northwest were simulated in this study. Each tree is represented by a solid, opaque cone on a pole. A group of these “trees” are distributed randomly on a flat surface (but with settable dip) such that they may touch but not overlap (Figure 31).

The simulated canopy surface is subdivided into raster elements. To ensure accuracy, these elements must be much smaller than a tree diameter (e.g., < 10%) so that the calculated radiosities are well approximated everywhere. The apparent reflectance from this canopy model is the average of reflectance received at the sensor from all the elements. I have chosen 100x100 pixels as the size of the canopy surface model by considering the image resolution and computation time. In the image, each tree comprises about 10 pixels.

For this preliminary study, additional simplifying assumptions have been made:

1. all the surface elements are perfectly diffuse (Lambertian surface), including the tree crowns, trunks and the background or substrate.
2. all the trees are the same size, including the height and the ratio of crown to trunk height.
3. the trees are opaque.
4. the canopy model surface is isotropic.

From the remote-sensing viewpoint, an important characteristic of a forest is that the trees are geotropic: their trunks are vertical regardless of the slope of the hillside. That makes the BRDF of vegetated surfaces distinct from those of soil and rock surfaces, because much of the radiative interaction is independent of topographic slope. As an analogy, the changes of canopy surface structure with topographic slope resemble a deck

of cards being sheared: as the slope increases, more tree surface is exposed, although the trees themselves are unchanged.

To minimize edge effects in the small (100x100 pixel) canopy model, the model was surrounded by opaque walls with the same height to the trees. This simulates extending the forest by allowing no illumination to reach the sides of the model. When the sun illumination angle equals the slope angle of back-facing hillsides, there is no light on the canopy surface and the reflectance of the surface is zero.

All the surfaces of tree crowns and trunks, and of the background, are assumed to be ideally diffuse or Lambertian. However, at the pixel scale the canopy surface is no longer Lambertian because of canopy structure. The CF, calculated from the canopy model, represents this anisotropy.

CFS FOR LANDSAT TM IMAGES

TEST SITES

Two Landsat TM images of the same area within the Bluff Creek watershed in the Pacific Northwest were chosen as test images for this study: one ("Image 84") was acquired on August 31, 1984, with 60.8° sun elevation angle (E) and 123.6° azimuth angle; and the other ("Image 90") was acquired on November 8, 1990, with 37.5° sun elevation angle and 145.0° azimuth angle. These two images are representative of most Landsat images acquired with middle to high sun elevations in temperate regions.

The test sites are 300x300 pixels in size, with 30-m resolution (9x9 km²). They are centered at 123°46' latitude and 41°50' longitude. The test sites were selected in high rugged areas supporting old-growth conifer forest (Douglas fir). There are several small patches of clearcut and snow, together accounting for less than 10% of the test sites. The

old-growth canopy closure is about 70-80%, as estimated by our own field measurements in 1996.

At the scale of the DEM, most slopes within the test site are under 50° , and average 20° - 30° . Because of this, the local incidence angles (τ) for Image 84 mostly fall between 0° and 70° ($0.35 \leq \cos(\tau) \leq 1.0$), but extend to their full range (0° - 90°) in Image 90. The sun elevation angle controls the fraction of the test area shadowed or heavily shaded.

The simulated canopy surface model for this test site was made of 115 trees. Each tree is 30 pixels tall, 10 pixels in diameter, and the crown-to-height ratio is 67%. The apex angle of the tree crowns is 25° .

CFS FOR THE TWO IMAGES

The canopy functions for the two images were calculated using equation 1 within the range of -60° (shaded side) to 60° (sunlit side) slope angle, at increment of 10° (Figure 31). Because of the isotropy of the canopy model and the symmetry of the sunlit and shaded sides, the range of 0° to 90° azimuth angle (increment, 10°) will cover all slope orientations (0° - 360°). Because of calculations of the MS at the subpixel scale, building the CF using equation 1 is the major cost of running the CF-correction model. The 13 slope and 10 azimuth-angle values required a total of 130 executions of the model algorithm, each taking about 90 minutes using a DEC Alpha-3000 station with a 276-MHz processor. Although the expensive computation is a major drawback for setting up the CF correction model, once the CF is known for a given sun elevation angle it can be used for all images that have the same illumination angle.

Figure 32 shows a 3-D plot of the CFs for Image 90 relating CF to the slope, s , and the azimuth angles, z . In the principal plane, where the slope azimuth is zero, the CF has the maximum sensitivity to slope angle. Perpendicular to the principal plane where the

azimuth is 90° , the curve is flat, indicating that the reflectance is largely independent of the slope at this illumination direction. Other CF features will be compared with equivalent cosine correction features in the next section.

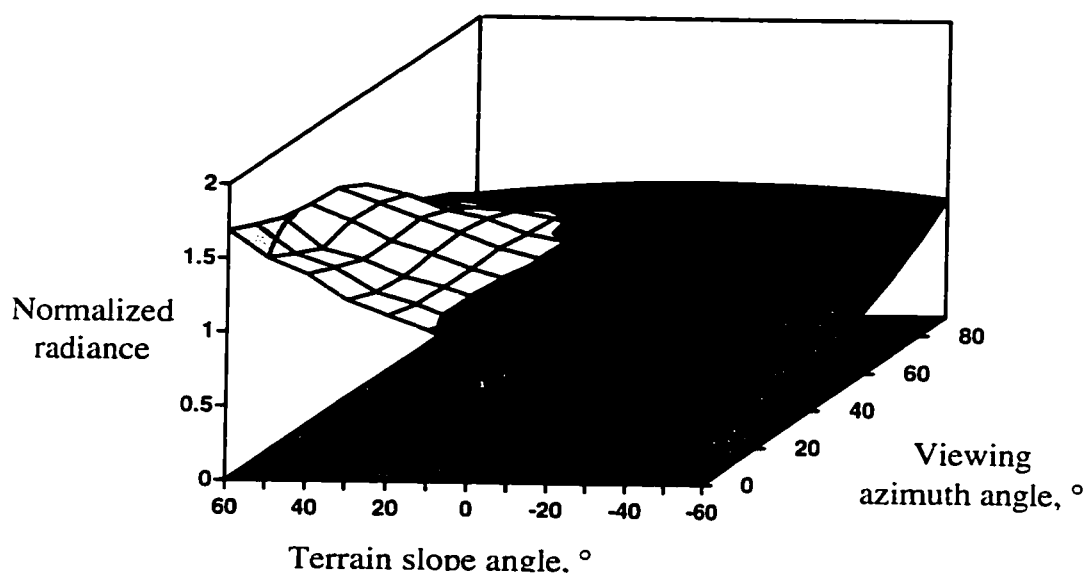


Figure 32. The canopy function of topographic correction is calculated for Image 90 (the Landsat image acquired on the November 8, 1990, with 37.5° sun elevation angle and 145° azimuth angle), when $\rho = 25\%$. Normalized radiance refers to the radiosity is normalized by the single scattering value at $\tau = 0^\circ$ ($\alpha = 30^\circ$). Color shows zones of radiance.

The canopy surfaces used in this study are rough, as indicated by the input aspect ratio. Deep and narrow holes between trees cause a large amount of shadowing at all but nearly vertical sun elevation angle. They also generate large amounts of multiple scattering, which increase with the intrinsic reflectivity (see Chapter 2). Thus, the CFs depended strongly on the surface reflectivity. In order to bracket the CFs for a single multispectral Landsat image (with different reflectivities at the different wavelengths), a series of CFs was calculated for surface reflectivities from 0% to 55% at 5% increments

(Figure 33). The topographic correction for each band will require a different CF correction model.

In the preliminary study, I have assume constant ρ for all components of the canopy surface. The difference of the CF for actual reflectivity distribution patterns (crown, trunks, substrate) will be discussed in a later section (discussion section).

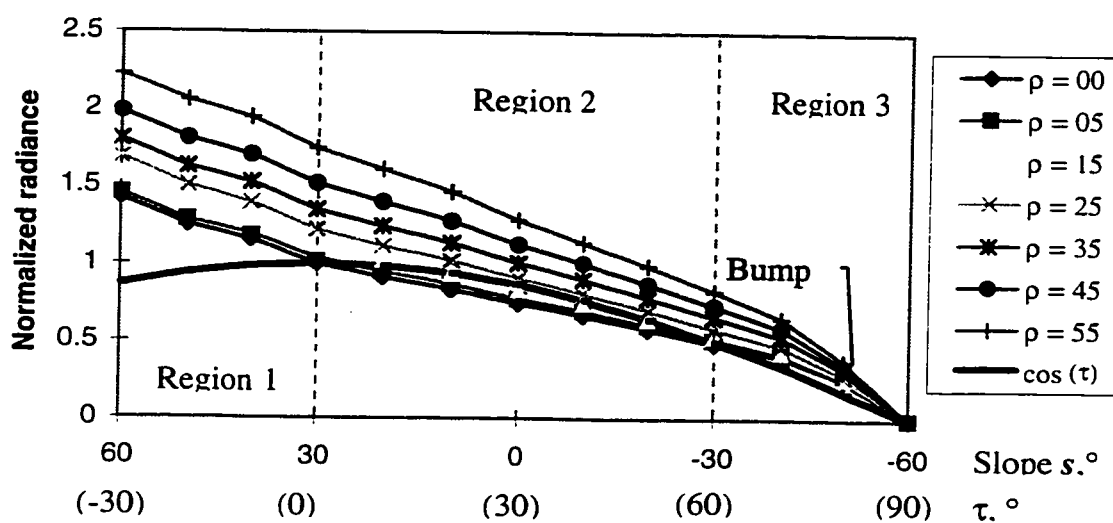


Figure 33. The canopy functions (CFs) of Image 84 for surface reflectivities from $\rho = 0\%$ to 55% in the principle plane, compared with the cosine curve of the local incidence angle. Region 1 is the negative-angle range ($\tau < 0^\circ$). Region 2 is the middle-angle range ($0^\circ \leq \tau \leq 60^\circ$). Region 3 is the high-angle range ($60^\circ \leq \tau \leq 90^\circ$).

CHARACTERISTICS OF THE CF

When compared to the cosine function, the CF shows three distinct characteristics (Figure 33). The three features directly relate to a three ranges of the local incidence angle: a negative-angle region, a low-middle-angle region, and a high-angle region.

1. The negative-angle range ($\tau < 0$) includes all negative values of the local incidence angle (on the camera side of surface normal). Such values are formed on the

upper side of the surface normal (Figure 31a). The CFs show a continuous linear increase as the surface slope increases from the zero incidence angle (or $s \geq 30^\circ$), whereas the cosine function is symmetrical about the surface normal ($\tau = 0^\circ$). This linear feature is caused by the increasing area of canopy exposed to sun light as the slope increases. Inaccurate correction caused by using the cosine function becomes worse in this region. Fortunately, data in this region are not common in most Landsat images, because they require both high terrain slopes and a high sun elevation angle. For example, in order for τ to be negative, an image with 60° sun elevation angle requires that the slopes must be greater than 30° .

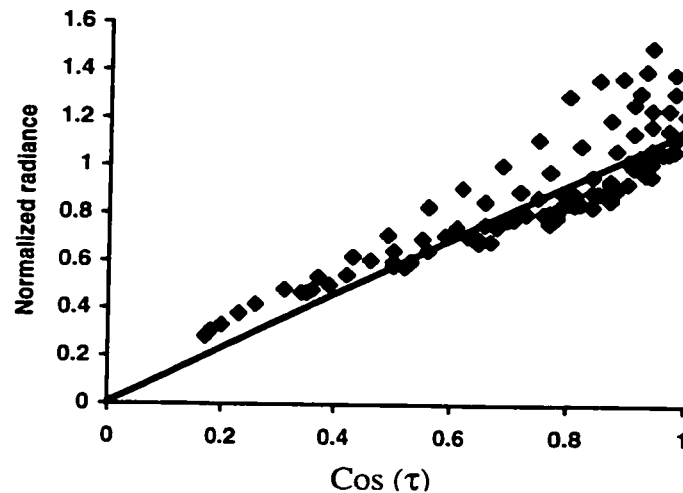


Figure 34. The normalized radiance data calculated from simulated canopy surfaces related to the cosine of the local incidence angle for all sun-surface-camera geometries. It is similar to Figure 35 by projecting all the data on to the principle plane in the range $0 \leq \cos(\tau) \leq 1$. The scatter of the data near $\cos(\tau) = 1$ is caused by the high radiance in the negative angle range. The solid line is the linear curve for a flat Lambertian surface. The terrain slopes are from -50° to 50° . Surface reflectivity is 25%. The data is normalized to the single-scattering radiance value for $\tau = 0^\circ$.

This feature of the CF causes the normalized radiances to scatter when plotted against $\cos(\tau)$, as shown in Figure 34. Unlike Figure 32, Figure 34 shows all data,

regardless slope azimuth. Figure 34 was constructed simply by projecting a 3-D plot of Figure 32 onto a 2-D plot. Because the cosine of the incidence angle has the same value for both positive and negative incidence angles, the projected data are “folded” about $\cos(\tau_i)=1$, and it is this that causes the vertical scattering on the right-hand side of Figure 34. The most scatter occurs near $\cos(\tau_i) = 1$. However, this indicates that the scattering of real image data may not be entirely due to measurement errors and the natural variability within scene classes, as interpreted in some studies; instead, it is likely caused by the structure of the trees themselves.

1. The middle-angle region refers to the range of $0^\circ \leq \tau < 60^\circ$ (or $30^\circ \geq s \geq -30^\circ$). In this region, the CFs are linear, similar to the cosine curve, but with small slope differences. Within this region the surface is essentially Lambertian. As the slope varies, the reflectance of the canopy surface also varies, and is given by the cosine of the local incidence angle.

The Lambertian quality of forest canopies at $0^\circ \leq \tau < 60^\circ$ is significant in topographic correction, because most Landsat images are acquired at a high sun elevation angle and have terrain slopes of less than 20° , such that most data fall within this range of incidence angles. Under these conditions, the CF model is nearly Lambertian, and there is little to be gained by using other than simple cosine correction. In a later section, I will demonstrate this similarity of correction results for different models.

2. The high-angle range is $60^\circ \leq \tau \leq 90^\circ$ (or $-30^\circ \geq s \geq -60^\circ$). Each CF curve in this range has a small “bump,” a convex curve, with higher values than the cosine curve, indicating that there is a stronger backscattering component from a canopy surface than from a Lambertian surface.

The sizes of the bumps are controlled by the tree spacing, surface structure (shape of the tree), and the surface reflectivity. These bumps play a critical role in topographic correction, especially for images illuminated with a low sun elevation angle, in which many areas are shaded or shadowed (in the high-angle range). The problems caused by

over-correction in most other topographic correction models are avoided by this stronger backscattering feature in the CF.

TOPOGRAPHIC CORRECTION OF A LANDSAT TM IMAGE

Image 84 was used to exercise the CF topographic-correction model. The CFs built for the 60° sun elevation angle were used in equation 2, together with a variation of surface reflectivities from 0%-55%. The calculated CFs are shown in Figure 33. Prior to the correction, some image preprocessing was required, as described below.

IMAGE PREPROCESSING

The first step prior to topographic correction was to register the TM image to the DTM. The registration was done using the 'PICREG' function in IDL image-processing software (which was adapted by Steven Cothorn at UW from a VICAR program at JPL). The misregistration errors have great impact on the analysis of image data among the different images and other data maps (Townshend et al., 1992). As discussed in Chapter 3, the accuracy of registration (geometric errors) is a critical factor to the radiosity calculation for the CF. The errors caused by the registration will greatly affect the topographic correction.

The second step is to calibrate the image. Using equation 2 and accounting for MS requires full calibration of the image. The empirical-line method is to obtain a linear regression for the image radiances or DN to the reflectance measured in the laboratory, for a particular surface material in the image. In this study, I have chosen a small lake and a gravel bar as anchor points. However, this simple calibration contains some errors caused by variation or deviation between the laboratory and TM data of these two anchor points. The variation for water could be caused by sky light, secondary illumination from trees, and sediment in the lake. The variation for the gravel bar could be caused by its rough surface. The errors in the calibrated image in turn affect the topographic correction

results. These errors are minimized if the sun elevation angle is high, because the signal/noise ratio is reduced.

Using equation 4 without MS requires a preliminary calibration of the image. This was done by simply removing the offset term caused in part by the upwelling sky light. The offset terms for all bands were determined based on the water spectrum measured in the TM image and/or the minimum DNs in the image. The offset coefficients were determined by assuming that the spectrum of pure water has zero reflectances in TM image bands 3, 4, and 5, and that the minimum DNs in the image correspond to these values. For Image 84, the offset terms were found to be 4 DN for band 3, 2 DN for band 4, and 0 DN for band 5.

DOWNWELLING SKY ILLUMINATION AND SURFACE REFLECTIVITIES EFFECTS TO THE CF

Downwelling sky illumination (F_A) and surface reflectivity (ρ) have complementary influence on the magnitude of the CF correction. In equations 2 and 4, F_A reduce the CF correction by simply adding a constant offset to the CF; ρ increases the CF correction by reducing the offset term due to multiple scattering, as shown in Figure 34. The complementary effects of the two terms will produce same correction results for different combination of the two terms. A best topographic correction, which has minimum dependency on the terrain slope after correction (discussed in a next section), is not unique to a specific combination of the F_A and the ρ , if only the data dependency on slope is considered.

A good topographic correction, defined by a particular pair of F_A and ρ , must be physically meaningful for a particular TM image. In other words, F_A and ρ must vary only in a limited range. For example, F_A on a clear day is usually near ~10% in TM band 3, ~5% in TM band 4, and ~0% in TM band 5; and ρ for vegetation is ~5% for TM band 3, ~40% for TM band 4, and ~25% for TM band 5. These values for F_A and ρ can be

derived from laboratory spectrum of vegetation and the illumination geometry of the TM image (Gao and Goetz, 1994). In order to achieve the best topographic correction results with the proper set of the two complementary parameters, several pairs of F_A and ρ are used in calculating the correction (Table 5).

Table 5. Slopes of the regression line of the TM image data for all combinations of F_A and ρ

ρ	Band 3			Band 4			Band 5		
	$F_A = 6$	$F_A = 8$	$F_A = 10$	$F_A = 2$	$F_A = 3$	$F_A = 4$	$F_A = 0$	$F_A = 1$	$F_A = 2$
00%	0.017	0.010	0.004						
05%	0.016	0.010	0.005				0.0003	-0.008	-0.016
15%	0.016	0.011	0.006	-0.012	-0.024	-0.035	0.001	-0.006	-0.013
25%	0.017	0.012	0.008	-0.006	-0.016	-0.026	0.002	-0.003	-0.009
35%				0.003	-0.006	-0.014	0.006	0.001	-0.003
45%				0.019	0.012	0.005			0.006
55%				0.04	0.034	0.028			

Correction results were evaluated by correlating the corrected image to the local incidence angle. Before correction, the image data were strongly affected by the terrain slopes. After correction, this dependency should be removed. Hence, a statistical regression line was fitted to the scatter plot of the image data before and after correction to the local incidence angle. A zero slope of the line would indicate independence of the image data to slope.

TOPOGRAPHIC CORRECTION WITHOUT MULTIPLE-SCATTERING

The topographic correction was first applied to the test site in Image 84 using equation 4 and ignoring MS at the DTM scale (pixel scale). The best possible combinations of F_A and ρ for each band (i.e., yielding zero correlation of corrected image data to terrain slope) is given as a bold number in Table 5.

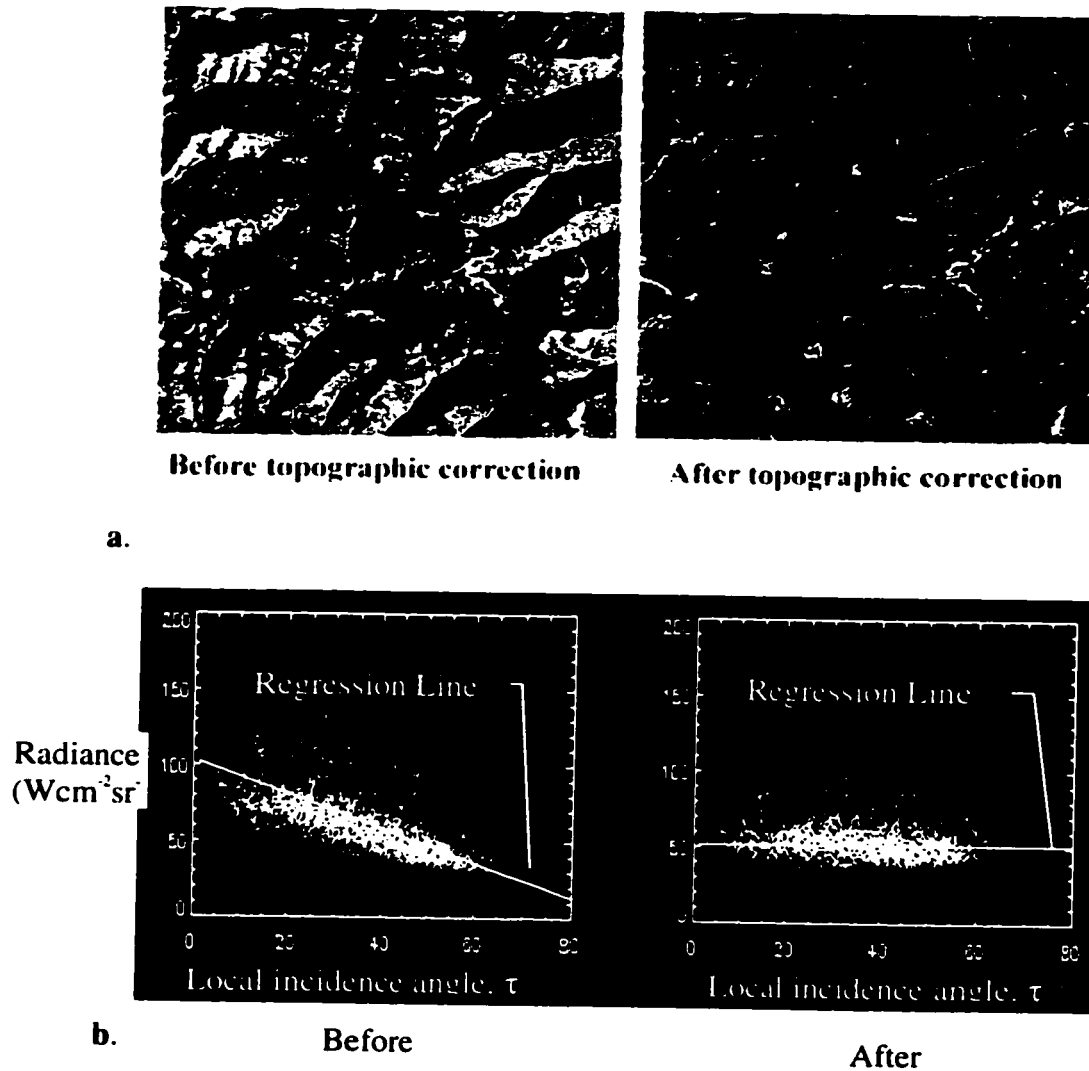


Figure 35. Comparison of the topographic correction for Image 84 using CFs. a). Color composite of three bands: 3 (green), 4 (blue), and 5 (red). b). The data scatter plots before and after topographic correction for band 4.

The corrected and uncorrected images are displayed in Figure 35. The major terrain shading features have been removed from the original image (Figure 35a). In general, the corrected image looks flat, even though there remains some shading variation in the shaded sides of hills. These correction errors can be caused by several conditions: inefficient topographic correction, registration error, or high noise/signal ratio in the

shaded slope. From the pattern of the mis-corrected areas, it is most likely caused by the last two factors.

Table 6. Comparisons of the regressions of image data before and after topographic correction using the CFs

Regression line	Band-3		Band-4		Band-5	
	Before	After	Before	After	Before	After
Slope (°)	-0.157	0.005	-0.766	0.012	-0.42	-0.003
Offset (DN)	21.6	18.9	88.4	55	47.8	36.6
Mean (DN)	16	18	60.8	55.6	32.6	36.5
Stdev ¹ (DN)	20	22	21.1	14.7	13.7	13

The comparison has been further evaluated quantitatively by using scatter plots of image data DN vs. local incidence angle (or slope) (Figure 35b). An evaluation of the use of regression lines to fit the scatter plot is given in Table 6. Comparisons of the regression slopes before and after correction show a reduction in the dependency of image data on terrain slope.

The offset, mean and standard deviation (stdev) of the regression line are less important than slope-angle parameter for evaluating the correction. The offset value at $\tau = 0$ indicates the spectral value of the surfaces on which the light incident vertically, and it is close to the mean value of the image data (reflectances) after correction. The standard deviation term describes the scattering of the image data. In general, the smaller the standard deviation, the better the correction.

TOPOGRAPHIC CORRECTION WITH MS

Topographic correction has been improved by compensating for multiple scattering as well as illumination geometry, even though the MS was only approximated by using equation 2. The biggest improvements are in the high-shade and shadow areas. Image

90, with 37.5° sun elevation angle, was used to demonstrate the effect of MS on the topographic correction.

To reduce computing time, the test site was re-sampled to reduce image size to 150x150 pixels, with 60-m resolution. The image was first fully calibrated using the empirical line method, converting the encoded measured radiance (DN) to reflectance. The sky illumination and surface reflectivity were selected using the same procedure discussed in the previous section. As an example, band 4 was used comparing corrections with and without MS. The reason is that MS effect in this band is stronger than other band for vegetated surfaces due to high reflectivity (from Chapter 2).

Table 7. Comparisons of the topographic corrections with and without Multiple-Scattering

Regression line Parameters	Image 90 Band-4		
	Before	Without MS	With MS
Slope (°)	0.16	-0.03	-0.002
Offset (DN)	6.8	16.5	14.2
Mean (DN)	15.6	14.7	14.1
Stdev (DN)	5.5	12.3	7.3

Figure 36 and Table 7 show the comparison of the corrections with and without MS in three different ways. First, the scatter plots in Figures 36a and b show less scattering with MS than without MS at low incidence angles. Second, the standard deviation of the corrected reflectances plotted against $\cos(\tau)$ in Figure 36c, shows that the correction without MS reflects more spatial variation and stronger dependency of slope than the correction with MS. Third, the slope of the regression line for the correction with MS is less than it is without MS, as shown in Table 7. However, the over-correction of data, which are scattered far off the main cluster at low incidence angles (Figure 36a), is not totally adjusted by using the radiosity model, as shown in Figure 36b. These overcorrected data were possibly caused by several conditions: MS that has not been

properly predicted by the radiosity model with the assumption of a Lambertian surface; registration errors; and/or calibration errors.

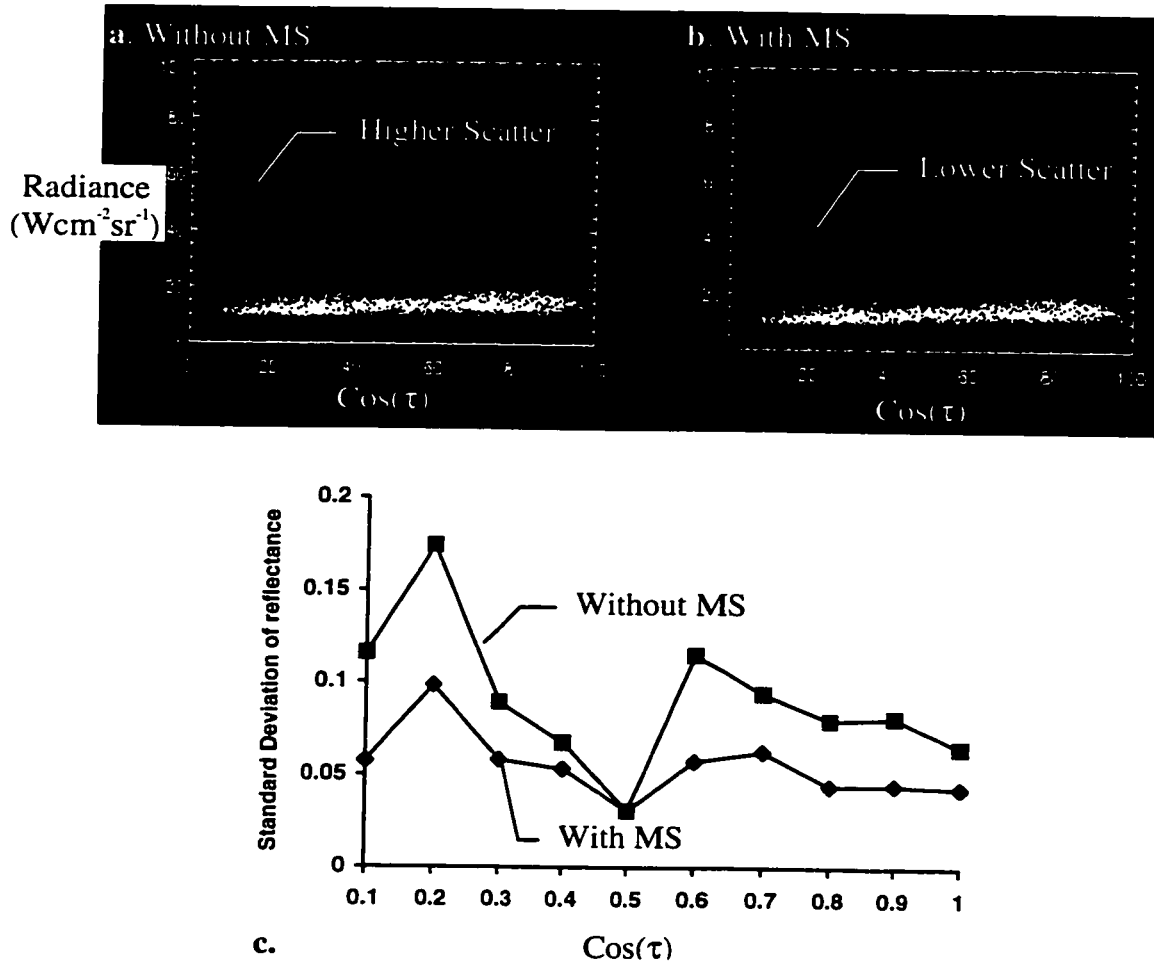


Figure 36. The comparison of topographic correction of Image 84 with and without MS, using CFs. a). A scatter plot of CF correction without MS, and b). The scatter plot of CF correction with MS. Both plots are resampled by 1/7 for clearer display. c). The comparison of the standard deviations of the two corrected reflectances.

DISCUSSION

All the topographic corrections presented above were made assuming that the preliminary and/or full image calibrations were accurate. If the offset term in the

calibration is inaccurate, the CF topographic corrections will be affected, causing the image data to be over- or under-corrected. The magnitude of effects is, however, also modified by the combinations of both downwelling atmospheric scattering F_A and surface reflectivity ρ , because F_A increases the base level of the CF by increasing irradiance to every pixel, whereas ρ reduces the intercept (offset) of the CFs by the increasing the amount of MS (Figure 33). Thus, the three parameters, by controlling the offset term of either the image data or correction functions, have similar effects to the topographic correction. For the same correction results, there is no unique set of values for the three parameters, because increasing one of them can be compensated for by adjusting the other two. Choosing the best combination of the three parameters requires additional information. For example, the reflectivity can be measured from laboratory: atmospheric scattering (up- and down- welling) may be inferred from other images;

The application of the CF correction model to Landsat TM images has been presented in simplified form, relying on several assumptions. However, even though the simplified form of the CF produces reasonable results, its accuracy is still the key factor for obtaining the best correction possible. As discussed earlier, the basic form of the CF is controlled by the canopy structure, but the shape of CF can be modified by many important parameters, including tree shape, tree spacing, surface reflectivity, transmission of light through the tree, and actual reflectivity distribution patterns. Understanding how these parameters affect the CF could enable us to refine the CF corrections.

TREE SHAPE

Two of the most common shapes of trees are approximated by cones (conifers) and ellipsoids (deciduous trees). The different types of trees that compose a forest affect its surface structure and roughness. Conifer trees have a higher aspect ratio (the ratio of tree height to spacing) than the ellipsoidal deciduous trees, and therefore a coniferous forest

has a rougher surface. The surface roughness affects the BRDF of the forest, and thus the CFs for the two types of forest ought to be different.

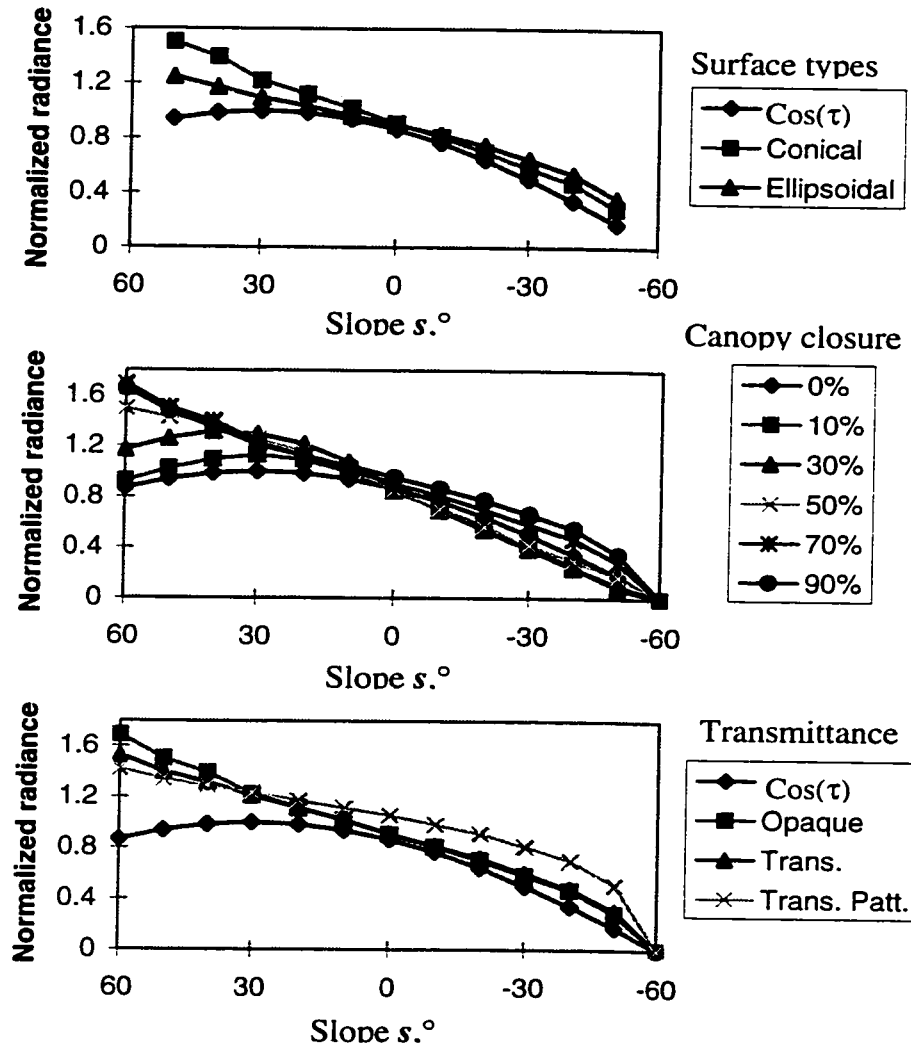


Figure 37. The Canopy Functions (CFs) for various type of canopy surfaces. a). CFs for canopy surfaces made of cone-shape trees (conifer) and ellipsoidal trees, compared with cosine curve. b). CFs for canopy surfaces of different canopy closure, from 0% - 90%. c). Comparisons among the canopies containing opaque trees with $\rho = 25\%$, transmissive trees with $r = 25\%$ ("trans."), trees with a distributed pattern of ρ (crown = 40%, trunk = 5%, and substrate = 25%, "trans. patt."), and cosine curve. Y axis is scaled radiance normalized by the radiance at $\tau = 0^\circ$.

I have designed a deciduous tree model composed of ellipsoid-shaped trees that is otherwise similar to the conifer tree model. In order to compare the two, I have kept all of the other canopy parameters the same in the deciduous forest model and in the conifer forest model. I have calculated CFs for the deciduous forest exactly as reported above for the conifer forest.

The two CFs are compared in the principal plane (the sun-surface-camera plane), as shown in Figure 37a. The two curves have similar shapes except for that the CF of the deciduous tree has smaller slope than that of the coniferous tree. The cause for the difference is quite complicated. Part of it is due to the different amount of MS component predicted by the two surface models. Part may also be caused by the sun-canopy-camera geometry. For example, when the sun elevation angle is fixed, the fraction of the single- and multiple-scattering component for each pixel could be different for the two kinds of canopy surfaces, because the surface exposure areas of the two are different due to their different apex angles. A complicating factor is that the ratio of single scattering to multiple scattering varies with the topographic slope. Additional studies are required to understand in detail how the CFs depend on the canopy-surface structure.

TREE SPACING

The tree spacing is a significant characteristic of the forest model. It is closely related to maturity stage, health status, and fire and logging history (Kleman, 1987; Abuelgasim and Strahler, 1994; Muchoney and Haack, 1994; Olsson, 1994; Syren, 1994). Variation of tree spacing directly affects the shade fraction in the image, and therefore the BRDF (Franklin et al., 1986; Franklin and Strahler, 1988; Franklin and Turner, 1992). The shade fraction (darkness) is mainly controlled by the single scattering and reduced by the multiple scattering (Li et al., 1996). Below, the CFs are compared among various tree

spacings from zero (flat, Lambertian surface) to 90% tree coverage with 15% gaps (Figure 37b).

The major changes of the CFs caused by the tree spacing occur for high ($\sim 70^\circ$) and negative ($0^\circ \geq \tau \geq -30^\circ$) local incidence angles. Under the Lambertian surface assumption, the zero density forest (100% tree spacing) is a flat, perfectly diffuse surface, giving an exact cosine curve response. As the tree coverage (density) increases progressively from 5% to 90%, the reflectance in the high incidence-angle region, initially less than that of the unforested surface, increases to the same (50% cover) and higher values (>50% cover). This is basically because the domination of the shadowed over the directly illuminated forest is reversed when the forest cover is increased to about 60% or more. In negative incidence-angle regions, however, as the forest cover increases the reflectance also increases steadily from cosine curve to a straight line. This is because the exposed area of the trees in this illumination range is proportional to the increase of the tree coverage.

Changing the tree spacing shows an important character of CFs. The size of the “bump” in CFs in the high local incidence angles is strongly influenced by the forest cover: higher cover will cause a bigger bump (Figure 37b). This is significant for forest terrain correction, especially at low sun elevation angles, because most image data will be in the high local incidence angles.

ADJUSTMENT REQUIRED FOR TRANSMISSIVE TREES

In the simple model, I have assumed that the individual trees are opaque. In reality, this is not the case, especially in the NIR spectral region (Roberts, 1991). Light transmitted through the trees, will increase the incident light in shaded areas and, therefore, increase both the single and multiple scattering. Thus, the CFs must be adjusted to accommodate these changes.

Using the same canopy surface model of a stand of conifers, I have examined the sensitivity of the CF to tree transmissivity for two cases: a scene with uniform $\rho = 0.25$ and a scene with variable ρ . For the second case, the energy transmitted through the tree was assumed to decrease exponentially with the path-length of light in the tree. The ρ image was constructed such that ρ for tree crowns was 45%, ρ for tree trunks was 5%, and ρ for substrate was 25%. These two terrain-corrected images are compared to their equivalents corrected with the cosine function, and CF-corrected assuming opaque instead of translucent trees (Figure 37c).

The CF for case 1 (uniform ρ) is almost same as the CF for the opaque-tree model, except it is slightly higher for negative local incidence angles. The CF for case 2, however, shows a strong difference for high local incidence angles. The bigger “bump” formed in high τ region is generated mainly by the high reflectivity of the crown surface.

REFLECTIVITY

The reflectivity of vegetation varies strongly with wavelength, from 5% (near 0.65 μm) to 50% or higher (near 1.2 μm). Thus, the topographic correction for the different bands of a multiple spectral image requires different CFs based on the proper reflectivities. In Chapter 2, it was demonstrated that increasing the surface reflectivity increases the MS in an image. In the result section of this Chapter, the uses of CFs with different ρ for topographic correction in different bands have demonstrated the dependency of the CFs on the reflectivity. The changes of CFs with ρ are mainly caused by the multiple-scattering component.

COMPARISON WITH OTHER METHODS

Many topographic correction models are being used to correct terrain effects in remotely sensed images. Three are representative and are used here for comparison to the CF model: cosine correction (Hall-Konyves, 1987; Jones et al., 1988; Kawata et al., 1988; Meyer et al., 1993), SCS (sun-canopy-sensor) correction (Gu and Gillespie, 1997), and Minnaert correction (Smith et al., 1980) .

COSINE CORRECTION

The cosine correction is the most basic method used for equalizing the illumination variation over rugged surfaces. It accounts for changes in illumination intensity at different illumination angles, for perfectly diffuse reflection. Equation 3 gives the formula of cosine correction for flat Lambertian surface, considering also down-welling sky illumination and multiple scattering. Cosine correction is most appropriate for smooth, unvegetated surfaces.

SCS (SUN-CANOPY-SENSOR) CORRECTION

The SCS model was developed for the topographic correction of vegetated terrain. It is based on the subpixel-scale geometric character of the forest canopy. The trees are geotropic, growing straight up independent of the terrain slope below. This leads to a simple relationship of apparent reflectance of vegetated surface with the terrain slopes and aspects. Differing from most other models, the SCS changes the topographic correction focus from the sun-terrain-sensor geometry to sun-canopy-sensor geometry. The bi-directional reflectance function is formulated as the cosine function of the slopes and the local incidence angle, which is written as

$$\rho = \frac{L \cos s}{\cos \tau} \quad (5)$$

where ρ is the surface reflectivity, L is the radiance, s is the slope angle and τ is the local incidence angle.

MINNAERT CORRECTION

The Minnaert function was originally used to describe reflectance measured in telescopic observations of the moon at different phases. It has been applied to characterize the photometric function of some natural surfaces (Smith et al., 1980; Meyer et al., 1993). It is the modified cosine function of local incidence angle I and exitance angle e , with an empirical exponential coefficient k that varies from surface to surface:

$$\rho = \frac{L}{\cos^k \tau_i \cos^{k-1} e} \quad (6)$$

where the exitance angle e is approximately the slope angle for the nadir-looking Landsat images. The Minnaert constant k is a measure of how closely the scattering is Lambertian; for a Lambertian surface, $k = 1$, and the Minnaert function is reduced to the simple cosine function. For many natural surfaces $k < 1$, the value of k can be found from an image if ρ and the viewing/illumination geometries are known.

COMPARISON OF THE METHODS

In this section, the four topographic correction models are compared for the two Bluff Creek subset images: Image 84 and Image 90. For simplicity the CF models generated in the results section are used here. Parameters are not suitable for any one of the correction models have been eliminated: for example, the MS term is not considered in either the SCS and the Minnaert models, so that it is also eliminated from the CF model. Both Image 84 and Image 90 were corrected only by removing the upwelling sky illumination (path radiance), which is the offset term in empirical-line calibration method. The down-welling sky illumination and the MS component are ignored for all the models.

Band 4 is used for this comparison, because the typically high reflectivity in band 4 provides a wider range of radiance variation with the slope, so comparison among the four methods is more obvious.

The correction models are evaluated on the basis of the distribution of corrected reflectances, plotted against the $\cos(\tau)$. Two critical parameters for the evaluation are the slope of line regressed to the data, and the standard deviation of the data about that line. The best model should produce the smallest slope of the regression line, and the smallest standard deviation of the corrected data across all ranges of τ .

TOPOGRAPHIC CORRECTIONS FOR IMAGE 84

Due to the high sun elevation angle ($E = 60^\circ$), most areas in Image 84 are fully illuminated (where $\tau < 70^\circ$). The corrections using the four models turn out to be similar. Figure 38 displays the scatter plots of the corrected data, and Table 8 lists the statistical parameters for their regressions. Before correction, the image data exhibit a strong correlation to the local incidence angle, and the slope coefficient of the regression line is 0.78. After correction, the regression lines are nearly horizontal, with slope coefficient near zero; -0.035 for CF, 0.065 for SCS, 0.049 for Minnaert, and -0.049 for cosine respectively.

Table 8. Comparisons of four topographic corrections for Image 84

Regression line parameters	Before correction	After correction			
		CF	SCS	Minnaert	Cosine
Slope coef.	0.23	-0.035	0.065	0.049	-0.049
Offset (DN)	53	60	71.1	65.7	83.1
Mean (DN)	60.8	57.2	76.2	69.5	79.3
Stdev (DN)	21.1	15.1	19.7	18.3	20.7

* stdev = standard deviation

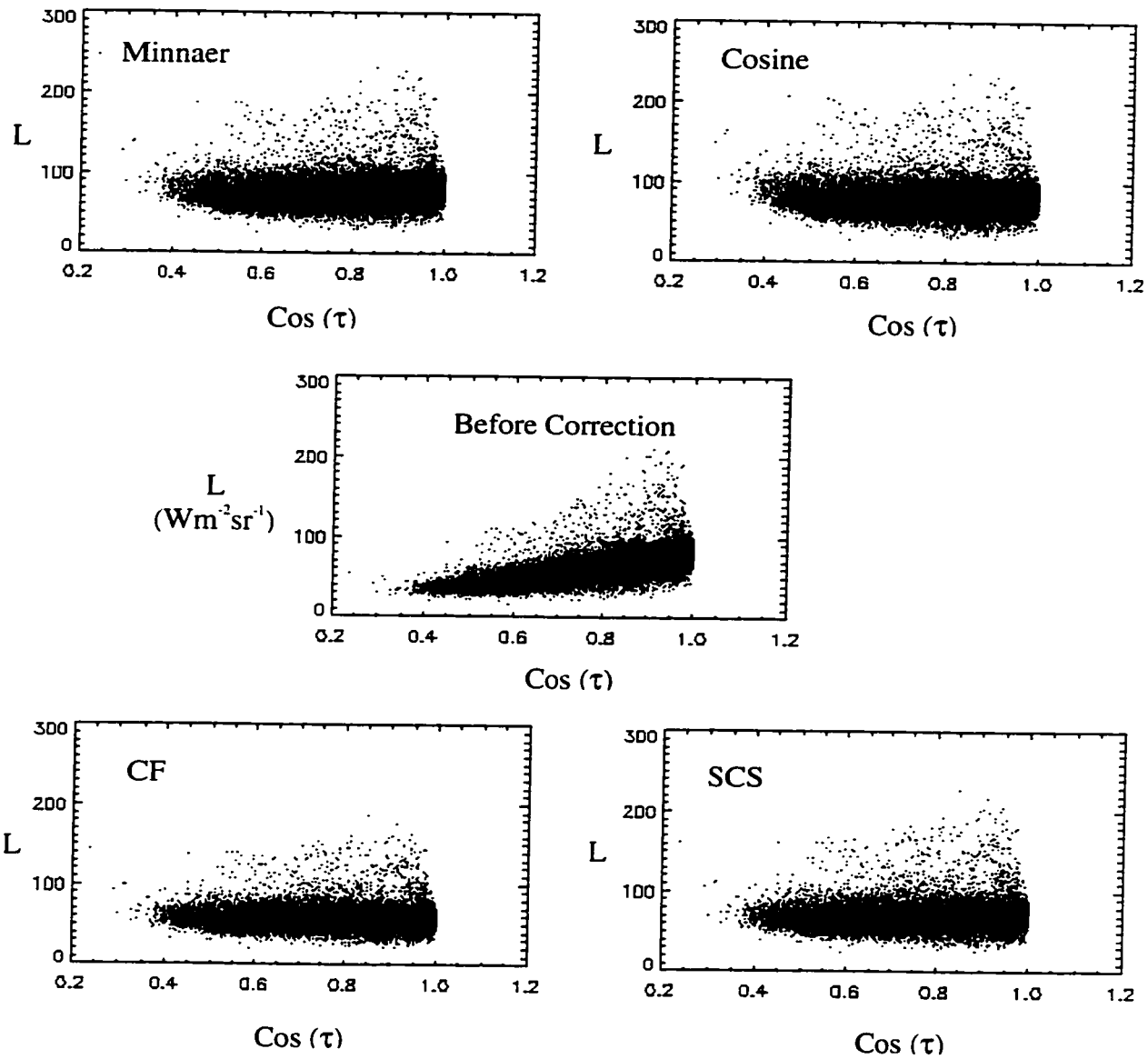


Figure 38. Scatter plots of radiance data ($\text{Wcm}^{-2}\text{sr}^{-1}$) before and after using four different methods of topographic correction on band 4 of Image 84.

Detailed comparison among the four models, however, shows that the CF model gives better results than the other models. The scatter plot for the CF correction shows noticeably less scatter above the regression line. Figure 39 shows the standard deviations

of the corrected radiance distributions against $\cos(\tau)$ for Image 84 (Figure 39a) and Image 90 (Figure 39b). In both Figures 39a and b, the standard deviations of the CF-corrected images are the smallest. They are also relatively stable across the entire range of $\cos(\tau)$. Physically, the constant standard deviation indicates the radiance variation is independent of the terrain slope.

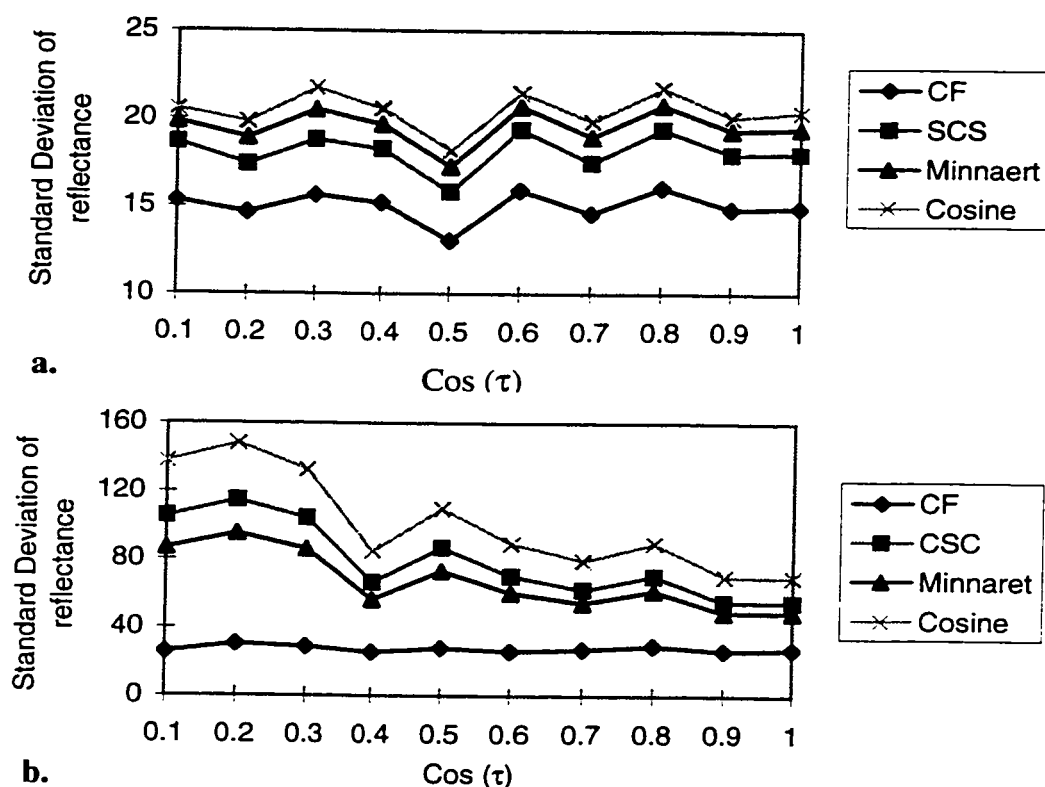


Figure 39. The standard deviations of topographically corrected reflectance about the regression lines in the scatter plots of radiance vs. $\cos(\tau)$. In both diagrams, the CF's have the smallest standard deviation for all local incidence angles. a). Standard deviations for corrected Image 84 from Figure 38. b). Standard deviations for corrected Image 90 from Figure 40.

Certainly, the differences of the four correction models applied to Image 84 are not large enough to determine which model is best, because at high sun elevation angle, the

image data distribution fall in middle region (region 2) of the CF (Figure 33), where all the models have similar linear functions. In order to compare the four models in a broader way, the corrections of the image with a lower sun elevation angle are considered and compared in the next section.

TOPOGRAPHIC CORRECTIONS FOR IMAGE 90

When the sun elevation angle changes from 60° to 40°, many areas in the image fall into high-shade regions, where the local incidence angle τ is high. At these angles, the topographic corrections of the four models for Image 90 show quite different results (Figure 40). The cosine correction causes the worst over-correction in the high-shade regions. For the Minnaert, SCS and CF models, the over-correction is progressively reduced. Clearly, the CF model performs the best terrain correction for the low-sun Image 90.

Table 9. Comparisons of four topographic corrections for Image 90

Regression line Parameters	Before Correction	After Correction			
		CF	SCS	Minnaert	Cosine
Slope coef.	-0.5	0.11	0.29	0.42	0.53
Offset (DN)	77	76.6	120.4	144.8	175.1
Mean (DN)	54.6	58.6	74.1	76.5	89.3
Stdev *(DN)	17.6	31.3	407.2	755.6	955.1

* stdev = standard deviation.

The slope and standard deviation of the linear regression for the CF are far smaller than for the other models (Table 9). The distribution of the standard deviation shown in Figure 39b is the lowest and has the least variability with τ demonstrating the reliability of the CF method in the high-shade area.

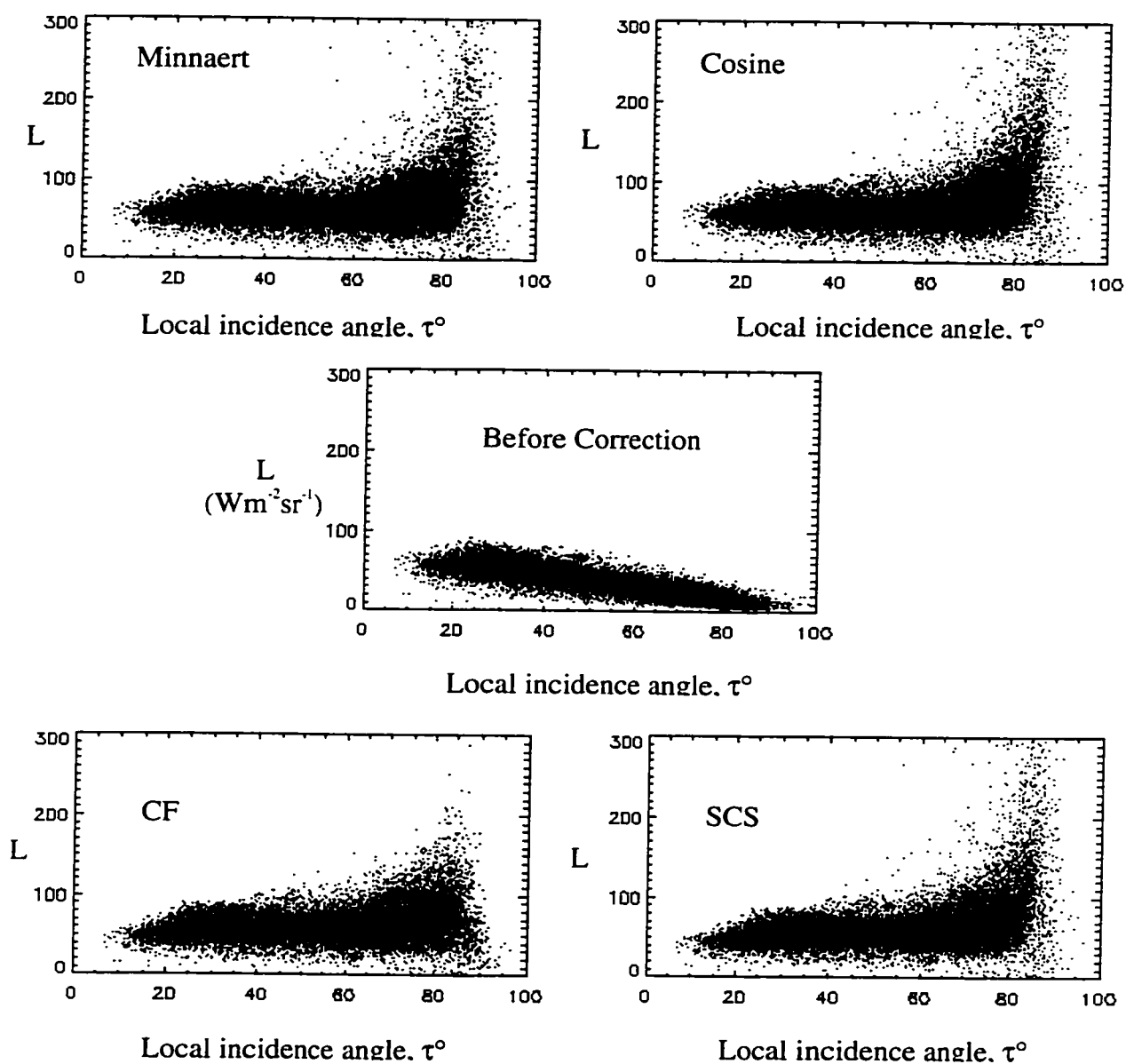


Figure 40. The scatter plots of the topographic correction before and after using four different methods on band 4 of Landsat Image 90.

The four models perform differently on the two images primarily due to the BRDF of the canopy surface. In the high-illumination range, where local incidence angle is low, the BRDF of the canopy surface is nearly constant, similar to the cosine function of a

Lambertian surface (Figure 35), as also noted by (Chihlar et al., 1994). Once the sun elevation angle is low, many areas are shadowed, and the relevant parts of the BRDF of the canopy surface have distinctive features, which only the CF models accounts for. Clearly, the serious over-estimation of the data corrected with the three other models is due to underestimating the reflectance. The “bump” of the CF in high-shade region (high local incidence angle) is a critical characteristic, and serves to reduce the over-correction.

Even so, there still remains some over-estimation in the CF-corrected data, which could be caused by several factors. First, the high noise/signal ration in high-shade areas will be exaggerated in correction. Second, the errors from mis-registration can extend into the correction results. Third, the uncertainty of the CF itself may affect the proper correction strength in this region. All these effects are interconnected, and are difficult to separate. If MS is properly considered, the over-correction can be further reduced, as discussed above.

CONCLUSIONS

The radiosity model has been used to compute the bi-directional reflectance distribution function (BRDF) of canopy surfaces, in order to build a proper topographic correction canopy function (CF) used for the topographic normalization of vegetated terrain. For the first time, MS effects of canopy structure at the subpixel scale have been considered in constructing the CF. Model forest canopies constructed from cones and ellipsoids were constructed and used for calculating the canopy function.

Three major features of the CF are distinguished by comparison with the cosine correction function. These correspond to three ranges of the cosine of the local incidence angle: a negative-angle region ($\tau < 0^\circ$), a middle region ($0^\circ \leq \tau \leq 60^\circ$), and a high-angle region ($60^\circ \leq \tau \leq 90^\circ$). In the negative-angle region, the CF shows increasing reflectance as slopes increase, whereas the cosine function predicts decreasing reflectance, indicating

the non Lambertian feature when sun elevation angle is very high. In the low-middle region, both the CF and cosine are similar linear functions, indicating the forest is nearly Lambertian for moderate sun elevation angles. In the high incidence-angle region (high shade areas) the CF, instead of smoothly decreasing as a function of $\cos(\tau)$, forms a small 'bump,' the magnitude of which is affected by many other parameters.

The shape and amplitude of the CF is controlled by several parameters: tree shape, tree spacing, tree surface reflectivity, and tree transmissivity. The basic shape of the CF, however, is directly related to the tree density, because shade and shadow are such a dominant factor controlling reflectance. Other parameters have smaller effects on the CF. The knowledge of all these effects enables us to understand intrinsic physical meaning of the bi-directional reflectance distribution function of a canopy surface.

The simple CF model has been applied to two Landsat TM images of vegetated terrain in the Pacific Northwest. One image was acquired in 1984, with a 60° sun elevation angle and a 123° zenith angle. The other image was acquired in 1990, with a 37.5° sun elevation angle and a 147° zenith angle. The results of the corrections show that the CF is an efficient topographic correction model for vegetated terrain.

In comparisons with the three other models, the CF model demonstrated the greatest advantage in the correction of forested terrain. The CF-corrected images have the smallest and constant standard deviations over the range of $\cos(\tau)$ and the least dependency on the hillslope angles, indicating that the CF model characterizes the reflectance distribution of vegetated surfaces better than the others. Correction at two different sun elevation angles shows the strong potential for correcting images at low sun elevation angles, where other models exhibit the most problems.

The topographic correction from the radiosity model has great flexibility for various surfaces. Using a forward-modeling approach, the radiosity model can compute the

suitable topographic corrections or functions (BRDF) for any simulated surface, such as soil, grass, or gravel bars. In dealing with complicated natural surfaces, many adjustments for this model will naturally be necessary; a major strength of the approach is that these adjustments are feasible.

SUMMARY

Separation of spectral and surface-structure information has been a major problem in using remotely sensed data. Mapping of land cover requires accurate recovery of spectral data for each type of material, but the remotely sensed data records only the radiant flux from the ground, and hence contains commingled information on both composition and roughness. In most remote-sensing studies, the surface has been assumed to be Lambertian and flat, having only direct reflectance. In fact, this assumption is not accurate, especially for rocky surfaces and vegetated surfaces in rugged terrain. The overall objective of this study is to develop an efficient numerical tool to separate the spectral and structural information, to help understand the physical properties of remotely sensed scenes, and to utilize the remotely sensed data more correctly and efficiently.

My dissertation is concentrated on two main subjects: modeling and application. The modeling part includes the radiosity model development, multiple-scattering prediction for two types of surfaces, and model verification. The application part includes the estimation of surface roughness (the extraction of surface structure information from images) and the correction of images of forests for topographic shading (the retrieval of reflectivity from images).

MODELING

As a primary tool, A practical hybrid radiosity model is adapted from existing algorithms in computer graphics and thermal engineering fields, and further developed for use in remote sensing. This new radiosity model accurately predicts radiosity from

natural surfaces, described by digital terrain models (DTMs), within acceptable precision and computation time limits. A complicated algorithm selects among three basic methods for calculating the radiosity, each having different speed and precision. These three are the double-contour integral, half-contour integral, and element-to-element algorithms. For each pixel in the image, the fastest algorithm is selected that will satisfy user-set limits of accuracy and precision. The radiosity calculation for an image of 100x100 pixels, with 2% error allowance, will take about 1.5 hour on an DEC Alpha-3000 station with a 278 MHz processor.

After the model was built, it was first used to specify the multiple-scattering component of the radiosity from various natural surfaces under a range of illumination geometries in order to investigate the importance of this term. Multiple scattering is determined by both reflectivity and surface structure, and thus is an important parameter for calculating these two parameters. For a flat surface, the multiple scattering is zero, increasing as the surface gets rough or as the reflectivity is increased. Multiple scattering occurs on most natural surfaces at all spatial scales and viewing and lighting geometries.

The radiosity model was applied to two typical land surfaces, at the pixel and subpixel scales. The results showed that the magnitude of MS in the scene varies with many parameters, including roughness of the surface, surface reflectivity, sky illumination, sun elevation angle and viewing direction. Under commonly encountered lighting conditions, the results demonstrated that multiple scattering is a more significant process than has previously been suggested. The amount of MS can vary with scale, because small-scale features such as boulders can maintain greater slopes than large-scale landscape elements. At the subpixel scale, the integration to the pixel scale of multiple-scattering effects can account for as much as 10% of the measured radiance. In addition to contributing a significant proportion of the radiosity, the surface roughness has a significant effect on the net BRDF; surfaces that are Lambertian when smooth become non-Lambertian when rough. At the pixel scale, in Landsat images of mountainous

regions for example, the fraction of a scene with significant (>5%) MS effects may exceed 10-20%. It is important to recognize and correct for these effects in quantitative image analysis

Verification of the radiosity model is necessary if it is to be used to predict the radiance from natural surfaces. Verification is presented in Chapter 3. The measuring experiments were conducted in the laboratory for two different types of surfaces. All the predictions from the model were compared with CCD radiance measurements made from various directions, by means of 1-D histograms, scatter plots and 2-D images, for a simple geometric surface (TA) and a real landscape surface (BC). The major mismatches between predicted and measured radiances were caused by the errors in the DTMs, geometric misregistration between the CCD image and the DTMs. Other errors are due to the illumination geometry for the physical surfaces and approximations made by the radiosity model.

The verification effort supports the conclusion that using SS to approximate the radiosity may cause 20% errors in general case, even up to 100% errors in shadow (if atmospheric down-welling irradiance is ignored). Therefore, it is at least sometimes necessary to account for MS in qualitative studies involving satellite images. It is also clear that MS is a major component in the reflectance from rough surfaces. Conventional image calibration, in which the surface is assumed to be flat and diffuse, is not accurate, especially for highly reflective surfaces such as snow, or vegetation in the NIR. Inaccurate reflectances calculated using the Lambertian assumption may introduce errors in remote-sensing applications.

The verification experiments have also demonstrated that the radiosity results are strongly sensitive to the accuracy of the DTM, especially in local environments, such as deep valleys, and cliffs. Overall, however, the hybrid radiosity model appeared to work properly and its predictions are accurate, reliable and applicable. From quantitatively

evaluating predictions and measurements, it appears that model accuracies are about 1-2%.

APPLICATIONS

I applied the radiosity model in two examples, first to retrieve the roughness information for a desert scene using an inversion method, and second to retrieve reflectivity for a forest in mountainous terrain by suppressing topographic information.

Estimating surface roughness using the radiosity model requires separating roughness and reflectivity influences on the measured reflectance. In Chapter 4, I have developed a new, semi-empirical inversion method based on foreground/background analysis (FBA) to estimate surface roughness from Landsat TM images. The central issue is to define a finite impulse response (FIR) filter with laboratory spectral measurements and the theoretical relationship of radiance response to surface roughness.

In this application, the radiosity model was used for correlating the radiosity with surface roughness and reflectivity. A series of rough surfaces, as was defined by the power-law spectral method, were simulated by inversion of specified Fourier transforms. The reflectivity spectra were measured for rock samples collected in the test areas. Thus, the sensitivity of the reflectance changes in the roughness and reflectivity of a surface may be computed and hence, the theoretical relationship of radiance to surface roughness may be established. The FIR filter was optimized using this theoretical relationship, in contrast to previously published methods, which use image data or field data to define the filter.

The semi-empirical inversion for roughness was applied to a Landsat TM image of Death Valley, chosen because Death Valley was a well-studied site used in previous investigations of surface roughness and radar data. Inversion results showed a good coincidence of estimation with field measurements, with regression coefficients of >0.7

for non-training areas. Spectral variability of the background was suppressed in calculated roughness image. For example, different geological units, having the same roughness but different lithologies and reflectivities (unit A, and the Kit Fox alluvial fans; Figure 28), were classified as a single unit in the roughness map, indicating success in retrieving the roughness information.

The semi-empirical inversion was compared with other methods for choosing the FIR: the field-data method, the image-data method, and the shade-image method. Comparison has shown that the semi-empirical inversion is more stable and accurate than the three other methods, for the non-training areas. There are two main factors which affect the accuracy of the semi-empirical inversion: sensitivity of reflectance to the phase information in the power-law spectrum; and the sensitivity of FIR filter to the variation of surface types in the scene. The former is related to the structure of the surface, and the later is related to the composition. The magnitudes of the effects from both factors are still in question, and require further study to estimate.

In topographic correction with the radiosity model, the model was used to construct a photometric function characterizing reflectance sensitivity to the view and illumination geometry of a rugged forested terrain. This abbreviated BRDF is here called the "canopy function" (CF). The CF actually is a special case of bi-directional reflectance distribution function (BRDF) of canopy surfaces, and varies only with the illumination direction (azimuth angle) and terrain slope angles. For the first time, MS effects in canopy structure, at the subpixel scale, have been considered in topographic correction. Three major features of the CF are distinguished by comparison with the cosine correction function. These features correspond to three ranges of the cosine of the local incidence angle: a negative-angle region ($\tau < 0^\circ$), a middle region (0° - 60°), and a high-angle region (60° - 90°). In the negative-angle region, the CF shows increasing reflectance as slopes increase, whereas the cosine function predicts decreasing reflectance. In the low-middle region, both the CF and cosine are similar linear functions, indicating the forest is nearly

Lambertian for these slopes and sun angles. In the high incidence-angle region (high shade areas) the CF, instead of smoothly decreasing as a function of $\cos(\tau_i)$, forms a small “bump,” the magnitude of which is affected by many other parameters.

Topographic correction based on the CF has been applied to two Landsat TM images of a forested test area in the Bluff Creek region of the Pacific Northwest. One image was acquired in the summer and has high sun elevation angle (60°), and the other was acquired in winter and has low sun elevation angle (37.5°). Correction results have shown that the CF model is an efficient, reliable topographic correction model for vegetated terrain. For the summer image, the CF-corrected reflectances are independent of terrain slope angles, as indicated by linear regression (slope = -0.003 for band 5). For the winter image, however, the CF-corrected data still show some residual terrain effects for shaded or shadowed slopes, probably because of the high noise/signal ratio in these areas. By taking account of the pixel-scale MS in the topographic correction, the over-corrections were reduced to some extent, even though the Lambertian assumption made in the CF correction is invalid for canopy surfaces.

Comparison has been made between the CF correction with other three methods: cosine correction, CSC correction and Minnaert correction. Of the four correction models, the CF method gave the best topographic-correction results, as indicated by the lowest slope of a linear regression of the corrected reflectances vs. terrain slope. Especially, the winter image, with a large area in shade or shadow, MS is an important factor and, therefore, the CF method has the greatest potential.

The CF method is flexible and can be readily adapted to different surface structures, and reflectivities. The CF can be constructed for any physical surface that can be described by the DTMs. For vegetated surfaces, it can be adjusted for the density of the canopy (tree spacing), the transmissivity of the trees, and different tree shapes. This

ability of the CF is a great advantage in topographic correction for different types of surfaces, and can be a useful tool for classifying the landcover.

The shape and amplitude of the CF is controlled by several parameters: the surface structure of the canopy (tree shape), tree spacing, tree surface reflectivity, and tree transmissivity. The basic shape of the CF, however, is directly related to the density of tree coverage, because shade and shadow are such a dominant factor controlling reflectance. Other parameters have smaller effects on the CF. The knowledge of all these effects enables us to understand the intrinsic physical meaning of the bi-directional reflectance distribution function of a canopy surface.

Through this study, I have developed a better tool for separating surface reflectivity and subpixel roughness or structure information from remotely sensed data. The radiosity model is a new technology in the remote-sensing field, but it has already demonstrated its importance in studying remotely sensed data quantitatively. From the two applications discussed above, it appears to have led to the development of more realistic physical models of radiative transfer than were possible before. However, the radiosity model discussed in this dissertation is still based on the Lambertian assumption, which is demonstrably incorrect for most natural surfaces. Therefore, a future model of greater complexity, one which can accommodate non-Lambertian scattering element is necessary. As a first step towards developing this model, it is necessary to know how sensitive the predictions from the current radiosity model are to the Lambertian assumption.

Most applications of the radiosity model in this dissertation have been limited to first-order problems, studied under many simplifying assumptions. Therefore, many questions remain. For example, the CF correction has been applied to heavily vegetated terrain. How well it works on rock or soil surface, or on forest containing different types of trees, remains to be determined. The potential for using the CF function to differentiate canopy types and cover estimates and seral stage likewise deserves study.

This dissertation has perhaps generated fewer answers than questions, but it has at least pointed out some possible fruitful avenues for future study, and some potential pitfalls in current ones.

BIBLIOGRAPHY

- Abuelgasim, A.A., and Strahler, A.H., 1994, Modeling of bidirectional radiance measurements collected by the Advanced Solid-state Array Spectroradiometer (ASAS) over Oregon transect conifer forests: *Remote Sensing of the Environment*, v. 47, p. 261-275.
- Adams, J.B., Smith, M.O., and Gillespie, A.R., 1989, Simple models for complex natural surfaces: a strategy for the hyperspectral era of remote sensing: *12th Canadian Symposium on Remote Sensing*, Volume 1, p. 16-21.
- Adams, J.B., Smith, M.O., and Johnson, P.E., 1986, Spectral mixture modeling: A new analysis of rock and soil types at the Viking Lander 1 Site: *Journal of Geophysical Research*, v. 91, p. 8098-8112.
- Anderson, J.R., 1977, Land use and land cover changes. A framework for monitoring: *Journal of Research by the Geological Survey*, v. 5, p. 143-153.
- Ashdown, I., 1994, Radiosity: a programmer's perspective. *John Wiley and Sons*, New York, 496 p.
- Aupperle, L., and Hanrahan, P., 1993, A hierarchical illumination algorithm for surfaces with glossy reflection: *Computer Graphics*, v. 27, p. 155-162, Anaheim, California.
- Austin, R.T., England, A.W., and Wakefield, G.H., 1994, Special problem in the estimation of power-law spectra as applied to topographical modeling: *IEEE Transactions on Geoscience and Remote Sensing*, v. 32, p. 928-939.

- Bauer, M.E., Daughtry, C.S.T., Biehl, L.L., Kanemasu, and Hall, F.G., 1986, Field spectroscopy of agricultural crops: *IEEE Transactions on Geoscience and Remote Sensing*, v. GE-24, p. 65-75.
- Baum, D.R., Rushmeier, H.E., and Winget, J.M., 1989, Improving radiosity solutions through the use of analytically determined form-factors: *Computer Graphics*, , Boston v. 23, p. 325-334.
- Bonan, G.B., 1993, Importance of leaf area index and forest type when estimating photosynthesis in boreal forests: *Remote Sensing of the Environment*, v. 43, p. 303-314.
- Borel, C.C., and Gerstl, S.A.W., 1992, Atmospheric corrections of land imagery using the extended radiosity method: IGARSS '92. *International Geoscience and Remote Sensing Symposium*: Houston, Texas.
- Borel, C.C., and Gerstl, S.A.W., 1994a, Radiosity based model for terrain effects on multi-angular views, IGARSS '94. *International Geoscience and Remote Sensing Symposium*, v. 3: Pasadena, CA, USA, p. 1667-1669.
- Borel, C.C., and Gerstl, S.A.W., 1994b, Nonlinear spectral mixing models for vegetative and soil surfaces: *Remote Sensing of the Environment*, v. 47, p. 403-416.
- Borel, C.C., Gerstl, S.A.W., and Powers, B.J., 1991, The radiosity method in optical remote sensing of structured 3-d surfaces: *Remote Sensing of the Environment*, v. 36, p. 13-44.
- Borengasser, M.X., Kleiner, E.F., Vreeland, P., Peterson, F.F., Klieforth, H., and Taranik, J.V., 1988, Geological and vegetational applications of Shuttle Imaging Radar-B, Mineral county, Nevada: *Photogrammetric Engineering and Remote Sensing*, v. 54, p. 71-76.

- Borengasser, M.X., and Taranik, J.V., 1988, Structural geology and regional tectonics of the Mineral County area, Nevada, using Shuttle Imaging Radar-B and digital aeromagnetic data: *International Journal of Remote Sensing*, v. 9, p. 967-980.
- Brown, S.R., and Scholz, C.H., 1985, Broad bandwidth study of the topography of natural rock surfaces: *Journal of Geophysical Research*, v. 90, p. 12,575-12,582.
- Chihlar, J., Manak, D., and Voision, N., 1994, AVHRR bi-directional reflectance effects and compositing: *Remote Sensing of the Environment*, v. 48, p. 77-88.
- Civco, D.L., 1989, Topographic normalization of Landsat Thematic Mapper digital imagery: *Photogrammetric Engineering and Remote Sensing*, v. 55, p. 1303-1309.
- Cohen, M.F., and Greenberg, D.P., 1985, The Hemi-Cube: A radiosity solution for complex environments: *Computer Graphics ACM SIGGRAPH 1985 Proceedings*, v. 19, p. 22-26.
- Cohen, M.F., and Wallace, J.R., 1993, Radiosity and realistic image synthesis: Cambridge, MA, Academic Press Professional, 381 p.
- Collins, J.B., and Woodcock, C.E., 1996, An assessment of several linear change detection techniques for mapping forest mortality using multitemporal Landsat TM data: *Remote Sensing of the Environment*, v. 56, p. 66-77.
- Deering, D.W., 1989, Field measurements of bidirectional reflectance, *Theory and Application of Optical Remote Sensing*: New York, Wiley, p. 14-65.
- Deering, D.W., Eck, T.F., and Grier, T., 1992, Shinnery oak bidirectional reflectance properties and canopy model inversion: *IEEE Transactions on Geoscience and Remote Sensing*, v. 30, p. 339-348.

- Dozier, J., and Frew, J., 1990, Rapid calculation of terrain parameters for radiation modeling from digital elevation data: *IEEE Transactions on Geoscience and Remote Sensing*, v. 28, p. 963-969.
- Dubois, P.C., van Zyl, J.J., and Engman, T., 1995, Measuring soil moisture with imaging radars: *IEEE Transactions on Geoscience and Remote Sensing*, v. 33, p. 915-926.
- Evans, D.L., Farr, T.G., and van Zyl, J.J., 1992, Estimates of surface roughness derived from synthetic aperture radar (SAR) data: *IEEE Transactions on Geoscience and Remote Sensing*, v. 30, p. 382-389.
- Evans, D.L., and Smith, M.O., 1991, Separation of vegetation and rock signatures in Thematic Mapper and polarimetric SAR images: *Remote Sensing of the Environment*, v. 37, p. 63-75.
- Evans, D.L., Farr, T.G., Van Zyl, J.J., and Zebker, H.A., 1988, Radar polarimetry: Analysis tools and applications: *IEEE Transactions on Geoscience and Remote Sensing*, v. 26, p. 774-786.
- Farr, T.G., 1992, Microtopographic Evolution of lava flows at Cima volcanic field, Mojave desert, California: *Journal of Geophysical Research*, v. 97, p. 15171-15179.
- Farr, T.G., Elachi, C., Hartl, P., and Chowdhury, K., 1986, Microwave penetration and attenuation in desert soil: A field experiment with the shuttle imaging radar: *IEEE Transactions on Geoscience and Remote Sensing*, v. 24, p. 590-593.
- Farrand, W.H., Singer, R.B., and Merenyi, E., 1994, Retrieval of apparent surface reflectance from AVIRIS data: a comparison of empirical line, radiative transfer, and spectral mixture methods: *Remote Sensing of Environment*, v. 47, p. 311-321.

- Franklin, J., Li, X.-W., and Strahler, A.H., 1986, Canopy reflectance modeling in Sahelian and Sudanian woodland and Savannah: *The Twentieth International Symposium on Remote Sensing of Environment*: Nairobi, Kenya, 10 p.
- Franklin, J., and Strahler, A.H., 1988, Inevitable canopy reflectance modeling of vegetation structure in semiarid woodland: *IEEE Transactions on Geoscience and Remote Sensing*, v. 26, p. 809-825.
- Franklin, J., and Turner, D.L., 1992, The application of a geometric optical canopy reflectance model to semiarid shrub vegetation: *IEEE Transactions on Geoscience and Remote Sensing*, v. 30, p.293-301.
- Gao, B.-C., and Goetz, A.F.H., 1994, Extraction of dry leaf spectral features from reflectance spectra of green vegetation: *Remote Sensing of the Environment*, v. 47, p. 369-374.
- Gerstl, S.A.W., and Borel, C.C., 1992, Principles of the radiosity method versus radiative transfer for canopy reflectance modeling: *IEEE Transactions on Geoscience and Remote Sensing*, v. 30, p. 271-275.
- Gillespie, A.R., 1992, Spectral Mixture Analysis of multispectral thermal infrared images: *Remote Sensing of the Environment*, v. 42, p. 137-145.
- Gillespie, A.R., Smith, M.O., Adams, J.B., Willis, S.C., Fisher, A.F., and Sabol, D.E., 1990, Interpretation of residual images: spectral mixture analysis of AVIRIS images, Owens Valley, California, *Airborne Scientific Workshop*: Pasadena, CA, JPL Publication., p. 243-270.
- Goff, J.A., 1995, quantitative analysis of sea ice drift , 1, methods for stochastic modeling: *Journal of Geophysical Research*, v. 100, p. 6993-7004.

- Gortler, S.J., Schroder, P., Cohen, M.F., and Hanrahan, P., 1993, Wavelet radiosity, *Computer Graphics*, v. 27, p. 221-230.
- Greenberg, D.P., 1989, Light reflection models for computer graphics: *Science*, v. 244, p. 166-173.
- Gu, D., and Gillespie, A., 1997, Topographic normalization of TM images of forest based on subpixel scale sun-canopy-sensor geometry: *Remote Sensing of the Environment*, in press.
- Hamilton, D.C., and Morgan, W.R., 1960, Radiant-interchange configuration factors: *National Advisory Committee for Aeronautics*, technical report.
- Hall-Konyves, K., 1987, The topographic effect on Landsat TM in gently undulating terrain in southern Sweden: *International Journal of Remote Sensing*, v. 8, p. 157-168.
- Hallum, C., 1993, A change detection strategy for monitoring vegetative and land-use cover types using remotely-sensed, satellite-based data: *Remote Sensing of the Environment*, v. 43, p. 171-177.
- He, X.-D., Heynen, P.O., Philips, R.L., Torrance, K.E., Salesin, D.H., and Greenberg, D.P., 1992, A fast and accurate light reflection model: *Computer Graphics*, v. 26: Chicago, p. 253-254.
- Hugli, H., and Frei, W., 1983, Understanding anisotropic reflectance in mountainous terrain: *Photogrammetric Engineering and Remote Sensing*, v. 49, p. 671-683.
- Ingram, K., Knapp, E., and Robinson, J.W., 1981, Change detection technique development for improved urbanized area delineation: Silver Springs, Maryland, USA, Computer Sciences Corporation, technical report.

- Itten, K.I., and Meyer, P., 1993, Geometric and radiometric correction of TM data of mountainous forested areas: *IEEE Transactions on Geoscience and Remote Sensing*, v. 31, p. 764-770.
- Jackson, R.D., Teillet, P.M., Slater, P.N., Fedosejevs, G., Jasinski, M.F., Aase, J.K., and Moran, M.S., 1990, Bidirectional measurements of surface reflectance for view angle corrections of oblique imagery: *Remote Sensing of the Environment*, v. 32, p. 189-202.
- Johnson, L.F., 1994, Multiple view zenith angle observations of reflectance from ponderosa pine stands: *International Journal of Remote Sensing*, v. 15, p. 3859-3865.
- Jon-Ranson, K., Irons, J.R., and Williams, D.L., 1994, Multispectral bidirectional reflectance of northern forest canopies with the Advanced Solid-state Array Spectroradiometer (ASAS): *Remote Sensing of the Environment*, v. 47, p. 276-289.
- Jones, A.R., Settle, J.J., and Wyatt, B.K., 1988, Use of digital terrain data in the interpretation of Spot-1 multispectral imagery: *International Journal of Remote Sensing*, v. 9, p. 669-682.
- Kaufman, Y.J., 1988, Atmospheric effect on spectral signature--measurements and corrections: *IEEE Transactions on Geoscience and Remote Sensing*, v. 26, p. 441-450.
- Kaufman, Y.J., and Holben, B.N., 1993, Calibration of the AVHRR Visible and Near-IR bands by atmospheric scattering, ocean glint and desert reflection: *International Journal of Remote Sensing*, v. 14, p. 21-52.
- Kawata, Y., Ueno, S., and Kusaka, T., 1988, Radiometric correction for atmospheric and topographic effects on Landsat MSS images: *International Journal of Remote Sensing*, v. 9, p. 729-748.

- Kleman, J., 1987, Directional reflectance factor distribution of two forest canopies: *Remote Sensing of the Environment*, v. 23, p. 83-86.
- Kriebel, K.T., 1978, Measured spectral bidirectional reflection properties of four vegetated surfaces: *Applied Optics*, v. 17, p. 253-259.
- Kusk, A., 1994, A multispectral canopy reflectance model: *Remote Sensing of Environment*, v. 50, p. 75-82.
- Lee, T.Y., and Kaufman, Y.J., 1986, Non-Lambertian effects on remote sensing of surface reflectance and vegetation index: *IEEE Transactions on Geoscience and Remote Sensing*, v. GE-24, p. 699-707.
- Leprieur, C.E., Durand, J.M., and Peyron, J.L., 1988, Influence of topography on forest reflectance using Landsat Thematic Mapper and digital terrain data: *Photogrammetric Engineering and Remote Sensing*, v. 54, p. 491-496.
- Li, W.-H., Weeks, R., and Gillespie, A.R., 1996, Multiple scattering in the remote sensing of natural surfaces, *The Eleventh Thematic Conference and Workshops on Applied Geologic Remote Sensing*, ERIM: Las, Vegas, Nevada, p. I-205-I-215.
- Li, X.-W., and Strahler, A.H., 1985, Geometric-optical modeling of a conifer forest canopy: *IEEE Transactions on Geoscience and Remote Sensing*, v. GE-23, p. 705-721.
- Li, X.-W., and Strahler, A.H., 1986, Geometric-optical bidirectional reflectance modeling of a conifer forest canopy: *IEEE Transactions on Geoscience and Remote Sensing*, v. GE-24, p. 906-918.
- Li, X.-W., and Strahler, A.H., 1992, Geometric-optical bidirectional reflectance modeling of the discrete crown vegetation canopy effect of crown shape and mutual

- shadowing: *IEEE Transactions on Geoscience and Remote Sensing*, v. 30, p. 276-292.
- Li, X.-W., Strahler, A.H., and Woodcock, C.E., 1995, A hybrid geometric optical-radiative transfer approach for modeling Albedo and directional reflectance of discontinuous canopies: *IEEE Transactions on Geoscience and Remote Sensing*, v. 33, p. 466-480.
- Liang, S., and Strahler, A.H., 1993, An analytic BRDF model of canopy radiative transfer and its inversion: *IEEE Transactions on Geoscience and Remote Sensing*, v. 31, p. 1081-1091.
- Moran, M.S., Jackson, R.D., Hart, G.F., Slater, P.N., Bartell, R.J., Biggar, S.F., Gellman, D.I., and Santer, R.P., 1990, Obtaining surface reflectance factors from atmospheric and view angle corrected SPOT-1 HRV data: *Remote Sensing of the Environment*, v. 32, p. 203-214.
- Malley, T.J., 1988, A shading method for computer generated images: *Master's thesis*, University of Utah.
- Meyer, S., Itten, K.I., Kellenberger, T., Sandmerier, S., and Sandmerier, R., 1993, Radiometric corrections of topographically induced effects on landsat tm data in an alpine environment: *ISPRS Journal of Photogrammetric Remote Sensing*, v. 48, p. 17-28.
- Muchoney, D.M., and Haack, B.N., 1994, Changes detection for monitoring forest defoliation: *Photogrammetric Engineering and Remote Sensing*, v. 60, p. 1243-1251.
- Mustard, J.F., and Pieters, C.M., 1987, Quantitative abundance estimates from bidirectional reflectance measurements: *Journal of Geophysical Research*, v. 92, p. E617-E626.

- Myneni, R.B., and Asrar, G., 1994, Atmospheric effects and spectral vegetation indices: *Remote Sensing of the Environment*, v. 47, p. 390-402.
- Nishita, T., and Nakamae, E., 1985, Continuous tone representation of three-dimensional objects taking account of shadows and interreflection: *Computer Graphics ACM SIGGRAPH 1985*, San Francisco, v. 125-132.
- Norman, J.M., 1984, Bidirectional reflectance modeling of non-homogeneous plant canopies, in Murphy, R.E., and Deering, D.W., eds., *Fundamental Remote Sensing Science Research Program Part I: Status Report Of The Scene Radiation And Atmospheric Effects Characterization Project*: NASA Goddard Space Flight Center, Greenbelt, MD, Tech. Memo, p. 55.
- Oh, Y., Sarabandi, K., and Ulaby, F.T., 1992, An empirical model and an inversion technique for radar scattering from bare soil surfaces: *IEEE Transactions on Geoscience and Remote Sensing*, v. 30, p. 370-381.
- Olsson, H., 1994, Changes in satellite-measured reflectances caused by thinning cuttings in boreal forest: *Remote Sensing of Environment*, v. 50, p. 221-230.
- Pak, K., Tsang, L., Chan, C.H., and Johnson, J.T., 1995, Backscattering enhancement of vector electromagnetic wave from two-dimensional random rough surfaces based on Monte Carlo simulations: *Journal Optical Society of America*, v. 12, p. 2491-2499.
- Proy, C., Tanre, D., and Deschamps, P.Y., 1989, Evaluation of topographic effects in remotely sensed data: *Remote Sensing of Environment*, v. 30, p. 21-32.
- Reyna, E., and Badhwar, G.D., 1985, inclusion of specular reflectance in vegetative canopy models: *IEEE Transactions on Geoscience and Remote Sensing*, v. GE-23, p. 731-736.

- Roberts, D.A., 1991, Separating spectral mixtures of vegetation and soils: Ph.D. Dissertation, Seattle, WA, University of Washington, 180 p.
- Roberts, D.A., Smith, M.O., and Adams, J.B., 1993, Green vegetation, nonphotosynthetic vegetation, and soils in AVIRIS data: *Remote Sensing of Environment*, v. 44, p. 255-269.
- Roberts, D.A., Smith, M.O., Adams, J.B., Sabol, D.E., Gillespie, A.R., and Willis, S.C., 1990, Isolating woody plant material and senescent vegetation from green vegetation in AVIRIS data: *Airborne Science Workshop*, Pasadena, Ca, p. 42-57.
- Sabol, D.E., Adams, J.B., and Smith, M.O., 1992, Quantitative subpixel spectral detection of targets in multispectral images: *Journal of Geophysical Research*, v. 97, p. 2659-2672.
- Sayles, R.S., and Thomas, T.R., 1978, Surface topography as a nonstationary random process: *Nature*, v. 271, p. 431-434.
- Schaaf, C.B., Li, X.-W., and Strahler, A.H., 1994, Topographic effects on bidirectional and hemispherical reflectances calculated with a geometric-optical canopy model: *IEEE Transactions on Geoscience and Remote Sensing*, v. 32, p. 1186-1193.
- Schaaf, C.B., and Strahler, A.H., 1993, Solar zenith angle effects on forest canopy hemispherical reflectances calculated with a geometric-optical bidirectional reflectance model: *IEEE Transactions on Geoscience and Remote Sensing*, v. 31, p. 921-927.
- Schaber, G.G., Berlin, G.L., and Brown, W.E., 1976, Variations in surface roughness within Death Valley, California, geologic evaluation of 25-cm-wavelength radar images: *Geological Society of American Bulletin*, v. 87, p. 29-41.

- Schröder, P., And Hanrahan, P., 1993, On form factor between two polygons. *Proc. Computer Graphics ACM SIGGRAPH 1993*, p.163-164
- Sellers, P.J., Meeson, B.W., Hall, F.G., Asrar, G., Murphy, R.E., Schiffer, R.A., Bretherton, F.P., Dickinson, R.E., Ellingson, R.G., Field, C.B., Huemmrich, K.F., Justice, C.O., Melack, J.M., Roulet, N.T., Schimel, D.S., and Try, P.D., 1995, Remote sensing of the land surface for studies of global changes, models-algorithms-experiments: *Remote Sensing of Environment*, v. 51, p. 3-26.
- Shinya, M., Takahashi, T., and Naito, S., 1987, Principles and applications of pencil tracing: *Computer Graphics*, v. 21, p. 45-54.
- Shirley, P., 1990, A ray tracing method for illumination calculation in diffuse-specular scenes: *Proceeding of Graphics Interface*, v. 90, p. 205-212.
- Shoshany, M., 1989, Secondary reflection effect on sensor response for a v-shaped valley: *International Journal of Remote Sensing*, v. 10, p. 1197-1206.
- Shoshany, M., 1993, Roughness-reflectance relationship of bare desert terrain: an empirical study: *Remote Sensing of the Environment*, v. 45, p. 15-27.
- Siegel, R., and Howell, J.R., 1992, Thermal radiation heat transfer: Washington, DC, Taylor and Francis Ltd., 1072 p.
- Sillion, F., and Puech, C., 1989, A general two-pass method integrating specular and diffuse reflection: *Computer Graphics*, v. 23, p. 335-344.
- Singh, A., 1989, Digital change detection techniques using remotely-sensed data: *International Journal of Remote Sensing*, v. 10, p. 989-1003.
- Smith, J.A., Cooper, K., and Randolph, M., 1984, Reflectance modeling, in Murphy, R.E., and Deering, D.W., eds., *Fundamental Remote Sensing Science Research*

- Program Part I: Status Report Of The Scene Radiation And Atmospheric Effects Characterization Project: NASA Goddard Space Flight Center, Greenbelt, MD, p. 50.
- Smith, J.A., Lin, T.L., and Ranson, K.J., 1980, The Lambertian assumption and landsat data: *Photogrammetric Engineering and Remote Sensing*, v. 46, p. 1183-1189.
- Smith, M.O., Rober, D.A., Hill, J., Mehl, W., Hosgood, B., Verdebout, J., Schmuck, G., Koechler, C., and Adams, J.B., 1994, A new approach to determining spectral abundances of mixtures in multiplespectral images, *Proceeding of IGARSS: JPL*, Pasadena, CA, 10 p.
- Smith, M., Weeks, R., and Gillespie, A., 1996, Using background factors to optimize roughness estimates from multipolarized SAR images, the Second International Airborne Remote Sensing Conference and Exhibition, San Francisco, California, p. 9.
- Smits, B.E., Arvo, J.R., and Salesin, D.H., 1992, An importance-driven radiosity algorithm: *Computer Graphics*, Chicago, v. 26, p. 273-282.
- Sparrow, E., 1963, A new and simple formulation for radiative angle factors: *Transactions of the ASME. The Journal of Heat Transfer*, v. 85, p. 81-88.
- Sparrow, E., and Cess, R., 1978, Radiative heat transfer: Washington, Hemisphere Publishing Corporation. 120 p.
- Suits, G.H., 1972, The calculation of the directional reflectance of a vegetative canopy: *Remote Sensing of Environment*, v. 2, p. 117-125.
- Syren, P., 1994, Reflectance anisotropy for nadir observations of coniferous forest canopy: *Remote Sensing of Environment*, v. 49, p. 72-80.
- Teillet, P.M., Guindon, B., and Goodenough, D.G., 1982, On the slope-aspect correction of multispectral scanner data: *Canadian Journal of Remote Sensing*, v. 8, p. 84-106.

- Townshend, J.R.G., Justice, C.O., Gurney, C., and McManus, J., 1992, The impact of misregistration on change detection: *IEEE Transactions on Geoscience and Remote Sensing*, v. 30, p. 1054-1059.
- Troutman, R., and Max, N.L., 1993, Radiosity algorithm using higher order finite element methods, *Computer Graphics*, Anaheim, CA, v. 27, p. 209-212.
- Van-Zyl, J.J., Burnette, C.F., and Farr, T.G., 1991, Inference of surface power spectra from inversion of multiplefrequency polarimetric radar data: *Geophysical Reserach Letter*, v. 18, p. 1787-1790.
- Vanderbilt, V. C., and Venecia, K. J. de, 1988, Specular, diffuse, and polarized imagery of an oat canopy: *IEEE Transactions on Geoscience and Remote Sensing*, v. 26 (4), p. 451-462.
- Wall, S.D., Farr, T.G., Muller, J.-P., Levis, P., and Leberl, F.W., 1991, Measurement of surface microtopography: *Photogrammetric Engineering and Remote Sensing*, v. 57, p. 1075-1078.
- Wallace, J., Cohen, M.F., and Greenberg, D.P., 1987, A two-pass solution to the rendering equation: a synthesis of radiosity and ray tracing methods: *Computer Graphics*, v. 21, p. 311-320.
- Wallace, J.R., Elmquist, K.A., and Haines, E.A., 1989, A ray tracing algorithm for progressive radiosity, *Computer Graphics ACM SIGGRAPH 1989 Proceedings 23*, Boston, v. 23, p.315-324.
- Watt, M., 1990, Light-water interaction using backward beam tracing: *Computer Graphics*, v. 24, p. 377-385.

- Weeks, R.J., Smith, M., Pak, K., Li, W.-H., Gillespie, A., and Gustafson, B., 1996, Surface roughness, radar backscatter, and visible and near-infrared reflectance in death valley, California: *Journal of Geophysical Research*, v. 101, p. 23,077-23,090.
- Zatz, H.R., 1993, Galerkin Radiosity: A higher order solution method for global illumination: *Computer Graphics*, v. 27, p. 213-220.
- Woodcock, C.E., Collins, J.B., Gopal, S., Jakabhazy, V.D., Li, X.-W., Macomber, S., Ryherd, S., Harward, V.J., Levitan, J., Wu, Y.-C., and Warbington, R., 1994, Mapping forest vegetation using Landsat TM imagery and a canopy reflectance model: *Remote Sensing of Environment*, v. 50, p. 240-254.
- Zebker, H.A., and Goldstein, R.M., 1986, Topographic mapping from interferometric synthetic aperture radar observations: *Journal of Geophysical Research*, v. 91, p. 4993-4999.
- Zebker, H.A., van Zyl, J.J., Durden, S.L., and Norikane, L., 1991, Calibrated imaging radar polarimetry: technique, example, and applications: *IEEE Transactions on Geoscience and Remote Sensing*, v. 29, p. 942-961.
- Zebker, H.A., van Zyl, J.J., and Held, D.N., 1987, Imaging radar Polarimetry from wave synthesis: *Journal of Geophysical Research*, v. 92, p. 683-701.

APPENDIX A: REFLECTANCES CALCULATED USING RADIOSITY MODEL
FROM THE COMPUTER-SIMULATED SURFACE FOR DIFFERENT ROCK
SAMPLES

	<i>Offset</i> ³	<i>TM</i> ¹ <i>1</i>	<i>TM</i> <i>2</i>	<i>TM</i> <i>3</i>	<i>TM</i> <i>4</i>	<i>TM</i> <i>5</i>	<i>TM</i> <i>7</i>
Sample 1	1.73	15.827	15.962	15.936	15.863	16.227	16.077
	2.13	18.532	18.689	18.659	18.574	18.995	18.822
	2.53	21.379	21.556	21.522	21.426	21.903	21.707
	2.93	24.388	24.585	24.547	24.44	24.97	24.752
	3.33	27.579	27.794	27.754	27.636	28.215	27.978
	3.73	30.974	31.206	31.162	31.036	31.657	31.402
Sample 2	1.73	15.491	15.536	15.516	15.473	15.358	15.276
	2.13	18.143	18.195	18.171	18.122	17.988	17.894
	2.53	20.938	20.997	20.97	20.913	20.762	20.654
	2.93	23.897	23.962	23.932	23.869	23.701	23.581
	3.33	27.042	27.114	27.081	27.012	26.828	26.696
	3.73	30.396	30.474	30.438	30.364	30.165	30.023
Sample 3	1.73	15.709	15.848	15.871	15.868	15.972	15.879
	2.13	18.396	18.556	18.583	18.58	18.7	18.592
	2.53	21.224	21.406	21.437	21.433	21.569	21.447
	2.93	24.216	24.418	24.452	24.448	24.599	24.463
	3.33	27.391	27.612	27.649	27.645	27.81	27.662
	3.73	30.772	31.01	31.05	31.045	31.222	31.063
Sample 4	1.73	15.707	15.947	16.099	16.11	16.532	16.1
	2.13	18.393	18.671	18.847	18.86	19.347	18.848
	2.53	21.222	21.537	21.735	21.75	22.3	21.737
	2.93	24.213	24.563	24.783	24.8	25.41	24.786
	3.33	27.388	27.771	28.011	28.029	28.694	28.014
	3.73	30.769	31.18	31.439	31.458	32.171	31.441
Sample 5	1.73	16.039	16.356	16.725	16.837	17.39	16.844
	2.13	18.778	19.143	19.568	19.698	20.333	19.706
	2.53	21.657	22.07	22.55	22.696	23.41	22.705
	2.93	24.697	25.156	25.687	25.848	26.636	25.858
	3.33	27.917	28.417	28.996	29.171	30.027	29.182
	3.73	31.337	31.874	32.494	32.682	33.597	32.694

¹ Offset of the line fitting to Fourier spectra of a surface

Sample 6	1.73	15.701	15.877	15.996	16.026	16.282	16.187
	2.13	18.387	18.59	18.728	18.763	19.059	18.948
	2.53	21.214	21.445	21.601	21.64	21.975	21.85
	2.93	24.204	24.461	24.635	24.678	25.049	24.911
	3.33	27.379	27.659	27.849	27.897	28.302	28.15
	3.73	30.759	31.06	31.264	31.315	31.75	31.588
Sample 7	1.73	15.599	15.686	15.731	15.698	15.634	15.422
	2.13	18.269	18.369	18.421	18.383	18.308	18.063
	2.53	21.08	21.193	21.253	21.21	21.125	20.847
	2.93	24.055	24.181	24.247	24.2	24.105	23.796
	3.33	27.216	27.354	27.426	27.374	27.27	26.932
	3.73	30.583	30.732	30.809	30.753	30.642	30.277
Sample 8	1.73	15.777	15.875	15.909	15.898	15.946	15.915
	2.13	18.474	18.588	18.627	18.614	18.67	18.634
	2.53	21.313	21.442	21.486	21.472	21.535	21.494
	2.93	24.315	24.458	24.507	24.491	24.562	24.515
	3.33	27.5	27.656	27.71	27.692	27.769	27.719
	3.73	30.888	31.057	31.114	31.095	31.179	31.124
Sample 9	1.73	15.48	15.838	16.119	16.25	16.514	16.174
	2.13	18.13	18.545	18.87	19.022	19.326	18.933
	2.53	20.923	21.394	21.761	21.933	22.276	21.833
	2.93	23.88	24.404	24.813	25.003	25.384	24.892
	3.33	27.024	27.597	28.043	28.251	28.666	28.13
	3.73	30.377	30.993	31.473	31.696	32.141	31.566
Sample 10	1.73	16.011	16.453	16.841	17.13	17.442	16.897
	2.13	18.745	19.255	19.703	20.034	20.393	19.767
	2.53	21.62	22.197	22.702	23.075	23.477	22.774
	2.93	24.656	25.296	25.854	26.266	26.71	25.934
	3.33	27.872	28.57	29.178	29.626	30.107	29.265
	3.73	31.289	32.038	32.69	33.168	33.682	32.782
Sample 11	1.73	15.632	15.653	15.656	15.582	15.486	15.386
	2.13	18.307	18.331	18.334	18.248	18.137	18.021
	2.53	21.124	21.15	21.155	21.057	20.931	20.799
	2.93	24.104	24.134	24.138	24.03	23.889	23.742
	3.33	27.269	27.301	27.307	27.188	27.033	26.873
	3.73	30.64	30.675	30.681	30.553	30.387	30.214
Sample 12	1.73	15.553	15.576	15.58	15.546	15.473	15.432
	2.13	18.215	18.242	18.246	18.207	18.123	18.074
	2.53	21.02	21.05	21.054	21.01	20.914	20.859
	2.93	23.988	24.022	24.026	23.977	23.871	23.81
	3.33	27.142	27.179	27.184	27.131	27.014	26.947
	3.73	30.504	30.543	30.549	30.491	30.365	30.293

VITA

Wen-Hao Li

University of Washington

1997

PERSONAL INFORMATION

Date of Birth: May 20, 1959

City of Birth: Tianjin, P. R. China

EDUCATION:

- 1992-present:** **Ph.D. candidate**, Department of Geological Sciences, University of Washington, Seattle, Washington. **Adviser:** Prof. Alan R. Gillespie.
- 1990-1992:** **M.S.**, Geology, Humboldt State University, Arcata, California. July 1992. **Adviser:** Prof. Gary Carver.
- 1982-1985:** **M.S.**, Remote sensing/GIS, Institute of Remote Sensing Applications, Peking University, P.R. CHINA, July 1985.
- 1978-1982:** **B.S.**, Geology, Peking University, P. R. CHINA, July 1982.

PAPERS AND REPORTS:

- Li, Wen-Hao**, Weeks, R., and Gillespie, A. R., 1996, Multiple scattering in the remote sensing of natural surfaces, *International Journal of Remote Sensing*, submitted.
- Li, Wen-Hao**, 1992, The late Holocene Subsidence Stratigraphy in the Eel River Syncline, northern California, in Carver, G.A., and Aalto, K.R., eds., Field guide to the late Cenozoic subduction tectonics and sedimentation of northern coastal California, GB-71: Pacific section, *American Association of Petroleum Geologists*, p.55-57.
- Li, Wen-Hao** and Xiang, H.F., Fang, Z.J., Li, R.Z. and Zhang, W.X., 1992, Preliminary study on the activity of the Miyun-Qianmen hidden fault zone, *North China Earthquake Sciences*, v.10, no.2, p.43-48.

- Li, Wen-Hao**, 1989, Seismotectonic surveys in 1966 Xing-Tai $m=7.2$ earthquake area, *Final-report to State Seismological Bureau (SSB)*, P.R. CHINA, pp 10.
- Weeks, R., Smith, M. O., Pak, K., Li, W.-H. 1996, Surface roughness, radar backscatter and visible and near-infrared reflectance in Death Valley, California, *Journal Geophys. Res.* vol. 101, no. E10, p.23077-23090.
- Qiang, Zuji and **Li, Wen-Hao**, 1988, The Statistical Correlation of Linear features and Earthquake Epicenters, *Northeastern Seismology*, Vol. 3, No. 3, pp 8.

ABSTRACTS:

- Gillespie, A. R., **Li, Wen-Hao**, Gu, D.-G., Adams, J. B., and Kahle, A. B., 1995, Measuring Change in forests with EOS/ASTER, *EOS Transactions, American Geophysical Union*, v.76, n.46.
- Li, Wen-Hao**, and G. A. Cover, 1992, Late Holocene Subsidence Stratigraphy of Eel River Syncline, Humboldt County, California, *GSA Abstracts with Programs, Cordilleran Section*, vol. 24, no. 5.